Chemical Tuning of Interaction Strength in 2-D and 3-D Frustrated Magnets

by

Jennifer Rose Morey

A dissertation submitted to Johns Hopkins University in conformity with the requirements for the degree of Doctor of Philosophy

Baltimore, Maryland

April, 2018

Abstract

Predictive design and synthesis of materials with quantum, topological, and magnetic properties is the frontier in quantum materials research. One of the most critical areas of research is the development of design principles for 2-D and 3-D magnetic materials, which exhibit a wide array of quantum behaviors. In this thesis I discuss materials design principles for, and synthesis and characterization of, new and newly-understood 2-D and 3-D frustrated magnets.

It was the employment of materials design principles that led to the discovery of two new compounds, $MgNiMo_3O_8$ and $FeNiMo_3O_8$, which were synthesized by site-specific chemical substitution on $Ni_2Mo_3O_8$, an integer-spin nickel honeycomb with tetrahedrally and octahedrally coordinated nickel on the two halves of the bipartite honeycomb lattice. These 2-D magnetic materials are discussed in Chapter 2. $Ni_2Mo_3O_8$ is the first known realization of zig-zag antiferromagnetic order in a non-centrosymmetric integer-spin honeycomb lattice.

The diamond lattice in spinel structure compounds is a 3-D frustrated lattice. $FeSc_2S_4$ is a well-known material that has been predicted to host a disordered quantum spin liquid state down to the lowest measurable temperatures. In both powder and crystal samples, antiferromagnetic order was observed to develop below T = 10 K, placing $FeSc_2S_4$ close to, but on the

antiferromagnetically ordered side of a quantum critical point, which is within the paradigm of theoretical predictions on this material.

Finally, two nascent projects are discussed in Chapter 4. One is the discovery and characterization of the first metallic kagomé antiferromagnet, KV_3Sb_5, and characterization of its physical properties. An antiferromagnetic transition at $T = 80$ K can be increased to $T = 100$ K by doping the material with Ba. In contrast, doping with Sn seems to reduce the magnetism in the material. The physical properties of M_3(hexaiminobenzene (HIB))$_2$, M = (Ni, Cu), have been reported as metals. However, resistivity and heat capacity measurements show that they are more likely small band gap semiconductors.

Dissertation committee

Advisor - *Professor Tyrel M. McQueen*

Professor Collin L. Broholm

Professor Thomas J. Kempa

Acknowledgements

"We have made a deal with a particularly inefficient devil that trades three years of our lives for one entry on IMDb, and these things are biography and they are alive"

- Guillermo Del Toro

Like so many human endeavors, this dissertation is the product of years of personal and communal work. First, I would like to thank my advisor, Dr. Tyrel M. McQueen for his guidance and support. Our scientific discussions and frank conversations have revealed worlds of new information to me and have elevated my intellectual capacity. His enduring optimism and pure scientific joy have been a model to me; a refreshing break from the bitterness that pervades academia. I have been struck more than once by the *rightness* of joining his laboratory and truly believe I could not have made a better choice. I do not know how to repay my debt of gratitude. Many things in my life and future would not have been possible without him and the people in his support network have made to support his career, so mine by extension (Thanks Courtney!). It truly takes a village.

I would like to thank the esteemed members of my committee, Dr. Collin L. Broholm and Dr. Thomas J. Kempa for their support. I have had the opportunity to work alongside many of the graduate students and post-docs in Dr. Broholm's research group, and have benefitted greatly from his and their help. Dr. Thomas J. Kempa has been a wonderful mentor to me since his arrival at Johns Hopkins University. It is impossible for me to overstate my gratitude to him for his time, advice, and guidance. Jestem niezmiernie wdzięczna Tomkowi za wyciągnięcie do mnie przyjaznej dłoni. Zawdzięczam mu część mojego sukcesu. Obiecuję, że pomoc, którą mi ofiarował, przekażę kolejnemu pokoleniu naukowców. Niech żyje nauka, chemia i Polska!

My parents encouraged my academic interests from the beginning, and I couldn't be more grateful. From them I learned the stubbornness, self-reliance, pride, and work ethic that I needed to get me where I am today. I have said to many people that no matter how hard I work, I could not possibly be working harder than my Mom, and I stand by that statement. Her unqualified and unconditional love and support means the world to me (love you more!). The unexpected loss of my father in September 2015 shook my spirit, and I miss him dearly. Perhaps nobody would have been prouder of, and more likely to tell every person they know and meet about, my successes than my Dad. My grandparents have been wonderfully supportive through my life as well. The weekends and

days and summers I spent with Grammy define me still. Growing up with the knowledge that you are truly loved is a fundamentally formative experience. I also thank Grandma and Grandpa for keeping me grounded, as I am more likely to be found daydreaming than working. I am thankful to my aunts Karen and Pat for loving me despite the fact that I, as a child, bent the rules of board games and broke every glass in their house. All my love.

My friends, roommates, and colleagues have played a big role in my success. I am grateful to the welcoming and rigorous academic environment that the early McQueen Lab members cultivated when I joined – John P. Sheckelton, Kathryn E. Arpino, David C. Wallace, Patrick Cottingham, Allyson M. Fry-Petit, Benjamin A. Ttrump – and the friendship and feedback I receive from my current contemporaries T. Thao Tran, Juan Chamorro, Tanya Berry, Mekhola Sinha, Veronica J. Stewart, Cheng Wan, Michał J. Winiarski, Hector Vivanco, Jessica R. Panella. I would like to thank Zachary A. Kelly specifically for his patience and support as an office mate for the last few years. More than anybody else, Zach has been a sounding board for ideas – a role that requires all of his essentially infinite patience and communication skills. I wish him all the best in the world. My roommates and MIF friends have been wonderfully diverting and essential to my progress - Chris J. Kauffman, Celia P. Litovsky, Samantha C. (Coffey) Paschke, Jordan Paschke. I would also like to thank Caroline Lo Ré Brewer for her love and

friendship. I wouldn't have gotten my M.S. without her, and every time we talk I appreciate her more. I look forward to the time I will be able to spend with her this summer. Many other excellent friends have gone unnamed here, but know that I think of you often and fondly. Thank you!

Two people I would like to mention as lights in my life, who are personally responsible for the maintenance of my physical and mental health, are Ian Moltrup and Julia Gallogly. Ian and I have a wonderful friendship, and between the fighting and bickering, he has fed me and helped me get to and from work for years. I couldn't be more grateful. Besides myself and my advisor, he has the most invested in the production of this dissertation. Julia has been my best friend since we met at orientation before our freshman year of college. Our conversations, in turns ponderous and exploratory, have allowed me the luxury of trying on ideas in a judgement-free environment. I look forward to many more years of fruitful discussion and good-doing together. Love!

Finally, I would like to thank and dedicate this work to the many teachers who have taken my hand for some part of my journey. More than most, school represented for me a haven; an academic oasis of safety and freedom. These unsung heroes did a lot for me, and without them I might not have 'made it': Andrew Wiza, Nina Arnold, Christine Rice, Jason Bielik, Mrs. Dube, Arthur

O'Connor, Bess Blunt, Jay Resmini, Nan Foley, and so many more. I would also like to thank Mike Lent, from whom I learned how to live my best life. Thank you.

While I do not know where my path will take me, I am secure in knowing that all of the people mentioned above have given me the tools I need to face it on my own terms, and to look inwards to find my own truth.

Table of Contents

List of Figures

List of Tables

Chapter 1 Introduction

Section 1.1 An Optimistic Vision for the Future

Human demand for energy and progress is poised to outstrip our capacity for energy production. The vast majority of the energy economy is carbon and hydrocarbon based. There are a few reasons for this: liquid hydrocarbons have a particularly high energy density. They can be transported easily in tanks and pipelines and can sit easily in cars and generally produce a massive amount of energy relative to the volume that they occupy. But it is also well known that these resources are finite: the easily accessible hydrocarbons are gone and require increasingly more energy to mine and refine. Where is the economic tipping point of 'worth it' on energy consumption?

Not only are resources dwindling, but the use of resources causes its own problems. It is written into one of the most fundamental chemical reactions: combustion. The burning of C_xH_y in an O_2 atmosphere releases CO_2, CH_4, and other greenhouse gases that contribute to unprecedented rapid climate change. Every action that a person takes that uses energy, even the act of being born, starts the meter on a personal carbon debt.

So, where is the optimistic vision for the future? Human progress – the search for new renewable energy sources- is in a race against time against human progress – the use of carbon-based energy to do so. **The optimistic vision for the future is that human progress might win**.

The history of human progress is inextricably linked with progress in materials research. It could be reasonably argued that science is the oldest profession. Even before language existed, early proto-homo-sapiens-sapiens must have thought "????" in response to seeing lightning. Perhaps a person, who, after falling and landing on a particularly sharp piece of diagenetically altered siliceous ooze (aka flint or chert) used it instead of sharpened wood on the end of their spear, might now be considered a scientist (Or an engineer? Differentiation between these terms is beyond the scope of this work). And the subset of 'chemists', long the purveyors of death via poison or explosion, have happily found more expansive uses for their multitudinous skills in recent years.

Notably, some famous chemists have walked the line: Fritz Haber won the Nobel Prize in 1918 for his development of the Haber-Bosch process, a chemical process that produces ammonia from nitrogen gas and hydrogen gas. It has been used to mass-produce fertilizer and has quadrupled the productivity of agricultural land, thereby enabling the massive population boom and saving

billions of famine-endangered lives. Up to 50% of nitrogen found in human tissues is from the Haber-Bosch process. Before achieving notoriety for this, he was known as 'the Father of Chemical Warfare' (which is a slight to the many thousands of years of fabulous Asian alchemists, but that, too, is beyond the scope of this work) for his eager development of bromine and chlorine gases as chemical weapons in World War I. In fact, somebody watching the 2017 action film

Most technology before the industrial revolution was geographically and temporally localized. For example, the best method for producing Damascus steel, was kept so secret that it was lost for thousands of years upon the death of the manufacturer. It is hard to imagine how that progress could go backward. Our technology is constantly and rapidly improving and evolving. But not so long ago, before the industrial revolution, the idea that progress could go backwards was culturally consistent. The Gauls, who came across the crumbling aqueducts after the fall of Rome, may have asked themselves "What Gods could have created these?" But even then – the math used to design the aqueducts was re-invented after having been discovered and lost thousands of years earlier in ancient Persia.

Methods for purifying silicon for use in transistors defines modern technology in the same way that Damascus steel defined its era. In the span of a human lifetime we have redefined human communication. I can correspond via e-mail with my grandmother, who didn't have electricity in the house she lived in as a child. We live in the 'silicon age' and now we must discover what next 'age' is. Some would say it is quantum computing.

It is exciting to be a materials chemist at the forefront of innovation and discovery. Just as the inventor of the telephone didn't know that the majority of Americans would carry a personal one, and just like the discoverer of the superconductor didn't know that it would ultimately be used in some of the most powerful medical diagnostics that we can do, we don't necessarily know the applications of new quantum materials *a priori*. But in some cases we start with an application – a problem that needs a solution – and in the process make great discoveries. This is the thrill of materials design – simultaneous engagement with applications and discoveries.

To usher in the next age of progress, hopefully towards energy efficiency and renewable energy production and storage, we need to develop currently unknown sources of computing and predictive computing power. That is one of the many strengths of quantum materials – these materials can possibly be used

for information processing and storage and can, in conjunction with human–developed intuition, accelerate the rate of research and save the human race from a self-imposed population apocalypse.

Section 1.2 The Materials Lifecycle

1.2.1 The Joy of Predictive Design

When we talk about 'predictive design' we are referring to two things: (1) predictive design of synthetic methods where we choose a method to get a product, and (2) choosing a structural motif that gives a material desired properties. Deciding what to make and how to make it is easy; proving that you succeeded is the subject of essentially all theses on chemistry.

The materials lifecycle is the fundamental principle that we use when looking for new materials. The development of a new material begins with a need, and it falls to the materials chemist to invent the material to address the need. After a survey of known materials, we decide on a structure, a stoichiometric ratio, and constituent elements to target a new material. Then we assess the results of the synthesis. Did we get what we wanted? Great - we measure the properties to see if we were right and predicted them correctly. If

we did not get what we wanted – why? What was wrong in the design principles? Did we get a different material instead? Why? What are the properties of that material? Are they useful? Sometimes when looking at the properties of those new materials we discover new phenomena. Sometimes the materials we make are useful for devices and advanced technology.

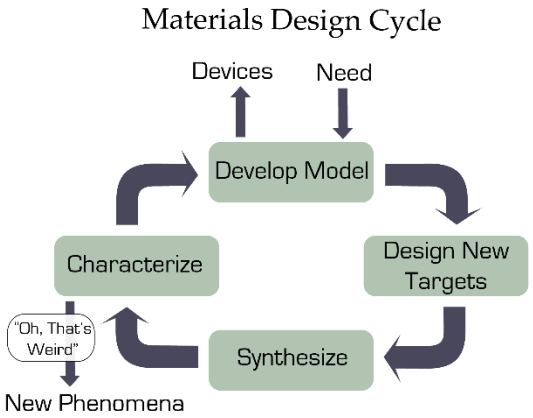

Figure 1.1 Materials design conceptual feedback loop for the discovery of new materials

1.2.2 Predictive design of synthetic methods

Our friends in organic chemistry experience the joy of experimental predictive design all the time. The catalog of methods available to the organic chemist gives them enough control to adjust the bonding environment of *one* atom in the middle of a massive molecule; to select a particular chirality of a molecule; to control the hydrophobicity of a polymer by changing one bond. The reason for this is that molecular chemists run reactions in the kinetic regime; the rate

limiting step is much faster than that of traditional ceramic methods which rely on diffusion of ions through solids. When the desired product is thermodynamically stable at the synthesis conditions, traditional methods are sufficient. However, this is certainly not the case for all materials. While the lexicon of methods for materials synthesis is by no means complete, there has been some excellent work on topotactic/soft chemistry/ *chimie douce* reactions. Recently and notably, the McQueen lab succeeded in using soft chemistry methods to electron dope the candidate spin liquid material Herbertsmithite [1].

1.2.3 Predictive design of structural motifs

Deciding on a structural motif is essentially answering the questions 'what elements, in what coordination, on what lattice'.

What elements?

One of a chemist's handiest tools for design of a new molecule or compound is elemental substitution. Elements in the same period often have similar reactivity, and that elements adjacent to each other on the periodic table are often similarly sized with one more/less electron than their neighbor. Many of the common periodic trends, Figure 1.1, are useful when designing chemical substitution experiments.

One of the most relevant periodic trends for solid state chemists is the increase in spin-orbit coupling (SOC) with higher mass. Other periodic trends such as metallic character, ionization energy, and electron affinity are highly relevant as well. Ionic radius is particularly important for chemical substitution. If the target compound is isostructural to a parent compound, then often the substituting element approximately the same size as the element that it is replacing. One point of interest is that atomic radii are different in molecules and vacuum than they are in crystals. This is visualized in Figure 1.2.

The nature of the bonding in materials is directly related to properties. In solid materials, electrons can have varying degrees of localization. In metals, electrons are shared and delocalized between atoms. In covalent solids, the electrons are localized on the atoms. In rare earth compounds, electrons can be both – some are localized around the atoms, and some are shared in the lattice. In general, materials comprised of elements with very different electron affinity may tend to have more localized electrons and ionic bonds.

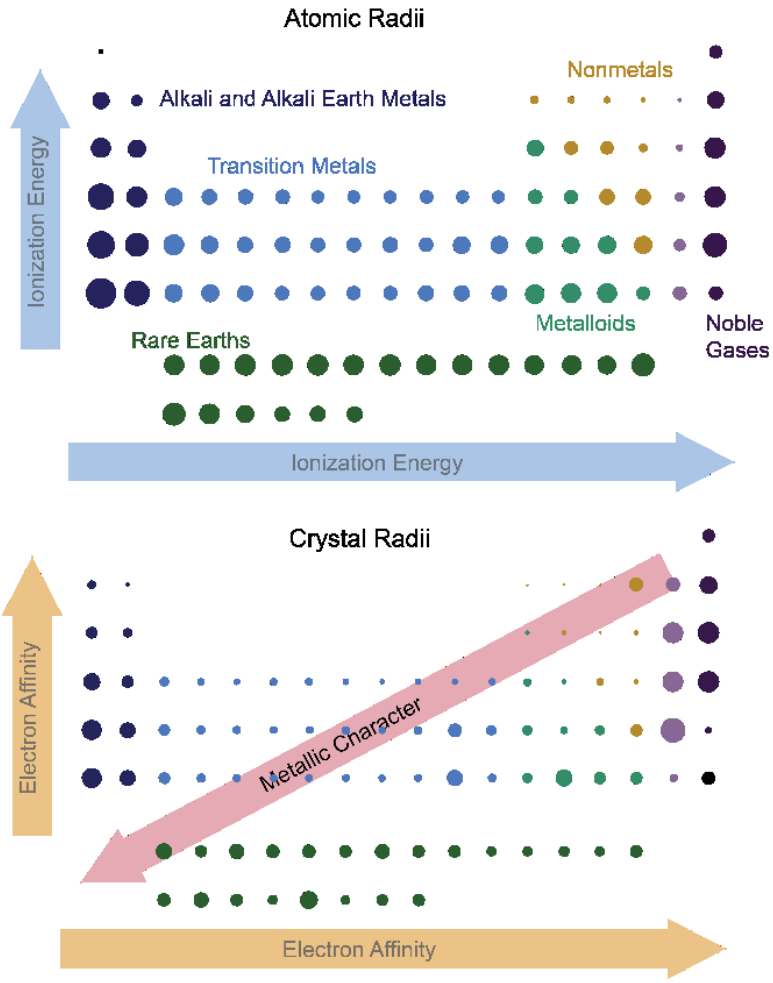

Figure 1.2 Periodic Trends and atomic and crystal radii of the elements. The crystal radii of cations and halogens are particularly different than the atomic radii.

What coordination?

The electrostatic interactions between ligands and metals centers cause orbital splitting. Figure 1.3 shows how the d orbitals split when coordinated ligands induce an anisotropic ligand field. These predictable orbital splittings can be leveraged, when combined with known elements and oxidation states, to control

the number of unpaired electrons in a system, and thus impacts the magnetic properties of a material. Some examples of electron filling in trigonal bipyramidal-split orbitals are shown in Figure 1.4. The green lines on the diagram connect similar states. For example, both d^2 and d^6 have two unpaired electrons in E orbitals, both d^3 (low spin) and d^7 (low spin) have one unpaired electron in an E orbital; the high spin configurations have three unpaired electrons. The configuration in d^3 places all three in E orbitals, and d^7 places one in a singly degenerate orbital.

Degeneracy arises when there are two or more states in a system that are at the same energy. In Figure 1.4, the high spin and low spin d^3 configurations have both spin and orbital degeneracy, while only the d^7 low spin configuration has orbital degeneracy. Often a system is able to lower its overall energy by releasing degeneracy, which can happen via a myriad of mechanisms including orbital ordering, ligand distortions, et al. A manifold with electrons sitting in orbitals can have spin and/or orbital degeneracy, arising when two spin configurations have the same energy, or when there are multiple configurations of spin occupation in orbitals that have the same energy. While the vast majority of materials do lift their degeneracy, some may be able to host states that maintain finite degeneracy to T = 0 K. The materials that are able to do this tend to have atoms sitting on a frustrated lattice. [2-5]

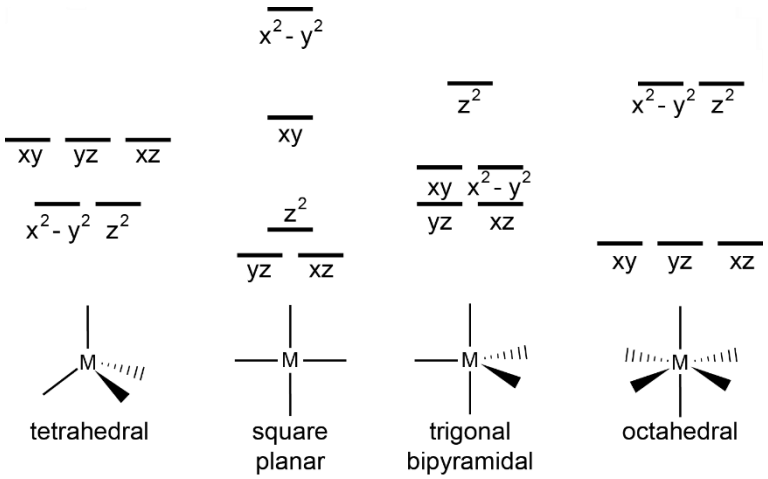

Figure 1.3 The presence of a ligand field breaks the degeneracy of the *d* orbitals and results in various patterns of orbital splitting, shown here on an approximate energy scale for tetrahedral, square planar, trigonal bipyramidal, and octahedral coordinations.

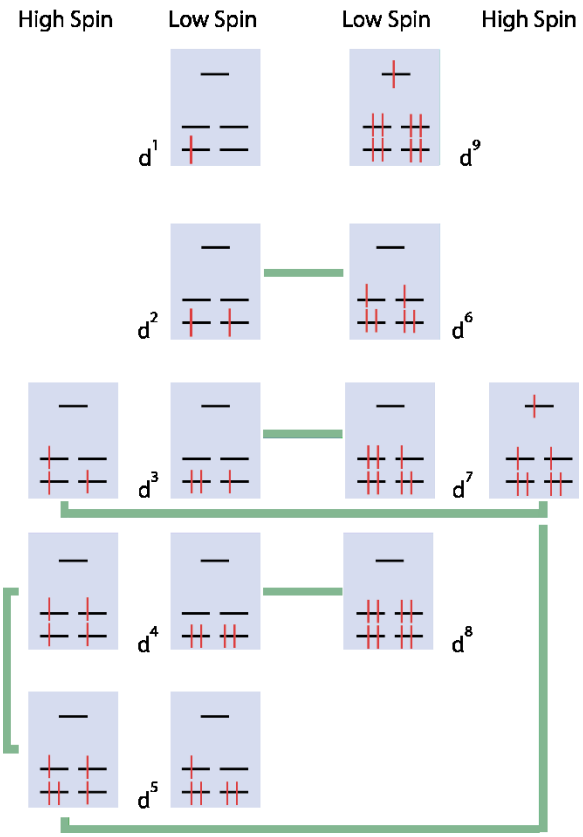

Figure 1.4 Population of the trigonal bipyramidal orbital splitting with occupancies d^0-d^9.Lines are drawn between similar electron configurations.

What lattice?

There are a vast number of structure types of materials. While there are some restrictions that arise from tiling in three-dimensional space, there are many, many structures that materials can adopt. It is also true that the vast majority of them do not host quantum behavior. Geometrically frustrated lattices are, however, known to do so. The fundamental structural motif of frustration is the triangle, for the reason that antiferromagnetic interactions cannot be trivially resolved on the three vertices. The triangular motif can be seen on one of the

canonical frustrated lattices : the two dimensional kagomé lattice, visualized in Figure 1.5 [1]. In the right panel of Figure 1.5 the relationship between the kagomé and honeycomb materials can be seen – they are complementary structures.

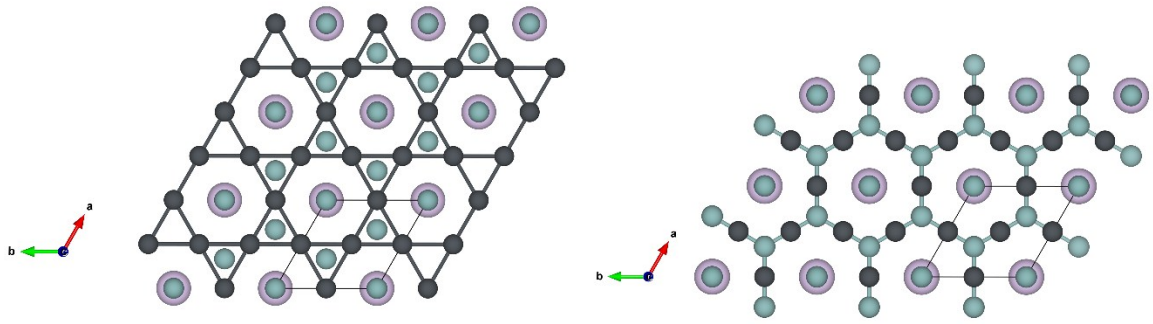

Figure 1.5 The relationship between the kagomé lattice and the honeycomb lattice is shown by: (left) a kagomé lattice of black atoms, and (right) the same structure where bonds between the green atoms make a honeycomb.

Another three-dimensional frustrated lattice is the spinel structure, with a general chemical formula AB_2X_4, where the 'A' site is on a frustrated diamond lattice. This is visualized in Figure 1.6 where the dark green and purple atoms occupy the diamond lattice. The polyhedra centered around the 'B' sites are shown in pink. The fundamental unit of frustration is again the triangle; here, they comprise the tetrahedral geometry connecting the magnetic atoms to each other. The magnetic exchange paths are shown explicitly in Figure 1.6 (b), here for

$NiRh_2O_4$. As exchange interactions follow paths through ligands, the chemical identity and bonding interactions along these pathways are relevant as well.

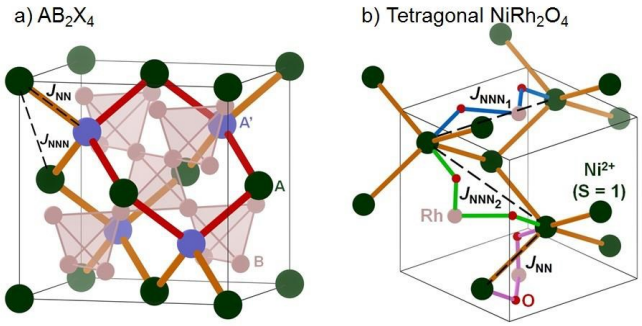

Figure 1.6 Spinel structure and 3D magnetic exchange pathways from Chamorro et al., (2018). [6]

As the kagomé lattice is structurally related to the honeycomb lattice, Figure 1.8, the spinel lattice is related to another lattice of importance to the quantum materials community: the pyrochlore lattice. The A sites of a spinel, shown in the right panel of Figure 1.7, are on a diamond lattice, and the 'B' sites make up the pyrochlore lattice, shown in the left panel of Figure 1.7.

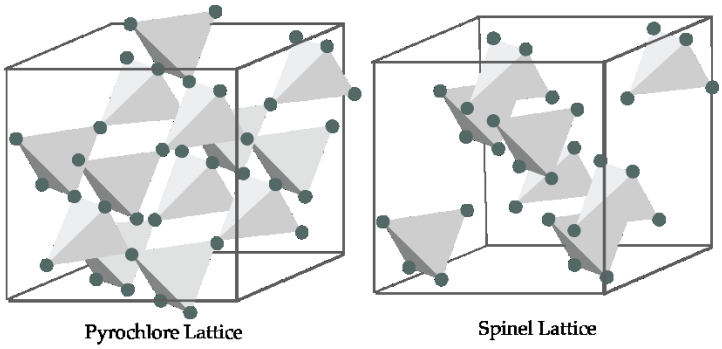

Figure 1.7 Related 3D lattices: spinel and pyrochlore

The honeycomb lattice is not inherently geometrically frustrated. It is a bipartite lattice comprised of two triangular lattices, visualized in Figure 1.8 where one triangular sublattice is green atoms and the other is blue atoms. This lattice could support trivial "Néel" antiferromagnetic order where all green atoms have magnetic moments pointing "up" and the blue atoms have magnetic moments pointing "down" (or vice versa). Materials with this structure become frustrated in the presence of competing magnetic exchanges [7].

The layering inherent to 2D materials often results in many stacking variants in these materials. One such stacking variant is shown in the right-hand panel of Figure 1.8, where blue atoms are directly over green atoms, but one could imagine many others.

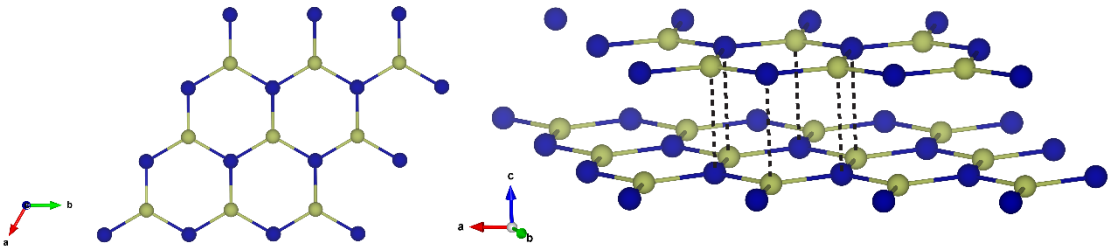

Figure 1.8 Honeycomb lattice with one stacking variant. The two halves of the bipartite honeycomb are green and blue.

Section 1.3 Group Theory

The symmetries of solids and materials can be usefully classified using Representation Theory, which is a subject in the mathematical discipline of Group Theory. Many excellent texts have been developed that describe how the symmetries of molecules are determined, and how these symmetries can be used to determine, for example, symmetry 'allowed' and 'forbidden' transitions in spectroscopy. Here I will describe the use of group theory to decompose/identify the symmetries of the states in a solid.

Chemists tend to describe the symmetry of molecules using the Schoenflies notation, whereas physicists and materials scientists/engineers use Hermann-Maugin notation (equivalently: International notation). The 32 space groups and their Schoenflies and Hermann-Maugin notations are listed below in Table 1.1.

Table 1.1 The 32 space groups with Hermann-Maugin (International) notation and Schoenflies notation.

Crystal system	Hermann-Mauguin notation	Schoenflies notation	Crystal system	Hermann-Mauguin notation	Schoenflies notation
Triclinic	1	C_1	Trigonal	3	C_3
	-1	C_i		-3	C_{3i}
Monoclinic	2	C_2		32	D_3
	m	C_s		3m	C_{3v}
	2/m	C_{2h}		-3m	D_{3d}
Orthorhombic	222	D_2	Hexagonal	6	C_6
	mm2	C_{2v}		-6	C_{3h}
	mmm	D_{2h}		6/m	C_{6h}
Tetragonal	4	C_4		622	D_6
	-4	S_4		6mm	C_{6v}
	4/m	C_{4h}		-62m	D_{3h}
	422	D_4		6/mmm	D_{6h}
	4mm	C_{4v}	Cubic	23	T
	-42m	D_{2d}		m-3	T_h
	4/mmm	D_{4h}		432	O
				4-3m	T_d
				m-3m	O_h

In each space group, there are special atomic Wycoff positions, denoted with letters *a, b, c,* etc. which each have a point group symmetry, a position operator (how the x, y, and z coordinates behave relative to each other, and a multiplicity (the number of these sites that exist in the unit cell under the space group symmetry). The Wycoff positions in space group $P6_3mc$ are listed in **Table 1.2**, with their multiplicities, point group symmetries, and position operators. From this, we can understand that atoms on Wycoff positions have C_{3v} symmetry (3m, Hermann-Maugin), those on the *c* position have Cs symmetry, and those on

position *d* have C_1 symmetry. Sometimes the Wycoff positions are notated with their Wycoff positions, so in $P6_3mc$, the Wycoff sites are: 2*a*, 2*b*, 6*c*, and 12*d* [8].

Table 1.2 Wycoff positions of space group 186, $P6_3mc$

Wycoff position	Multiplicity	Point Group	Position Operator
d	12	1	*x*, *y*, *z*
c	6	m	*x*, -*x*, *z*
b	2	3m	1/3, -1/3, *z*
a	2	3m	0, 0, *z*

When we categorize the symmetry of a molecule, we consider the symmetry operations in three-dimensional space. Another way to say this is that atomic positions vary under the inversion of space, but not under the inversion of time. In this space, a 360° rotation (the identity operation E) brings an atom back to its original position. In contrast, electrons and other spin-having objects are invariant under space-inversion, but do vary under time inversion. This means that the symmetry of electrons follows the symmetry of double groups. And, while there are 230 positional space groups, there are 1651 magnetic space groups.

For comparison, the single group and double group character tables for T_d (tetrahedral) symmetry are listed in Table 1.3 and Table 1.4, respectively. In the character tables, the columns are the symmetry operations (E, C_3, etc.). The T_d

double group is twice the size of the T_d single group: there are 24 symmetry operations in the single group (1 E, $8C_3$, $3C_2$, $6S_4$, $6\sigma_d$) and 48 in the double group. The rows of the character tables are irreducible representations (IRs). The dimensionality of an IR is easily seen in the number under the identity operator, E: A_1, A_2 are 1-dimensional; Γ_1 and Γ_2 are 'singlets'; the E representation is 2-dimensional and Γ_3 is a doublet; T_1 and T_2 are 3-dimensional and Γ_4 and Γ_5 are triplets.

Table 1.3 Character table for tetrahedral (T_d) symmetry in the single group

T_d	E	$8C_3$	$3C_2$	$6S_4$	$6\sigma_d$
A_1	1	1	1	1	0
A_2	1	1	1	-1	-1
E	2	-1	2	.	0
T_1	3	0	-1	1	-1
T_2	3	0	-1	-1	1

Table 1.4 Character table for tetrahedral (T_d) symmetry in the double group

T_d	E	$\bar{E}$	$8C_3$	$8\overline{C_3}$	$3C_2$ $3\overline{C_2}$	$6S_4$	$6S_4$	$3\sigma_d$ $3\overline{\sigma_d}$
A_1	1	1	1	1	1	1	1	1
A_2	1	1	1	1	1	-1	-1	-1
E	2	2	-1	-1	2	0	0	0
T_1	3	3	0	0	-1	1	1	-1
T_2	3	3	0	0	-1	-1	-1	1

Really interesting interplay between crystal field splitting and symmetry comes about when an ostensibly high-symmetry crystal field coordination sits on a Wycoff site with lower symmetry. For example, a 4-ligand coordinated tetrahedral ion could sit on the 2*a* or 2*b* Wycoff position in a unit cell with $P6_3mc$ space group symmetry. In this case, the double group T_d IR's would be symmetry-allowed to decompose into C_{3v} symmetry. The details of how these IRs decompose has been helpfully tabulated in the book *Properties of the thirty-two point groups* by George F. Koster (1963) [9]. The decomposition of T_d to its subgroups, may be found in Table 1.5. In the case of C3v, the singlets Γ_1 and Γ_2 remain as Γ_1 and Γ_2, the doublet Γ_3 remains a Γ_3, the triplet Γ_4 decomposes into a singlet Γ_2 and doublet Γ_3 and the triplet Γ_5 decomposes into a singlet Γ_1 and doublet Γ_3. So, for a CN=4 "tetrahedral" ion on the 2*a* or 2*b* Wycoff position, all doublets will behave symmetrically as Γ_3 and there are no triplets, in contrast to

the CN=4 tetrahedral ion on a T_d site which would have, symmetrically, one kind of doublet (Γ_3) and two kinds of triplets (Γ_4 and Γ_5).

Table 1.5 Decomposition of T_d and O IR's into various subgroups, one of which is C_{3v}.

T_d	O	Γ_1	Γ_2	Γ_3	Γ_4	Γ_5	Γ_6	Γ_7	Γ_8
C_{3v}	D_3	Γ_1	Γ_2	Γ_3	$\Gamma_2 + \Gamma_5$	$\Gamma_4 + \Gamma_5$	Γ_4	Γ_4	$\Gamma_4 + \Gamma_5 + \Gamma_6$
T	T	Γ_1	Γ_1	$\Gamma_2 + \Gamma_3$	Γ_4	Γ_4	Γ_5	Γ_5	$\Gamma_6 + \Gamma_7$
C_{2v}		Γ_1	Γ_3	$\Gamma_1 + \Gamma_3$	$\Gamma_2 + \Gamma_3 + \Gamma_4$	$\Gamma_1 + \Gamma_2 + \Gamma_4$	Γ_5	Γ_5	$2\Gamma_5$
D_{2d}	D_4	Γ_1	Γ_3	$\Gamma_1 + \Gamma_3$	$\Gamma_2 + \Gamma_5$	$\Gamma_4 + \Gamma_5$	Γ_6	Γ_7	$\Gamma_6 + \Gamma_7$

The symmetry decomposition on the Wycoff sites is particularly relevant for determining the ground state of a real system with crystal field splitting, spin orbit coupling, and ligand distortion.

Continuing in the example of a CN=4 tetrahedral ion on the 2*b* site in *P*6$_3$*mc*, let us consider that the ion is Ni^{2+}.Liehr and Ballhausen published the Complete Theory of Ni(II) and V(III) in Cubic Crystalline Fields [10] , and collected their results in Tanabe-Sugano diagrams to which we can refer (rather than arduously work out again). Their diagram of Ni^{2+} in a tetrahedral field is duplicated for convenience in Figure 1.9.

In Figure 1.9, the lowest energy state is a singlet Γ_1, 44 meV above is a Γ_4, and then 72 meV above this Γ_4 are Γ_3 and Γ_5 states. A tetragonal distortion from T symmetry to C_{3v} symmetrically allows the T Γ_4 and Γ_5 states to split into Γ_2+Γ_3 and Γ_1+Γ_3, respectively. Ligand distortions and spin orbit coupling can cause

these singlet+doublet states to split further, and the ground state could easily become a doublet Γ_3. Thus, an understanding of the double group symmetries of the Wycoff sites and thoughtful decomposition of the symmetries present in materials is an important part of understanding 'designable' material properties.

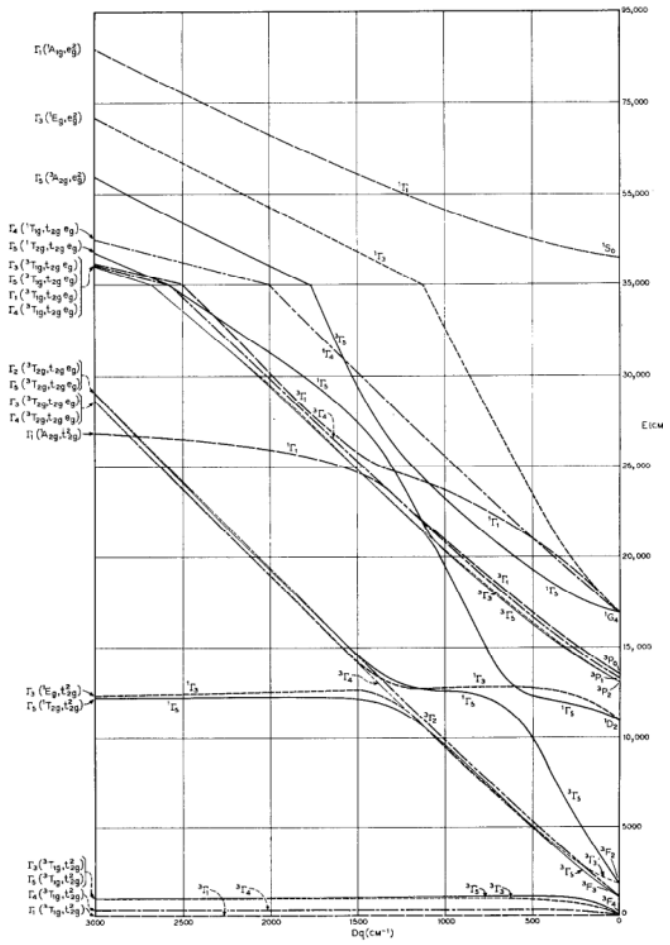

Figure 1.9 Tetrahedral Tanabe-Sugano diagram, duplicated from Liehr and Ballhausen (1953). [10]

Section 1.4 Synthesis

The methods employed in traditional ceramic methods are designed to overcome energy barriers and promote diffusion of elements through the reacting solids. Typical solid state methods involve thoroughly grinding stoichiometric ratios of powdered reactants together and reacting them in sealed ampoules under vacuum or in non-reactive vessels under atmospheric conditions at elevated temperatures for periods of 12+ hours. The temperatures used in solid state reactions are generally much higher than those used in other areas of chemistry, often in excess of 1000 °C.

Some specific techniques can be used to promote the rapid synthesis of phase-pure products. An excellent example of a material made phase-pure by the employment of these methods is $FeSc_2S_4$, the subject of Chapter 3 of this work. Surfaces and interfaces are where reactions happen, and many solid state techniques are designed to promote reactions by increasing reactant surface area. Surfaces are where reactions happen! Compressing powdered reactants also promotes the rate of reactions by reducing barriers to diffusion and putting more surfaces in contact.

Another important component of successful reactions is the set of starting materials. Some materials, like KV_3Sb_5, discussed in Chapter 4, can be made from

elemental starting materials. For others, like $FeSc_2S_4$ and $Ni_2Mo_3O_8$, a mix of sulfides or oxides is used: $FeSc_2S_4$ is made from FeS and Sc_2S_3 (which are, in turn, made by reacting elemental reactants), and $Ni_2Mo_3O_8$ is made from NiO and MoO_2. Conceivably, $Ni_2Mo_3O_8$ could be made from a mixture of MoO_3 and NiO and Ni, but competing side reactions occur.

In Chapter 3, the crystal growth of FeSc2S4 is discussed. This crystal growth was enabled by the use of a modified Bridgman traveling solvent floating zone method. The choice of solvent is critical to the success of this method. In the case of $FeSc_2S_4$, FeS was used as the solvent. This solvent melts at a temperature at which stoichiometric $FeSc_2S_4$ can crystallize. Dr. Seyed Koohpayeh at the Institute for Quantum Matter is a pioneer in traveling solvent floating zone growths and was instrumental to the success of the growths described in Chapter 3.

Section 1.5 Materials Characterization Techniques

1.5.1 Structural Characterization

Long-range and average structure: X-ray and neutron diffraction

X-ray and neutron diffraction are complementary techniques for determining the average long range ordered nuclear structure of a material. X-rays diffract off of the electron clouds around nuclei, while neutrons diffract off of the nuclei

themselves. The intensity of X-rays decreases with an angular dependence of $\sin(\theta)/\lambda$; neutrons, however, have element and isotope dependent coherent and incoherent scattering cross sections that dictate the strength of scattering. In general, neutron sources are much less brilliant than X-ray sources, so signal strength can be a challenge in neutron scattering experiments.

The diffraction pattern that we observe depends on (1) material properties, (2) instrumental setup, and (3) sample preparation.

Material properties are those structural components inherent to the material that, ideally, are independent of sample preparation, but can depend on thermodynamic variables like the temperature of measurement, air pressure, etc. These are: lattice parameters (a, b, c), structural angles (α, β, γ), average atomic positions and occupancies, and atomic displacement parameters (formerly called and occasionally still referred to as thermal parameters, B and/or U).

The instrumental parameters such as the type of incident radiation, the type of detector, the resolution, and time of exposure affect the peak shapes in the diffraction pattern. Some material properties and sample preparation techniques also affect peak shape. The instrumental parameters, though, are theoretically 'knowable' and can be accounted for.

Sample preparation considerations are different for different geometries of measurement. For example, effects like sample height offsets, surface roughness,

and preferred orientation are very visible for the Bragg-Brentano geometry (our in-lab geometry), but are not for a rotating sample in Debye-Scherrer geometry used for diffraction at a variety of beamlines at national laboratory facilities.

Table 1.6 Summary of peak attributes and their causes

	Category	Affected by…
Peak Area	Material	Contents of unit cell
	Sample	Phase amount in mixture
Peak Shape and width	Sample	Crystallite size
	Sample/material	Strain
	Sample/material	Disorder
	Sample	Surface Roughness/Absorption
	Sample	Preferred Orientation
	Instrument	Finite source size
	Instrument	Axial Divergence
	Instrument	Slits
	Instrument	Detector resolution
Peak Position	Material	Lattice parameters
	Sample	Sample height offset

Magnetic Structure Determination

Just as X-rays and neutrons diffract off of long-range nuclear (structural) order, they also diffract off of long-range magnetic order that appears at temperatures below magnetic ordering phase transitions. It is far more common to use neutrons to study magnetic structure as the scattering factor of neutrons off of

magnetic order is approximately 1000 times greater than that of X-rays, though some X-ray techniques, such as X-ray resonance diffraction, are in use.

Magnetic order can be either commensurate, with periodicity the same as unit cell periodicity, or incommensurate, where the periodicity of the magnetic order is not the same as the periodicity of the underlying unit cell. Magnetism is not the only kind of incommensurate structure to be found in crystallography: defects and local distortions can have incommensurate order as well. In general, incommensurate structures require a much more complicated theoretical treatment.

There is a variety of software available for solving magnetic structures, all of which can be used for solving nuclear structures as well: GSAS [11] with EXPGUI [12] (free, uses 'dummy' nuclear atoms), FullProf [13] (free, commensurate and incommensurate structures), and TOPAS (not free, commensurate only). FullProf is the best free software for solving magnetic structures. Rather than defining each magnetic atom in the expanded unit cell, it populates structures using $\vec{k}$ propagation vectors. The $\vec{k}$ vector describes how the unit cell expands from the structural unit cell to the magnetic unit cell. For example, a $\vec{k}$ vector of (1/2 0 0) corresponds to a magnetic unit cell that is the same as the structural unit cell doubled in the *a* direction, a $\vec{k}$ vector of (1/2 1/2

1/3) is doubled in the *a* and *b* directions and tripled in the *c* direction, etc. The d-spacings of the magnetic Bragg peaks are used to determine the magnetic supercell and $\vec{k}$ vector. A magnetic Bragg peak appearing at d = 2**a*, for example, might suggest a doubling of the unit cell in *a*. In general, the largest $\vec{k}$ vector is the 'correct' one because it is the smallest real space distance that can describe the order.

SARAh [14] is a program that uses Representation Theory to generate symmetric irreducible representations (IR's) that can describe the symmetry of the ordered state, with the input of the magnetic $\vec{k}$ vector, the space group, and the atomic positions of the magnetic ions. According to Landau theory, one IR should be sufficient to describe the symmetry of the ordered state. Each IR has some number of components, and FullProf refines the coefficients of these components. Depending on the input parameters, there may be many IR's that need to be sifted through to find the correct one, requiring hundreds of refinements. There is a thorough worked example in Chapter 2.

Local nuclear and magnetic structure probes

There is a plethora of techniques available for analysis of the local structure of materials. One of the most popular is Pair Distribution Function (PDF) Analysis, which can be done with both X-rays and neutrons. PDF data is collected as

diffraction data in Q-space (related to θ as |Q| = $(4\pi/\lambda)\sin(2\theta/2)$), then Fourier transformed into real space (r). Because of the mathematical processing, the resolution in r is dependent on the Q-range of the measurement. The equation for G(r) that is plotted for PDF analysis describes the number of atoms at distance r away from a given atom, relative to a totally amorphous solid:

$$G(r) = \frac{2}{\pi}\int_0^{Q_{max}} Q(S(Q) - 1)\sin(Qr)\, dQ$$

X-Ray PDF can be done on both in-house and at synchrotron sources, like at the 11-ID-B beamline at Argonne National Laboratory. Lower intensity sources with Ag or Mo sources are available for universities, but generally suffer from a very small Q-range available for sampling, which, as mentioned above, severely limits the resolution. Neutron PDF is useful in the same way that neutron diffraction is a complementary technique to XRD: despite the low brilliance of neutron sources, the difference in scattering factors makes it very useful for seeing specific elements, particularly lighter elements such as oxygen.

1.5.2 Physical Properties Characterization

Heat Capacity

Heat capacity is a powerful tool for understanding energy scales of interactions in materials. The constituent atoms of the lattice vibrate in symmetry-allowed acoustic and optic excited states which behave as quasiparticles and are called

phonons. Phonons have characteristic energies of interaction and if the thermal energy provided by the surroundings to the material goes below the energy of the phonon then the phonon will 'freeze out'. This is why heat capacity generally increases from low temperature to high temperature: increasing the temperature increases the number of phonons in the solid. There are many other quasi-particles of condensed-matter interest such as magnons and excitons that will be discussed later.

One of the ways that we most often use a heat capacity measurement is to identify transitions and quantify their entropy. We are able to do this because of the thermodynamic relationship:

$$\Delta S_{T_1 T_2} = \int_{T_1}^{T_2} \frac{C_p}{T}$$

where $\Delta S_{T_1 T_2}$ is the change in entropy across the temperature range T_1 to T_2 and C_p is the constant-pressure heat capacity that we routinely measure using our in-house instrumentation. The entropy of a given transition can be calculated by essentially accounting for the microstates associated with the transition, which can be expressed as $\Delta S = Rln(\Omega)$ where Ω is the number of microstates. For example, for an Fe^{2+} magnetic system, the microstates for $S = 2$ are $s = 2, 1, 0, -1, -2$, and $\Delta S = Rln(5)$.

When the transition under consideration is a magnetic transition, it is often useful to measure a non-magnetic analog to isolate only the magnetic contribution to the heat capacity. The choice of an appropriate non-magnetic analog is critical for obtaining an as-accurate-as-possible determination of the magnetic contribution. The analog is generally a chemically similar material where non-magnetic atoms have been substituted for magnetic units. For example, and as will be discussed in subsequent chapters, $Zn_2Mo_3O_8$ was a good choice of non-magnetic analog for $Ni_2Mo_3O_8$ because zinc and nickel are similar in mass and Zn^{2+} has no unpaired, magnetically active electrons. For $MgNiMo_3O_8$, the phonon subtraction was found by averaging the measured heat capacities of $Mg_2Mo_3O_8$ and $Zn_2Mo_3O_8$. The Mg in $Mg_2Mo_3O_8$ was too dissimilar from the Ni and the Zn in $Zn_2Mo_3O_8$ to dissimilar from the Mg in $MgNiMo_3O_8$, but the average of the two measurements served as an excellent non-magnetic subtraction.

The small differences in mass between substituted elements can be accounted for using a scaling factor of the form:

$$\frac{\Theta^3_{L_mY_sZ_p}}{\Theta^3_{X_mY_nZ_q}} = \frac{mM_X^{3/2} + nM_Y^{3/2} + qM_Z^{3/2}}{mM_L^{3/2} + sM_Y^{3/2} + pM_Z^{3/2}}$$

To scale the atoms in material $L_mY_sZ_p$ to material $X_mY_nZ_q$where $\Theta_{L_mY_sZ_p}$ is the Debye temperature of $L_mY_sZ_p$ and M_X is the molar mass of element X (and similarly for elements L, Y, etc.). Both the heat capacity and the temperature should be scaled by this factor.

Magnetization

Materials can be diamagnetic, paramagnetic, ferromagnetic, or antiferromagnetic; there are many resources that quite ably describe their characteristics. All materials with more than one electron are somewhat diamagnetic: paired electrons in orbitals with no net magnetic moment produce a weak negative moment under an applied field. But diamagnetism is often significantly weaker than other types of magnetism, so is often only observed in their absence.

A system selects a magnetically ordered state to lower inherent magnetic degeneracy and thereby lower the overall energy of the system. The magnetically ordered state that the system selects depends on the magnitude and nature of the magnetic interactions (J_1, J_2, …, J_i) between magnetic units in the material. The temperature of a transition is characteristic of the strength of the magnetic interactions – a material can magnetically order when the energy of the magnetic interactions is greater than the thermal fluctuations. Above this temperature, a

magnetic material shows paramagnetic (disordered) behavior. The ordering temperature for a ferromagnetic transition is called the Curie temperature (T_C), while that of an antiferromagnet is the Néel Temperature (T_N).

The Curie-Weiss law can be used to analyze the paramagnetic response of a material to quantify the interaction strength, temperature independent contribution to the magnetism (χ_0), and the magnetic moment. It takes the form:

$$\chi_m = \frac{C}{T - \theta_W} + \chi_0$$

The Weiss temperature is a measure of the type and strength of the magnetic interactions. In the case of non-interacting spins the Weiss temperature $\theta_W = 0$. Stronger interactions correspond to further divergence from 0; spins that tend to align in the same direction will have $\theta_W > 0$ and spins that tend to align in opposing directions will have $\theta_W < 0$. The Curie constant, C, is related to the effective magnetic moment as $p_{eff} = \sqrt{8C}$. This equation is particularly useful for analyzing data plotted as $1/\chi_m$ versus T, where "Curie-Weiss behavior" is linear. In the case of impurity spins, the inclusion of a temperature independent χ_0 term is sometimes necessary.

The effective magnetic moment is related to the spin quantum number S (equal to half of the number of unpaired electrons per unit) as:

$$p_{eff} = g\sqrt{S(S+1)}$$

Where g is the gyromagnetic ratio of the electron and is normally ~ 2. This is the spin-only case where the orbital angular momentum is totally quenched. In the case that there is un-quenched orbital moment:

$$p_{eff} = g\sqrt{J(J+1)}$$

Where $J = L + S$ and L is the orbital angular momentum quantum number. The effective magnetic moments of various transition metal ions are shown in Table 1.7.

Table 1.7 Experimental and theoretical values of μ_{eff} for some transition metal ions. Reproduced from Smart, 1966 [15].

Ion	S	L	J	$g\sqrt{J(J+1)}$	$2\sqrt{S(S+1)}$	μ_{eff}(exp)
Ti^{3+}, V^{4+}	½	2	3/2	1.55	1.73	1.8
V^{3+}	1	3	2	1.63	2.83	2.8
Cr^{3+}, V^{2+}	3/2	3	3/2	0.77	3.87	3.8
Mn^{3+}	2	2	0	0	4.9	4.9
Fe^{3+}, Mn^{2+}	5/2	0	5/2	5.92	5.92	5.9
Fe^{2+}	2	2	4	6.7	4.9	5.4
Co^{2+}	3/2	3	9/2	6.63	3.87	4.8
Ni^{2+}	1	3	4	5.59	2.83	3.2
Cu^{2+}	1/2	2	5/2	3.55	1.73	1.9

Section 1.6 Conclusion

Using the knowledge introduced in this chapter, three new families of quantum magnets were explored that are described in the following chapters. Chapter 2

discusses the discovery of zig-zag antiferromagnetic order on an integer-spin honeycomb in a non-centrosymmetric space group – the first of its kind – and the successful selective substitution onto one of the two halves of the bipartite honeycomb lattice. Substitution was enabled by differences in coordination environment around the magnetic ions. Chapter 3 is a presentation of the first report of a growth of mm-scale crystals of $FeSc_2S_4$ – a compound that has been of great interest to the quantum materials community for decades. This work enabled the identification of an antiferromagnetically ordered state in this material – suggesting that it is close to, but on the ordered side of, a quantum critical point. Chapter 4 discusses two nascent projects: one on the first metallic kagomé antiferromagnet, and the other on characterization of highly conductive small band-gap semiconducting MOF's. These studies push the boundaries of quantum magnetism and the possibilities of materials design of new quantum materials. Perhaps they will even help us step from the Silicon Age to the Quantum Age.

References

[1] T-H. Han, J. S. Helton, S. Chu, D. G. Nocera, J. A. Rodriguez-Rivera, C. Broholm and Y. S. Lee *Nature*, 492 (2012).

[2] Y. Zhou, K. Kanoda, and T-K. Ng, *Rev. Mod. Phys*. 89, 025003 (2017).

[3] L. Savary and L. Balents, *Rep. Prog. Phys*. 80, 016502 (2016).

[4] B. K. Clark, D. A. Abanin, and S. L. Sondhi, *Phys. Rev. Lett*. 107, 087204 (2011).

[5] A. Kitaev, *Ann. Phys*. 321, 2 (2006).

[6] J. Chamorro, L. Ge, M. Subramanian, M. Mourigal, T.M. McQueen, *Phys. Rev. Materials* **2**, 034404 (2018).

[7] Z. Nussinov and J. van den Brink *Rev. Mod. Phys*. 87, 1 (2015).

[8] edited by Theo Hahn. *International Tables for Crystallography. Volume A, Space-Group Symmetry.* Dordrecht. London :Published for the International Union of Crystallography, Kluwer Academic Publishers (2002).

[9] Koster, George F., *Properties of the thirty-two point groups*, Cambridge, Mass., M. I. T. Press (1963).

[10] A. D. Liehr and C. J. Ballhausen. *Ann. Phys*, 2, (1959).

[11] A.C. Larson and R.B. Von Dreele, Los Alamos National Laboratory Report LAUR 86-748 (2000).

[12] B.H. Toby, J. Appl. Cryst. 34, 210 (2001).

[13] Rodrigues-Carvajal, Phys. B 192, 55 (1993).

[14] Wills, A. S. Physica B, 276 (2000).

[15] J. S. Smart, *Effective Field Theories of Magnetism*, W. B. Saunders Company (1966).

Chapter 2 $Ni_2Mo_3O_8$: zig-zag antiferromagnetic order on an integer-spin non-centrosymmetric honeycomb lattice

This work was co-written with the following authors and has been submitted to Physical Review Materials

Jennifer R. Morey[a,b] Allen Scheie[b], John P. Sheckelton[a,b], Craig M. Brown, and Tyrel M. McQueen[a,b,d]

[a] Department of Chemistry, Johns Hopkins University, Baltimore, Maryland 21218, USA

[b] Department of Physics and Astronomy, Institute for Quantum Matter, Johns Hopkins University, Baltimore, Maryland 21218, USA

[c] National Institute for Standards and Technology, Gaithersburg, MD 20899 USA and Department of Chemical and Biomolecular Engineering, University of Delaware, Newark, Delaware, 19716 USA

[d] Department of Materials Science, Johns Hopkins University, Baltimore, Maryland 21218, USA

Section 2.1 Introduction

Theoretical studies have predicted the existence of topological magnons in honeycomb compounds with zig-zag antiferromagnetic (AFM) order. Here we report the discovery of zig-zag AFM order in the layered and non-centrosymmetric honeycomb nickelate $Ni_2Mo_3O_8$ through a combination of magnetization, specific heat, x-ray and neutron diffraction and electron paramagnetic resonance measurements. It is the first example of such order in an integer-spin non-centrosymmetric honeycomb structure ($P6_3mc$). Further, each of the two distinct sites of the bipartite honeycomb lattice has a unique crystal field environment, octahedral and tetrahedral Ni^{2+} respectively, enabling independent substitution on each sublattice. Replacement of Ni by Mg on the octahedral site suppresses the long range magnetic order and results in a weakly ferromagnetic state. Conversely, substitution of Fe for Ni enhances the strength of the AFM exchange and increases the ordering temperature. Thus $Ni_2Mo_3O_8$ provides a platform on which to explore the rich physics of $S = 1$ on the honeycomb lattice in the presence of competing magnetic interactions with a non-centrosymmetric, formally piezo-polar, crystal structure.

The prediction and discovery of topological phenomena in materials has ignited a global search for new quantum materials and states of matter [1, 2], with potential applications in quantum computing and information storage. The physical realization of theoretically proposed topological states requires the ability to produce materials with highly controlled structural, electronic, and magnetic properties. Most materials release inherent magnetic degeneracy at sufficiently low temperatures by mechanisms such as structural phase transitions, local magnetic ordering, and changes in the degree of electron localization (e.g. by formation of singlet pairs with neighboring ions), but there are some states of matter postulated to retain finite degeneracy to $T = 0$ K, such as quantum spin liquids (QSL's) [3-6].

One of the main structure types known to host quantum frustrated magnetic topological phenomena is the 'honeycomb' structure, which is a two dimensional bipartite lattice. Unlike the triangular lattice or spinel structure, the honeycomb is not inherently geometrically frustrated, but becomes frustrated in the presence of competing longer range magnetic interactions or anisotropic magnetic exchanges.

One example of this is the ruthenium honeycomb in α-$RuCl_3$ which may host almost exactly the interactions that would allow a finite degenerate

quantum spin liquid (Kitaev QSL) state to emerge [7-11]; it is suggested that it is the strong next-nearest neighbor and next-next-nearest neighbor interactions that stabilize the frustration [12, 13]. Furthermore, extensive experimental and theoretical investigations into iridium honeycomb compounds Li_2IrO_3 [14-18] and Na_2IrO_3 [19-23] have realized many of the types of magnetically ordered states that are proximal to QSL states – i.e. stripy antiferromagnetic (AFM), zig-zag AFM, and Néel AFM [24-29].

The nature of the spin interaction, relevant magnetic exchanges, structural geometry, order, symmetry, and spin orbit coupling (SOC) influence the magnetic ground state of a compound. SOC generally increases with atomic number and becomes a controlling factor in 4d and 5d transition metal honeycombs, particularly those incorporating iridium and ruthenium. Strong SOC has been posited as the reason that iridium honeycombs have a ground state that is magnetically ordered rather than a QSL [29].

Despite having weaker SOC than the 4d or 5d equivalents, 3d ions with strong anisotropy, e.g. Co^{2+}, may also harbor strong bond-dependent interactions between ions [30, 31]. Further, recent theoretical predictions have shown that honeycomb compounds with zig-zag AFM and stripy AFM order may host

topologically non-trivial magnons that are robust under Dzyaloshinskii-Moriya interactions [32, 33].

Here we report that $Ni_2Mo_3O_8$, which contains a honeycomb of $S = 1$ Ni^{2+} ions and has previously been reported to remain paramagnetic down to $T = 2$ K [34], undergoes a transition to a zig-zag ordered antiferromagnetic state below $T_N = 6$ K, and is thus a candidate for harboring topological excitations. Compared to other nickel compounds known to have zig-zag antiferromagnetic order, including $BaNi_2V_2O_8$, $BaNi_2As_2O_8$, $Na_3Ni_2BiO_6$, $A_3Ni_2SbO_6$ (A = Li, Na), and $Cu_3Ni_2SbO_6$ [35-37], $Ni_2Mo_3O_8$ is unique in that the two triangular sublattices of the honeycomb have different local coordination environments of the Ni^{2+} ions (octahedral and tetrahedral), permitting selective replacement of one of the two halves of the bipartite lattice. Additionally, it is the first example of zig-zag AFM order in a non-centrosymmetric $S = 1$ honeycomb material, complementing the only other known non-centrosymmetric zig-zag antiferromagnetic material, $Na_2Co_2TeO_6$, with $S = 3/2$.

In $Ni_2Mo_3O_8$ substitution of non-magnetic Mg^{2+} on the tetrahedral site removes long range magnetic order, with remnant small ferromagnetic interactions between Ni^{2+} ions. In contrast, substitution of $S = 2$ Fe^{2+} for Ni^{2+} results in a large increase in the antiferromagnetic ordering temperature to

T_N = 50 K. $Ni_2Mo_3O_8$ is a realization of zig-zag order in a non-centrosymmetric antiferromagnet; The ability to selectively substitute one of the two sites in the honeycomb make this material an excellent platform from which to investigate the underlying physics of the selection of magnetic ground states on the honeycomb lattice.

Section 2.2 Experimental Methods

2.2.1 Powder Synthesis

$M_2Mo_3O_8$, M = (Mg, Ni, Fe, Zn), were synthesized by intimately mixing MO or M_2O_3 and MoO_2 with a small stoichiometric excess of MO where M = (Mg, Ni) in an agate mortar and pestle, followed by compression into a pressed pellet and sealing in an alumina crucible in a quartz ampoule evacuated to 10^{-2} torr. The samples were first heated at 200 °C/hr to 950 °C, held at that temperature overnight, and then quenched by removal of the quartz ampoule from the furnace to the benchtop to cool. Successive regrinding, repressing, resealing, and overnight reheating cycles, with the sample placed directly into and removed from a furnace at T = 950 °C, were performed until phase purity was achieved. Purity was checked with Rietveld refinements of powder x-ray diffraction (PXRD) patterns.

2.2.2 Nuclear and Magnetic Structural Characterization

PXRD patterns were collected on a Bruker D8 Focus diffractometer with a LynxEye detector using Cu Kα radiation. Rietveld refinements were performed using Topas 4.2 (Bruker). Powder neutron diffraction (PND) experiments on $Ni_2Mo_3O_8$ and $MgNiMo_3O_8$ were performed at the National Institute for Standards and Technology Center for Neutron Research on the BT-1 powder diffractometer using the Ge311 monochromator, 60′ collimation, and a wavelength $\lambda_{neutron}$= 2.0775 Å. Nuclear structural refinements were performed using GSAS [38] and EXPGUI [39] and cross referenced with structural refinements done in the FullProf Suite [40]. Time of flight neutron powder diffraction experiments were done at the high resolution powder diffractometer POWGEN at Oak Ridge National Laboratory using Frame 1.5 at T = 10 K and T = 300 K. LeBail unit cell refinements were used to account for starting material (NiO, MgO, MoO_2) and side product ($NiMoO_4$) impurities, present at the < 2% level.

The magnetic unit cell was manually indexed using GSAS and EXPGUI and confirmed using k-search in the FullProf suite. SARAh Representational Analysis software [41] and FullProf were used in tandem to determine the final structure. Structures were visualized using Vesta software [42].

2.2.3 Physical Properties Characterization

Magnetization and heat capacity measurements were done using a Quantum Design Physical Properties Measurement System. Temperature dependent magnetization data were collected from T = 2-300 K under applied fields of $\mu_0 H$ = 0.5 and 1 T. Susceptibility was computed as $\chi = \Delta M/\Delta H$ numerically from the two fields for each temperature. The 0.5 T and 1 T fields were chosen as representative of a linear portion of the magnetization curve. Curie-Weiss analysis was performed over the temperature range 150 K < T < 300 K after linearization of susceptibility data with a temperature independent χ_0.

Zero field heat capacity was collected from T = 2 to T = 300 K for $Ni_2Mo_3O_8$ and to T = 150 K for $MgNiMo_3O_8$ and $FeNiMo_3O_8$ using the semi-adiabatic pulse technique with a 2% temperature rise and measurement over 3 time constants in time. Measurements were performed in triplicate. Field-dependent heat capacity was collected up to $\mu_0 H$ = 5 T from T = 2 to T = 20 K. $Ni_2Mo_3O_8$ and $MgNiMo_3O_8$ were measured as pressed pellets, while $FeNiMo_3O_8$ was pressed with clean silver powder. The heat capacity of silver is well known and was subtracted from the raw data. Heat capacity measurements in the T = 150 mK – 3.5 K range were done on a Quantum Design Dilution Refrigerator (DR) using the semiadiabatic pulse technique with a 2% temperature rise and measurement over 3 time constants in

time. Measurements were performed in triplicate. DR samples were pressed with clean silver powder to enhance thermal conductivity with the stage. The heat capacity of silver was measured and subtracted from the raw signal.

The phononic contribution of $Ni_2Mo_3O_8$ was found by scaling the measured heat capacity of $Zn_2Mo_3O_8$ for the mass difference between nickel and zinc [43]. Similarly, the phononic contribution to the heat capacity of $MgNiMo_3O_8$ was found as the average of measurements on $Mg_2Mo_3O_8$ and $Zn_2Mo_3O_8$, scaled to account for the mass differences in the stoichiometric formulae. Literature reports on $Fe_2Mo_3O_8$ were used to scale measurements taken on $Zn_2Mo_3O_8$ manually to find the phonon contribution in $FeNiMo_3O_8$ [44].

2.2.4 Calculation Methods

The energy splitting of the Ni^{2+} ions was calculated with a point charge model [45] using the PyCrystalField software package [46]. We built crystal electric field models using the ligand positions determined from the neutron diffraction experiments, and calculated the eigenstates of a single-ion Hamiltonian with crystal fields and spin orbit coupling treated non-perturbatively.

The crystal electric field (CEF) Hamiltonian can be written as $H_{CEF} = \sum_{nm} B_n^m O_n^m$ where O_n^m are Stevens Operators and B_n^m are multiplicative CEF parameters. To calculate the energy level splittings, we computed the single-ion eigenstates using

PyCrystalField [46]. This code is based on the method outlined in Hutchings (1964), which estimates the CEF Hamiltonian by treading ligands as point charges using Stevens Operators formalism. To fully account for spin-0orbit interactions, we calculated the singe-ion Hamiltonian in the intermediate coupling scheme by expressing the crystal fields by interacting the orbital angular momentum L and adding spin orbit coupling $H_{SOC} = \lambda S \cdot L$ non-perturbatively to the Hamiltonian so that $H = H_{SOC} + H_{CEF}$. From here, the eigenvalues and eigenvectors are calculated by diagonalizing the Hamilonian. These are shown in Figure 2.12. Values of λ and Ni^{2+} radial integrals were taken from Abragam and B. Bleaney (1970).

Section 2.3 Results

2.3.1 Nuclear Structural Determination

$Ni_2Mo_3O_8$, $MgNiMo_3O_8$, and $FeNiMo_3O_8$ are isostructural and are comprised of alternating layers of hexagonal honeycomb and trimerized molybdenum oxide layers. Analyses of NPD (Figure 2.3(a-b)) and PXRD patterns support that $Ni_2Mo_3O_8$, $MgNiMo_3O_8$, and $FeNiMo_3O_8$ crystallize in the non-centrosymmetric hexagonal space group 186, $P6_3mc$, Table 2.1.)

The honeycomb lattice is a bipartite lattice comprised of two triangular sublattices. In $Ni_2Mo_3O_8$, one triangular sublattice is octahedrally coordinated Ni^{2+} and the other is tetrahedrally coordinated Ni^{2+}, making this material an

integer-spin honeycomb (Figure 2.3(c)). In $MgNiMo_3O_8$, 86(3)% of the *2b* octahedral sites and 14(3)% of the *2b* tetrahedral sites are occupied by nickel, and 14(3)% and 86(3)% of these sites, respectively, are occupied by non-magnetic magnesium ions. The sensitivity of the fit statistics to changes in stoichiometry is shown in Figure 2.1.

The fit statistic $\chi^2$is calculated as $\chi^2 = \frac{1}{N}\frac{\Sigma_i\left(I_{C,i}-I_{O,i}\right)^2}{\sigma^2[I_{O,i}]}$ where N is the number of points less the number of refined parameters (for all fits, N >> number of refined parameters), $I_{C,i}$ is the calculated intensity at each point i, $I_{O,i}$ is the observed intensity at each point i, and σ is the standard deviation:

The fit statistic wRp is calculated as $wRp = \sqrt{\frac{\Sigma_i w_i\left(I_{C,i}-I_{O,i}\right)^2}{\Sigma_i w_i (I_{O,i})^2}}$

the weighting factor $w_i = 1/\sigma^2[I_{O,i}]$.

The fit statistic Rp is calculated as $Rp = \sqrt{\frac{N}{\Sigma_i w_i (I_{O,i})^2}}$

At T = 15 K, the oxygen ligands on the 2*b* Wycoff position in $Ni_2Mo_3O_8$ are slightly distorted in the *c*-direction from their ideal positions around the nickel sites. In the octahedron, the O-Ni-O angle is 88.2(2)° rather than the ideal 90°. In

the tetrahedron, the O-Ni-O angle is 114.52(14)°, rather than the ideal 109.5°. This distortion has an anisotropic temperature dependence, shown in Figure 2.4. The *c* lattice parameter decreases almost linearly from T = 300 K to T = 15 K, while the *a* lattice parameter decreases more rapidly than *c* from T = 300 K to T ~ 180 K and remains relatively constant from T = 150 K to T = 15 K. The ratio of the lattice parameters *a*/*c* over temperature in the lower panel of Figure 2.4 is particularly instructive: it increases from T = 300 K to T ~ 180 K and decreases from T = 130 K to T = 15 K.

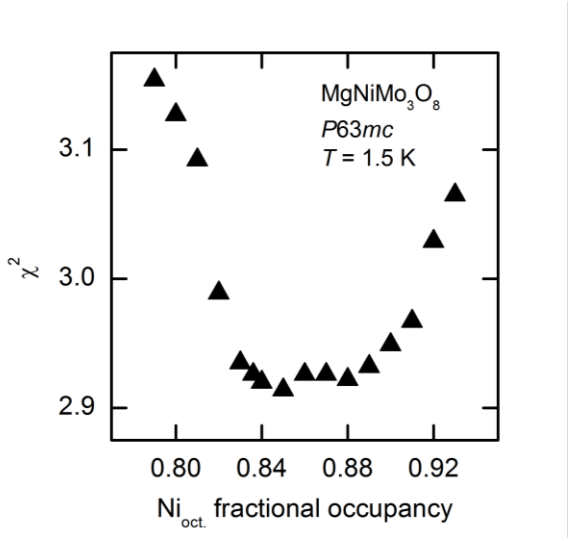

Figure 2.1 Dependence of the fit statistic χ^2 on the fractional occupancy of nickel on the octahedral site of the Mg-Ni honeycomb lattice. Total occupancy of the site was held at 1.

The oxygen ligand crystal field environment is similarly distorted in $MgNiMo_3O_8$ as it is in $Ni_2Mo_3O_8$. In these materials, the oxygen locations can be

precisely located due to the scattering factor contrast available by NPD measurements. $FeNiMo_3O_8$ was characterized using PXRD; the best refinements are obtained with the octahedral site selectively occupied by Fe^{2+} (Table 2.1, refinements plotted in Figure 2.2). The placement of Fe^{2+} on the octahedral site somewhat surprising: while the ionic radius of Ni^{2+} is slightly smaller than that of Fe^{2+} (high spin) in both CN = 4, respectively 0.55 pm and 0.63 pm, and CN = 6, 0.69 pm and 0.79 pm, which would tend to favor placement of Fe^{2+} on the octahedral site, crystal field stabilization energies would favor Ni^{2+} on the octahedral site. Despite this expectation, other data is also consistent with an ordering of the Fe^{2+} and Ni^{2+} ions: there is a sharp antiferromagnetic transition in the susceptibility (see below), which would not be expected if Fe^{2+} and Ni^{2+} were randomly mixed. Thus we assume ordering of Fe^{2+} and Ni^{2+}, but note that site mixing at the 10-20% level cannot be ruled out.

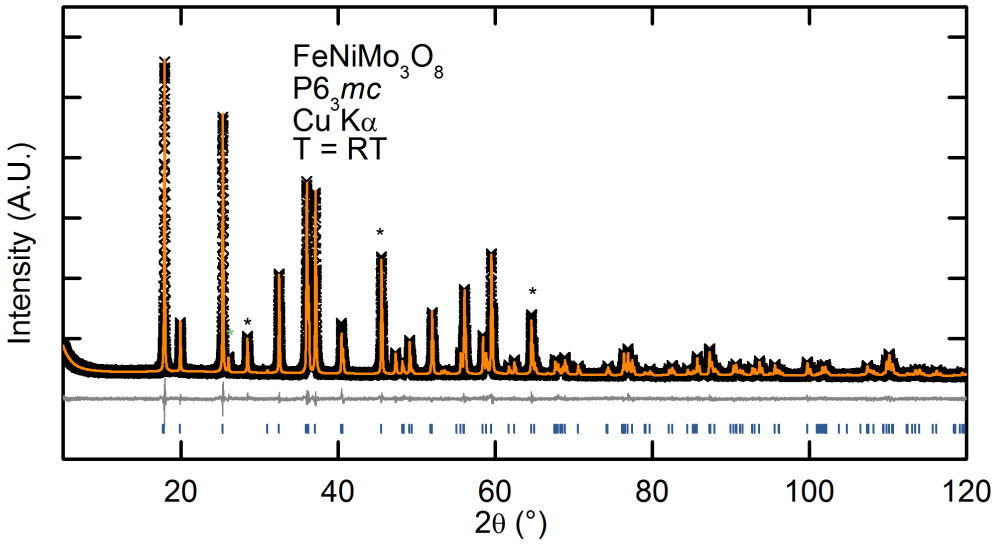

Figure 2.2 Rietveld refinement of P63mc to a room temperature PXRD pattern collected on FeNiMo3O8, measured with Cu Kα radiation. Black asterisks denote a Si standard, and a green asterisk denotes a 1.6 % MoO2 impurity.

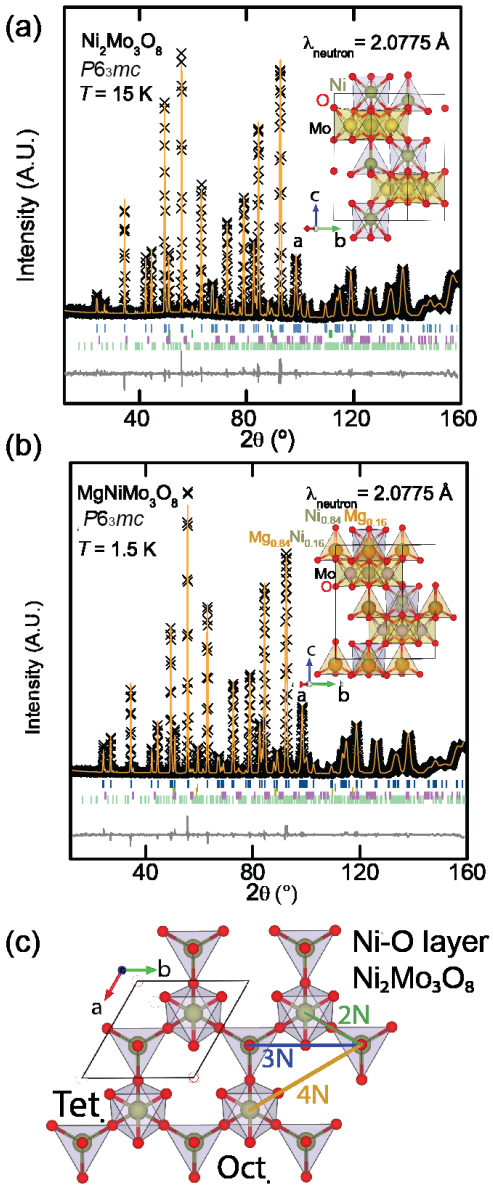

Figure 2.3 Neutron powder diffraction patterns of (a) $Ni_2Mo_3O_8$ and (b) $MgNiMo_3O_8$, refined to the *P6₃mc* space group; Table 2.1. Tick marks in descending vertical display order: $Ni_2Mo_3O_8$ (dark blue), NiO (dark green); MgO (brown); MoO_2 (purple), and $NiMoO_4$ (light green). MgO is not present in the refinement for $Ni_2Mo_3O_8$. (c) Top-down view of the nickel honeycomb lattice, showing alternating adjacent octahedrally and tetrahedrally coordinated atoms and nearest neighbor (2N; 3.384(3) Å), next nearest neighbor (3N; 5.759(5) Å) interactions, and next-next nearest neighbor (4N; 6.680(5) Å) interactions.

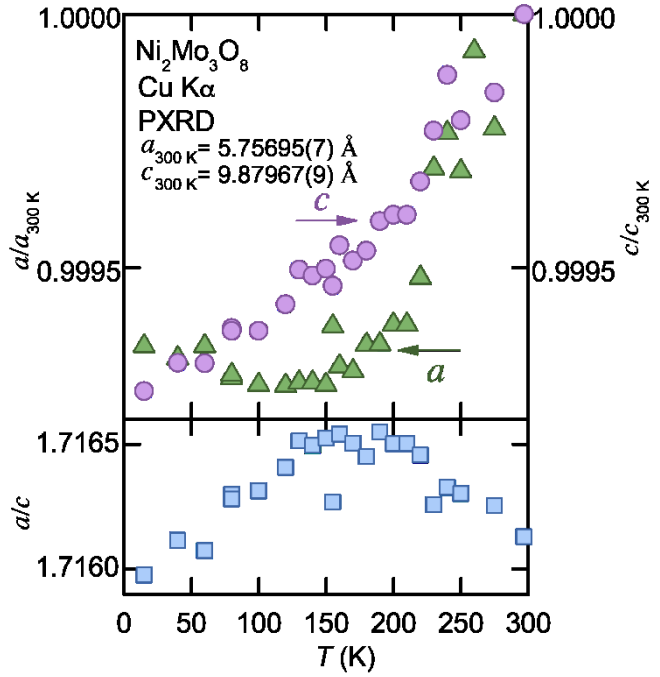

Figure 2.4 Top: temperature dependence of the *a* (green triangles) and *c* (purple circles) lattice parameters of $Ni_2Mo_3O_8$ relative to $T = 300$ K values of 5.75695(7) Å and 9.87967(9) Å, respectively. Bottom: temperature dependence of the ratio of the lattice parameters (blue squares).

Table 2.1 Atomic parameters for structural refinement of (*M1)(M2*)Mo_3O_8, *M1* = (Ni, Mg, Fe), *M2* = Ni; $Ni_2Mo_3O_8$ and $MgNiMo_3O_8$ from NPD at T = 1.5 K and T = 15 K respectively with a neutron wavelength of 2.0775 Å, $FeNiMo_3O_8$ from PXRD at room temperature with $\lambda_{Cu,K\alpha} =$ 1.5406 Å. Occupancies of M1 and M2 are given as (Mg or Fe)/Ni and Ni/(Mg or Fe) respectively.

		$Ni_2Mo_3O_8$	$MgNiMo_3O_8$	$FeNiMo_3O_8$
	a (Å²)	5.74683(5)	5.75166(3)	5.76580(2)
	c (Å²)	9.8626(2)	9.85620(9)	9.90929(3)
	T (K)	15	1.5	295
M1	*x*	1/3	1/3	1/3
2*b*	*y*	2/3	2/3	2/3
	z	0.9480(4)	0.9452(2)	0.9715(2)
	U_{iso}	0.0057(7)	0.0006(4)	0.0109(3)
	Occ.	1	0.86/0.14(3)	1.0(1)/0.0
M2	*x*	1/3	1/3	1/3
2*b*	*y*	2/3	2/3	2/3
	z	0.5116(3)	0.5120(5)	0.5348(2)
	U_{iso}	0.0056(8)	0.00106(4)	0.0109(3)
	Occ.	1	0.86/0.14(3)	1.0(1)/0
Mo	*x*	0.1440(2)	0.14586(9)	0.14688(3)
6*c*	*y*	-0.1440(2)	-0.14586(9)	-0.14688(3)
	z	0.2489(2)	0.25017(14)	0.2733(10)
	U_{iso}	0.0042(7)	0.0002(2)	0.0058(2)
O1	*x*	0	0	0
2*a*	*y*	0	0	0
	z	0.6839(5)	0.3890(3)	0.6165(4)
	U_{iso}	0.008(2)	0.0095(8)	1
O2	*x*	1/3	1/3	1/3
2*b*	*y*	2/3	2/3	2/3
	z	0.1461(4)	0.147(2)	0.1765(4)
	U_{iso}	0.0012(13)	0.0003(5)	1
O3	*x*	0.4880(3)	0.4878(2)	0.4882(2)
6*c*	*y*	-0.4880(3)	-0.4878(2)	-0.4882(2)
	z	0.3659(3)	0.36774(17)	0.3971(4)
	U_{iso}	0.0044(4)	0.0047(3)	1
O4	*x*	0.1688(3)	0.1723(2)	0.1665(3)
6*c*	*y*	-0.1688(3)	-0.1723(2)	-0.1665(3)
	z	0.6342(3)	0.36774(17)	0.6609(2)
	U_{iso}	0.0015(7)	0.0173(4)	1
	wRp	0.0715	0.0415	2.88
	Rp	0.0521	0.0288	2.23
	χ^2	2.526	3.913	1.41

2.3.2 Physical Properties

$Ni_2Mo_3O_8$ and $MgNiMo_3O_8$ both exhibit a peak in heat capacity at T ~ 6 K, Figure 2.5 (a,b). It is at slightly higher temperature and is sharper in $Ni_2Mo_3O_8$, which is consistent with this material being less disordered and having stronger magnetic interactions than $MgNiMo_3O_8$. The application of a $\mu_0 H$ = 5 T magnetic field causes the peak to shift to lower temperatures in $Ni_2Mo_3O_8$ and to higher temperatures in $MgNiMo_3O_8$, which is indicative of antiferromagnetic and ferro/ferrimagnetic interactions, respectively.

Strikingly, $Ni_2Mo_3O_8$ and $MgNiMo_3O_8$ recover the same amount of entropy per magnetic ion by T ~ 150 K. The entropy loss looks to be two step: one degree of freedom is lost between T = 10 K and T = 150 K and two more at the T ~ 6 K transition. The high temperature phonon contribution, calculated from the mass-adjusted measured heat capacity of non-magnetic analogs, describes the high temperature behavior of the materials well. This is highlighted in the insets, which are plotted on a linear temperature scale. There is a large peak in the heat capacity of $FeNiMo_3O_8$ at T ~ 50 K that recovers ΔS = 20.54(5) J mol^{-1} K^{-1}, between T = 2 K and T = 100 K,

Figure 2.6. The phononic background is consistent with reports on the related compound $Fe_2Mo_3O_8$ [44]. The changes in entropy of all three compounds are summarized in Table 2.2.

Table 2.2 Summary of recovered entropy per formula unit (f.u.), shown in Figure 2.5(c) and the lower panel of Figure 2.6.

	ΔS_{mag} (J mol-f.u^{-1}.K^{-1})
$Ni_2Mo_3O_8$	13.9(7)
$MgNiMo_3O_8$	6.9(3)
$FeNiMo_3O_8$	20.5(1.0)

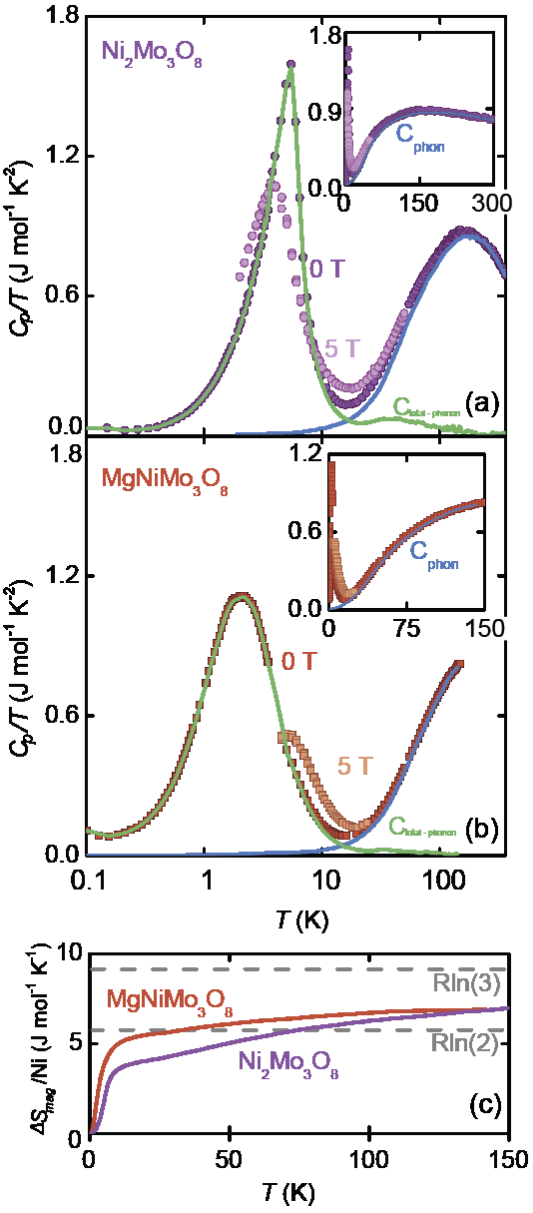

Figure 2.5 (a) Heat capacity over temperature versus the logarithm of temperature of $Ni_2Mo_3O_8$ (top panel, purple circles) and (c) $MgNiMo_3O_8$ (brown squares). Magnetic heat capacity (green curve) found by subtracting the phononic contribution (blue curve) determined from measured non-magnetic analog materials. Insets: Heat capacity over temperature versus linear temperature, highlighting the high temperature phonon contribution. (c) Entropy as a function of temperature.

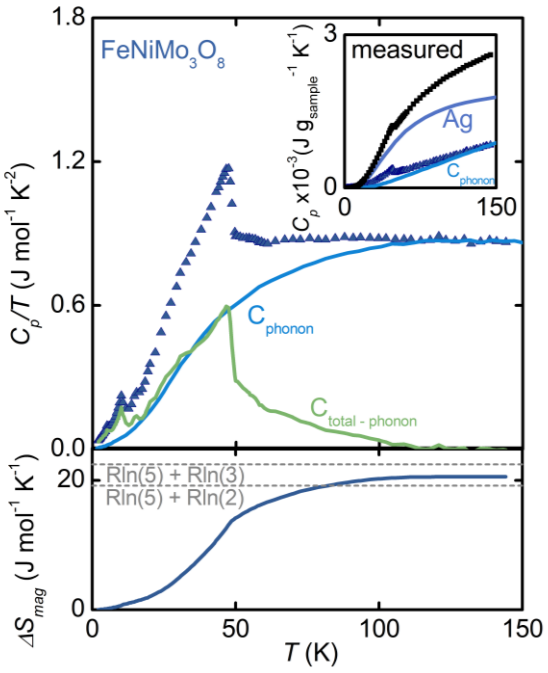

Figure 2.6 Top: Heat capacity over temperature versus temperature of $FeNiMo_3O_8$ measured from T = 2 to T = 150 K (dark blue squares). Inset: Raw measured data (black squares) included heat capacity from clean silver powder pressed with the sample (blue curve), which was subtracted to isolate only the contribution from $FeNiMo_3O_8$. A peak at T = 50 K capturing between Rln(5) + Rln(2) and Rln(5) + Rln(3) of entropy (bottom panel, dark blue curve) was determined to be magnetic (green curve, top panel) by subtracting the phonon contribution to the specific heat (light blue curve, top panel and inset, from measured non-magnetic analog $Zn_2Mo_3O_8$, scaled to be consistent with literature measurements on $Fe_2Mo_3O_8$ [44]).

All three compounds exhibit Curie-Weiss behavior at T > 100 K,

Figure 2.7(a). $MgNiMo_3O_8$ has a small positive Weiss temperature of θ_W = 6.5(1.3) K, consistent with weak ferromagnetic interactions, and a Curie constant of 1.280(7) and p_{eff} = 3.20(3) μ_B. $Ni_2Mo_3O_8$ has a larger negative Weiss temperature of θ_W = -55.5(5) K, consistent with antiferromagnetic interactions, a total Curie constant of 5.518(1.0), and an average p_{eff} of 4.70(3) μ_B per nickel atom, summarized in Table 2.3.

$FeNiMo_3O_8$ exhibits a clear antiferromagnetic phase transition at T ~ 50 K,

Figure 2.7(b). The effective magnetic moment is 6.86(4) μ_B, which is close to the expected spin-only moment of 7.32 μ_B of combined high-spin Fe^{2+} (4.49 μ_B) and Ni^{2+} (2.83 μ_B). The Weiss temperature is T = -101.5(3) K, indicating strong antiferromagnetic interactions.

At T = 2 and T = 6 K, the field dependent magnetization of $Ni_2Mo_3O_8$ has metamagnetic curvature which is not visible at T = 15 K,

Figure 2.7(a) inset. Such metamagnetism suggests that a low-lying (in field) magnetic phase transition is possible. This behavior could be interpreted as differences in in-plane and out-of-plane magnetic responses, for which single crystal samples are necessary to fully understand the nature of the transition [8]. There is no apparent hysteresis to the curve, suggesting that there is little to no ferromagnetic component of the magnetization at this temperature. The magnetic response of $MgNiMo_3O_8$ fits well to a Brillouin function in the T = 2 K to T = 300 K temperature range and is thus likely paramagnetic at all measured temperatures (Fig. 3 and Table 2, SI).

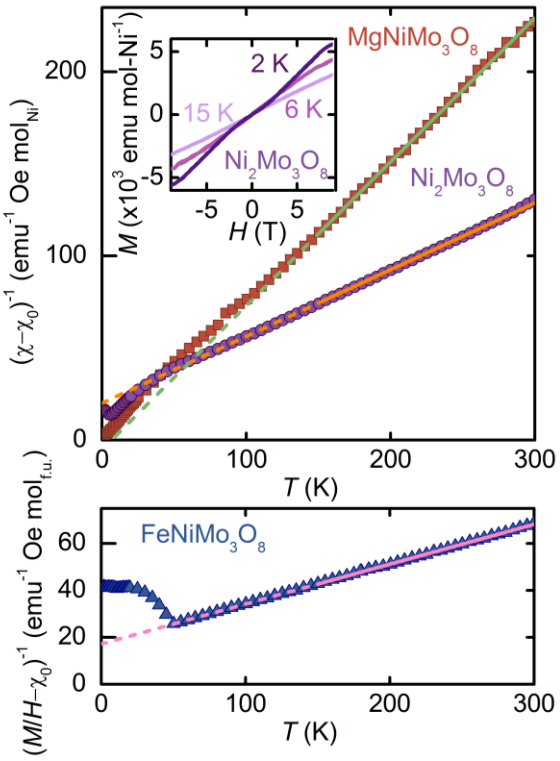

Figure 2.7 Inverse susceptibility of $Ni_2Mo_3O_8$, $MgNiMo_3O_8$, and $FeNiMo_3O_8$ linearized and fit to the Curie-Weiss law in the temperature range of 150 K to 300 K, fit values summarized in Table 2.3. (a) Inverse susceptibility of $MgNiMo_3O_8$ (brown squares) is non-linear below $T = 150$ K but shows no clear ordering transition. In contrast, a small upturn at $T = 6$ K in the inverse susceptibility of $Ni_2Mo_3O_8$ (purple squares) indicates an antiferromagnetic phase transition. The inverse susceptibility of this material is also non-linear in the $T = 6 – 150$ K temperature range. Inset: Magnetization versus applied field of $Ni_2Mo_3O_8$ at $T = 2$ K, 6 K, and 15 K. (b) A sharp uptick in the inverse susceptibility of $FeNiMo_3O_8$ indicates an antiferromagnetic phase transition at $T \sim 50$ K.

Table 2.3 Fit values for Curie-Weiss analysis of high temperature magnetic susceptibility of $Ni_2Mo_3O_8$, $MgNiMo_3O_8$ and $FeNiMo_3O_8$, shown graphically in

Figure 2.7. *C* and p_{eff} are per formula unit.

	$Ni_2Mo_3O_8$	$MgNiMo_3O_8$	$FeNiMo_3O_8$
C (emu K mol^{-1} K^{-1})	5.52(1.4)	1.28(7)	5.89(9)
p_{eff} (μ_B)	6.64(6)	3.20(3)	6.86(4)
θ_W (K)	-55.5(5)	6.5(1.3)	-101(1.0)
T_N (K)	6.0(2)	-	50.0(2)
χ_0 (emu mol^{-1} Oe^{-1})	0.0025	0.0015	0.00055

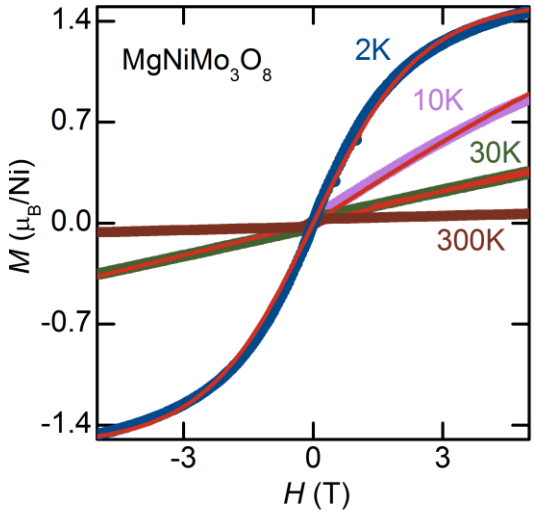

Figure 2.8 Field-dependent magnetization of $MgNiMo_3O_8$ measured at T = 2 K, 10 K, 30 K, and 300 K. Red curves represent fits of a Brillouin function to the data. Fit values are summarized in Table 2.4

Table 2.4 Refined values and fit statistics for fits of a Brillouin function to field-dependent magnetization of $MgNiMo_3O_8$ at T = 2 K, 10K, and 300 K.

T (K)	J	R^2
2	0.7751(9)	0.99874
10	1.051(18)	0.99504
30	1.157(2)	0.9942

The magnetization is defined as $M = g_j \times J \times B_j$

Where the Brillouin function B_J as a function of angular momentum J is:

$$B_j = \frac{2J+1}{2J} coth\left(\frac{2J+1}{2J} \times t\right) - \frac{1}{2J} coth\left(\frac{t}{2J}\right)$$

And the ratio of the magnetic and thermal energies is:

$$t = \frac{f \times g_j \times J}{kT} \times H$$

Where M is magnetization, H is applied field, and g_j is held to the spin-only value of 2.

2.3.3 Electron Spin Resonance

The ESR data in Figure 2.10 (a) and (b) from $Ni_2Mo_3O_8$ and $MgNiMo_3O_8$ have broad resonances, which is typical of S = 1 systems [47]. There are two magnetic sites in each unit cell: the octahedrally coordinated and tetrahedrally coordinated nickels on the two triangular honeycomb sublattices. In $Ni_2Mo_3O_8$, these sites are equally populated. In $MgNiMo_3O_8$, 14(3)% of the tetrahedral sites and 86(3)% of the octahedral sites are populated by Ni (determined from NPD), and the remaining sites are non-magnetic. Thus, the ESR data from $Ni_2Mo_3O_8$ should

show two equally-weighted resonances and the data from $MgNiMo_3O_8$ should show two resonances at 14% and 86% on each of the respective sites. This is visually consistent with the data, shown in Figure 2.9, $Ni_2Mo_3O_8$, and Figure 2.10, $MgNiMo_3O_8$. The resonance for $Ni_2Mo_3O_8$ looks like one broad resonance, which can be decomposed into two similarly-sized overlapping features. The resonance for $MgNiMo_3O_8$ is clearly two components. These features were fit using two Lorentzian curves, from which the g factor, integrated intensity, and width could be extracted. The temperature dependence of these parameters are plotted in Figure 2.9 (d-f) and Figure 2.10 (d-f).

We can leverage our knowledge of the stoichiometry and site occupancy in $MgNiMo_3O_8$ and the measured signals from $Ni_2Mo_3O_8$ and $MgNiMo_3O_8$ to separate the signals from the two sites. The higher intensity feature in $MgNiMo_3O_8$ corresponds to the 86% stoichiometric octahedral fraction, while the lower intensity peak corresponds to the 14% stoichiometric tetrahedral fraction. Subtracting the $Ni_2Mo_3O_8$ and $MgNiMo_3O_8$ signals with scaling factors for occupancy yield the single-contribution peaks (Figure 2.11). The resonance at lower (higher) field corresponds to the tetrahedral (octahedral) component: when the scaled fraction of $Ni_2Mo_3O_8$ is subtracted from the $MgNiMo_3O_8$, the higher field feature remains.

The g factor for the octahedral site is temperature insensitive in both $MgNiMo_3O_8$ and $Ni_2Mo_3O_8$ and remains at ~ 2.2 from T = 300 K to T = 10 K. In contrast, the g-factor for the tetrahedral site remains constant at ~ 3.7 from T = 290 K to T ~ 120 K and then increases from T ~ 130 K to ~ 4.3 as temperature decreases to T = 10 K.

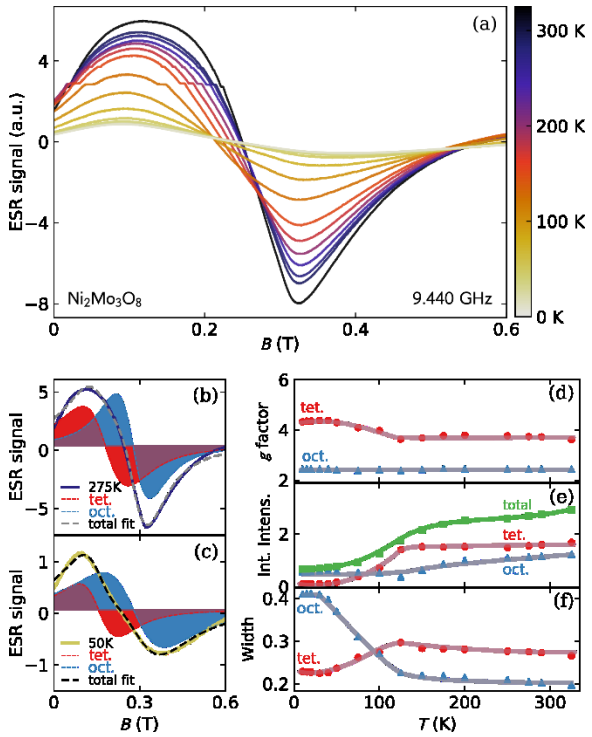

Figure 2.9 (a) Temperature dependent electron spin resonance (ESR) signal of $Ni_2Mo_3O_8$ in the T = 10 K to T = 325 K range. Two Lorenzian peak profiles were used to fit the data, shown for (b) T = 275 K and (c) T = 50 K, and the (d) g factor, (e) integrated intensity, and (f) width have a temperature dependence for the tetrahedral (red circles) and octahedral (blue triangles) coordination environments. Total integrated intensity is represented with green squares. Guides to the eye are drawn for panels d, e, and f.

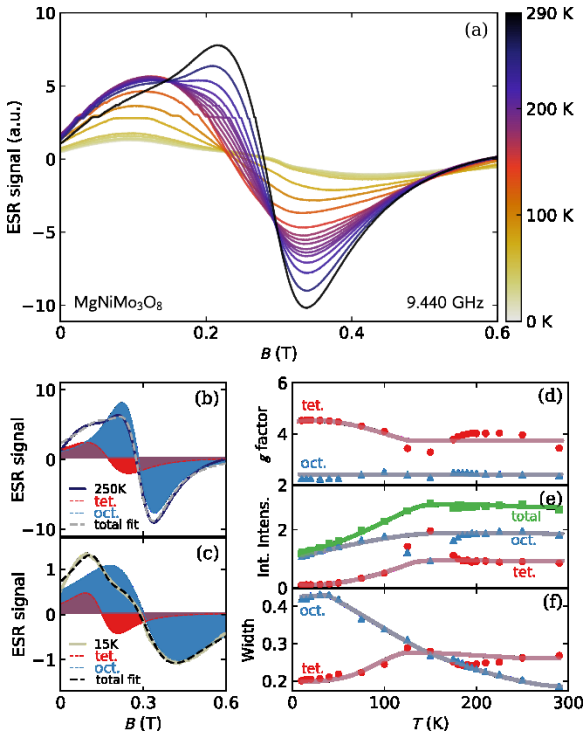

Figure 2.10 (a) Temperature dependent electron spin resonance (ESR) signal of $MgNiMo_3O_8$ in the $T = 10$ K to $T = 325$ K range. Two Lorenzian peak profiles were used to fit the data, shown for (b) $T = 275$ K and (c) $T = 50$ K, and the (d) g factor, (e) integrated intensity, and (f) width have a temperature dependence for the tetrahedral (red circles) and octahedral (blue triangles) coordination environments. Total integrated intensity is represented with green squares. Guides to the eye are drawn in panels d, e, and f.

Above $T = 150$ K, the octahedral data have two isosbestic points: one at 0.28 T and the other at 0.18 T. Below $T = 150$ K, there is one isosbestic point at 0.23 T. The integrated intensity for both $Ni_2Mo_3O_8$ and $MgNiMo_3O_8$ decreases from $T \sim 150$ K to $T = 10$ K.

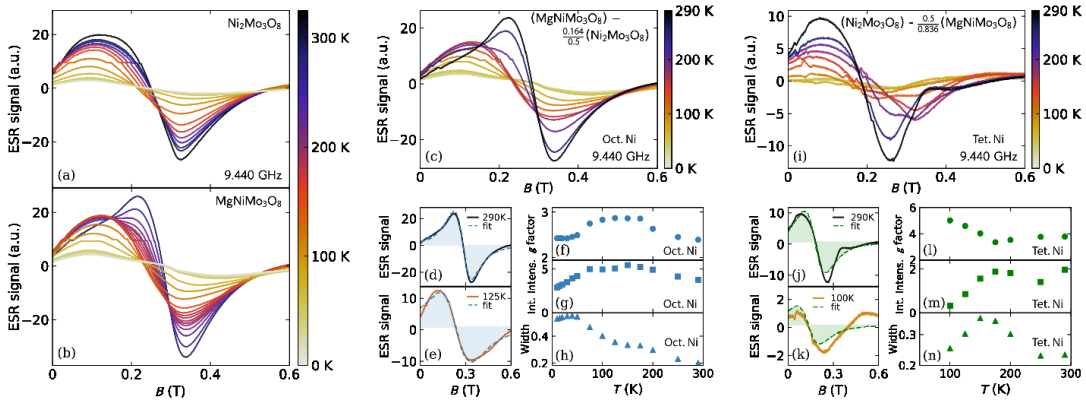

Figure 2.11 (a) Temperature dependent electron spin resonance signal of (a) $Ni_2Mo_3O_8$ in the $T = 10$ to $T = 325$ K range, and (b) $MgNiMo_3O_8$ in the $T = 10$ K to $T = 290$ K range measured at a frequency of 9.440 GHz. (c)(i) Plot of the octahedral (tetrahedral) component of the $MgNiMo_3O_8$ ($Ni_2Mo_3O_8$) data, and fits of a Lorentzian profile to data at (d)(j) 290 K and (e)(k) 125 K (100 K). Plots of (f)(l) g-factor, (g)(m) integrated intensity, and (h)(n) width parameters of fits at all measured temperatures.

2.3.4 Single Ion Crystal Field Analysis

Using the low temperature crystal structure, a point charge model can be used to construct the expected splitting of multielectron states for Ni^{2+} on the octahedral and tetrahedral sites, Figure 2.12. As expected, the trigonal distortion removes the orbital degeneracy for the tetrahedral case, but leaves the (orbitally non-degenerate) ground state of the octahedral site intact. The confluence of the trigonal crystal field with spin orbit coupling lifts the degeneracy of the ground state triplet resulting in single ion anisotropies of $\Delta = 22$ meV and $\Delta = 7.8$ meV for tetrahedral and octahedral respectively. Crucially, the low lying states on the two distinct sites are symmetry compatible and thus can have significant

exchange/superexchange interactions, in agreement with the large and negative Weiss temperature observed for $Ni_2Mo_3O_8$. Further, the single ion anisotropy of the tetrahedral site is consistent with the temperature dependent changes observed in ESR: the g-factor is expected to start to change from its high temperature to low temperature value around $0.42*\Delta = 107$ K, versus the observed $T = 110$ K. In contrast, the octahedral site would not have a local change in anisotropy until ~30 K, a temperature at which interactions between sites are already dominant.

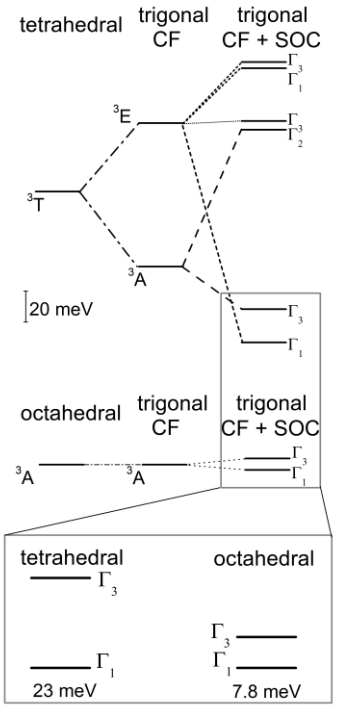

Figure 2.12 Diagram of the single ion energy levels of the (left) undistorted tetrahedral and octahedral coordination environments, (middle) trigonal distortion, and (right) trigonal distortion and spin orbit coupling (SOC). Bottom: the two lowest energy states of tetrahedral and octahedral crystal field environments are similar in energy splitting and have the same Γ_1 and Γ_3 symmetries.

2.3.5 Magnetic Structure Determination

Magnetic Bragg peaks were identified in NPD patterns of $Ni_2Mo_3O_8$ at T = 1.6 K that were not present at T = 15 K, which is consistent with the magnetic phase transition observed in susceptibility data. These peaks were isolated by

subtraction of nuclear peaks measured at the two temperatures and can be seen in

Figure 2.13. The largest propagation vector, $\vec{k}$, the smallest vector in real space that indexes all of the magnetic peaks is $\vec{k}$ = (½ 0 0). This indicates that a doubling of the unit cell in the *a* direction is necessary to describe the magnetic order. It should be noted that space group $P6_3mc$ is non-orthogonal, and this doubling is in internal *abc* directions, rather than orthogonal *xyz* directions. Representational analysis of this $\vec{k}$ vector in space group $P6_3mc$ leads to four irreducible representations: Γ_1, Γ_2, Γ_3, and Γ_4 on six basis vectors ψ_1-ψ_6, which are summarized in Table 2.5. Consistent with Landau theory, only a single irreducible representation is necessary to describe the structure resulting from a second order phase transition.

Table 2.5. Irreducible representations (IR) and basis vectors (BV) for the two magnetic nickel atoms in $Ni_2Mo_3O_8$ and associated real components in the *a*, *b*, and *c* directions for $\vec{k}$ = (½ 0 0) in space group $P6_3mc$.

IR	BV	atom	$m_{\parallel a}$	$m_{\parallel b}$	$m_{\parallel c}$
Γ_1	ψ_1	Ni1	0	-1	0
		Ni2	0	-1	0
Γ_2	ψ_2	Ni1	2	1	0
		Ni2	2	1	0
	ψ_3	Ni1	0	0	2
		Ni2	0	0	-2
Γ_3	ψ_4	Ni1	0	-1	0
		Ni2	0	1	0
Γ_4	ψ_5	Ni1	2	1	0
		Ni2	-2	-1	0
	ψ_6	Ni1	0	0	2
		Ni2	0	0	2

The intensity of neutrons scattering off of long range magnetic corresponds to the magnetic moment perpendicular to the neutron scattering vector. The tallest magnetic peak at $2\theta = 24.10^o$ corresponds to the (004) reflection. The significant amount of intensity in this and related reflections means that there must be intensity in the *c* direction. There is no coefficient giving rise to intensity in the *c* direction in the Γ_1 and Γ_3 irreducible representations, so these may be discarded. Both Γ_2 and Γ_4 allow for intensity at all indexed peaks; between the two, refinements of Γ_2 show a better fit to the data, with a statistical χ^2 of 4.479, where the best fit of Γ_4 gives a χ^2 of 5.502. A comparison of the statistical refinements can be seen in Table 2.6.

Table 2.6 Refinement statistics for fits using the irreducible representations Γ_2 and Γ_4 on the magnetic peaks in neutron powder diffraction patterns of Ni2Mo3O8. Initialization of refinements with more magnitude in the c direction or the ab plane resulted in subtly different solutions.

	Γ_2		Γ_4	
	c direction	*ab* plane	*c* dir.	*ab* plane
χ^2	4.479	4.479	5.546	5.502

With no constraints on magnitude and direction of magnetic moment, the refined magnetic structure in Γ_2 is a zig-zag structure. Three other common ordering patterns for honeycomb lattices were also explicitly tested: ferromagnetic (FM), Néel AFM, stripy AFM. In these refinements, the sign of the moment (+/-) in *c* relative to the honeycomb lattice was constrained, but the magnitude and direction of the magnetic moment were not. The results of these refinements are shown in Figure 2. (a-d), and the structure visualized in Figure 2.13 (e, f). It is clear that (a) FM, (b) stripe AFM, and (c) Néel AFM do not fit the data as well as the zig-zag AFM structure (d-f)

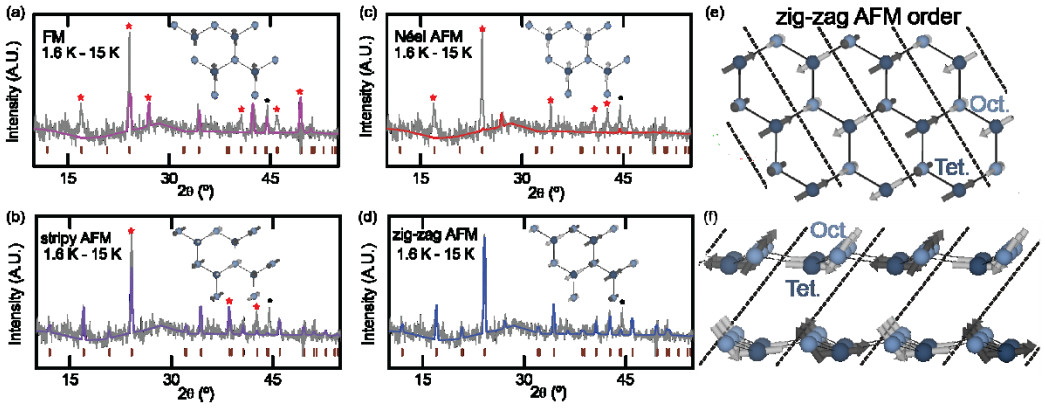

Figure 2.13 Refined models with enforced (a) ferromagnetic (FM), (b) stripy antiferromagnetic (AFM), (c), Néel AFM, and (d) zig-zag AFM order on neutron powder diffraction patterns collected at T = 1.6 K with the nuclear contribution subtracted using measurements done at T = 15 K. (a) FM and (c) Néel AFM order do not have intensity at many magnetic peaks; zig-zag AFM order results in the best fit. Red asterisks denote significant deviations of the fit from the data. The black asterisk denotes a remnant structural contribution. (e) Top-down and (f) side view of the zig-zag structure. Magnetic moment in the +c (-c) direction are light (dark) gray, dark (light) blue atoms are tetrahedrally (octahedrally) coordinated nickel.

All combinations of larger moment on the tetrahedral site or the octahedral site, initiated with magnitude in the c direction or the ab plane, and every combination of positive and negative starting values for the coefficients of the basis vectors were refined using the nuclear-subtracted magnetic Bragg peaks with no constraints on magnitude and direction, Table 2.7and Table 2.8. All refinements resulted in zig-zag AFM order. While there is no statistical difference between the χ^2 metric of the quality of the refinements that have more magnitude on the octahedral or tetrahedral nickel site (the sites are indistinguishable if only

the Ni atom positions are considered), it is clear from ESR data that there is a larger magnetic moment on the tetrahedral nickel.

There are two statistically identical zig-zag AFM ordered magnetic structures with larger magnetic moment on the tetrahedral nickel. There is strong directionality to the magnetic moment of the two sites of both. In one, an ordered moment of 1.727 μ_B on the tetrahedral site lies mainly in the *ab* plane and a moment of 1.431 μ_B on the octahedral site points primarily in the *c* direction. In the other, an ordered moment of 1.997 $\mu_B$on the tetrahedral site points partially in the *c* direction and a moment of 0.891 μ_B on the octahedral site is mainly in the *ab* plane. These have been visualized in Figure 2.14.

Table 2.7 Γ_2 refinements of c_2, the coefficient of basis vector ψ_2, and c_3, the coefficient of basis vector ψ_3, initialized with greater intensity in the *c* direction on either the tehtrahedrally or octahedrally coordinated nickel. Magnitude and direction of the spins were not constrained. All refinements resulted in zig-zag order.

Γ_2	Initial		Final		μ_B	χ^2	Initial		Final		μ_B	χ^2
	c_2	c_3	c_2	c_3			c_2	c_3	c_2	c_3		
Ni_{Td}	-2	-5	-0.463	-0.586	1.423	4.48	-2	-2	-0.463	-0.586	1.423	4.48
Ni_{Oh}	-2	-2	0.994	0.070	1.727		-2	-5	0.994	0.070	1.727	
Ni_{Td}	-2	-5	-0.463	-0.586	1.421	4.48	-2	-2	-0.994	0.072	1.727	4.48
Ni_{Oh}	-2	2	0.994	0.070	1.727		-2	5	0.467	-0.586	1.424	
Ni_{Td}	-2	-5	-0.463	-0.586	1.421	4.48	-2	-2	-0.994	0.072	1.727	4.48
Ni_{Oh}	2	-2	0.994	0.070	1.727		2	-5	0.467	-0.586	1.391	
Ni_{Td}	-2	-5	-0.463	-0.586	1.421	4.48	-2	-2	0.994	-0.072	1.727	4.48
Ni_{Oh}	2	2	0.994	0.070	1.727		2	5	-0.467	0.586	1.430	
Ni_{Td}	-2	5	0.467	0.590	1.430	4.48	-2	2	-0.994	0.072	1.727	4.48
Ni_{Oh}	-2	-2	-0.994	-0.069	1.727		-2	-5	0.467	-0.586	1.424	
Ni_{Td}	-2	5	0.467	0.590	1.430	4.48	-2	2	0.994	-0.072	1.727	4.48
Ni_{Oh}	-2	2	-0.994	-0.069	1.727		-2	5	-0.467	0.586	1.430	
Ni_{Td}	-2	5	0.467	0.590	1.430	4.48	-2	2	-0.994	0.072	1.727	4.48
Ni_{Oh}	2	-2	-0.994	-0.069	1.727		2	-5	0.467	-0.586	1.424	
Ni_{Td}	-2	5	0.467	0.590	1.430	4.48	-2	2	0.994	-0.069	1.727	4.48
Ni_{Oh}	2	2	-0.994	-0.069	1.727		2	5	-0.467	0.586	1.430	
Ni_{Td}	2	-5	-0.463	-0.586	1.430	4.48	2	-2	-0.994	0.072	1.727	4.48
Ni_{Oh}	-2	-2	0.994	0.070	1.727		-2	-5	0.467	-0.586	1.424	
Ni_{Td}	2	-5	-0.463	-0.586	1.421	4.48	2	-2	0.994	-0.069	1.727	4.48
Ni_{Oh}	-2	2	0.994	0.070	1.727		-2	5	-0.467	0.590	1.421	
Ni_{Td}	2	-5	-0.463	-0.586	1.430	4.48	2	-2	-0.994	0.072	1.727	4.48
Ni_{Oh}	2	-2	0.994	0.070	1.727		2	-5	0.467	-0.586	1.424	
Ni_{Td}	2	-5	-0.463	-0.586	1.430	4.48	2	-2	0.994	-0.072	1.727	4.48
Ni_{Oh}	2	2	0.994	0.070	1.727		2	5	-0.467	0.590	1.430	
Ni_{Td}	2	5	0.467	0.590	1.430	4.48	2	2	0.994	-0.069	1.727	4.48
Ni_{Oh}	-2	-2	-0.994	-0.069	1.393		-2	-5	-0.467	0.590	1.424	
Ni_{Td}	2	5	0.467	0.590	1.430	4.48	2	2	0.994	-0.069	1.727	4.48
Ni_{Oh}	-2	2	-0.994	-0.069	1.727		-2	5	-0.467	0.590	1.430	
Ni_{Td}	2	5	0.467	0.590	1.430	4.48	2	2	0.994	-0.069	1.727	4.48
Ni_{Oh}	2	-2	-0.994	-0.069	1.727		2	-5	-0.467	0.590	1.424	
Ni_{Td}	2	5	0.467	0.590	1.430	4.48	2	2	0.994	-0.069	1.727	4.48
Ni_{Oh}	2	2	-0.994	-0.069	1.727		2	5	-0.467	0.590	1.430	

Table 2.8 Γ_2 refinements of c_2, the coefficient of basis vector ψ_2,and c_3, the coefficient of basis vector ψ_3, initialized with greater intensity in the *ab* plane on either the tehtrahedrally or octahedrally coordinated nickel. Magnitude and direction of the spins were not constrained. All refinements resulted in zig-zag order.

Γ_2	Initial		Final		μ_B	χ^2	Initial		Final		μ_B	χ^2
	c_2	c_3	c_2	c_3			c_2	c_3	c_2	c_3		
Ni_{Td}	-5	-2	-0.956	-0.559	1.998	4.47	-2	-2	0.430	0.012	0.747	4.60
Ni_{Oh}	-2	-2	0.508	0.021	0.881		-2	-2	-1.000	-0.488	1.988	
Ni_{Td}	-5	-2	-0.956	-0.559	1.998	4.49	-2	-2	0.509	-0.021	0.882	4.49
Ni_{Oh}	-2	2	0.509	0.023	0.883		-5	2	-0.956	0.559	1.997	
Ni_{Td}	-5	-2	-0.955	-0.559	1.997	4.49	-2	-2	-0.508	0.021	0.881	4.49
Ni_{Oh}	2	-2	0.513	0.021	0.896		5	-2	0.959	-0.559	2.000	
Ni_{Td}	-5	-2	-0.955	-0.559	1.997	4.49	-2	-2	-0.467	-0.586	0.747	4.48
Ni_{Oh}	2	2	0.509	0.022	0.884		5	2	0.997	0.070	1.988	
Ni_{Td}	-5	2	-0.994	0.080	1.727	4.49	-2	2	0.467	0.586	1.424	4.57
Ni_{Oh}	-2	-2	0.467	-0.586	0.000		-5	-2	-0.994	-0.069	1.727	
Ni_{Td}	-5	2	-0.999	-0.489	1.987	4.60	-2	2	0.509	-0.020	0.747	4.49
Ni_{Oh}	-2	2	0.431	-0.010	0.747		-5	2	-0.956	0.559	1.988	
Ni_{Td}	-5	2	-0.994	0.072	1.727	4.48	-2	2	0.508	0.022	0.881	4.49
Ni_{Oh}	2	-2	0.468	-0.586	1.425		5	-2	0.959	-0.559	2.003	
Ni_{Td}	-5	2	-0.999	0.489	1.988	4.60	-2	2	0.432	-0.009	0.748	4.60
Ni_{Oh}	2	2	0.432	-0.009	0.748		5	2	1.000	0.489	1.989	
Ni_{Td}	2	-5	1.003	-0.488	1.990	4.60	2	-2	0.435	0.012	0.754	4.49
Ni_{Oh}	-2	-2	-0.431	0.012	0.747		-2	-5	-1.000	-0.488	1.988	
Ni_{Td}	5	-2	1.003	-0.488	1.993	4.48	2	-2	0.514	-0.021	0.759	4.48
Ni_{Oh}	-2	2	-0.431	0.012	0.747		-5	2	-0.955	0.559	1.997	
Ni_{Td}	5	-2	1.002	-0.488	1.987	4.60	2	-2	-0.501	0.020	0.747	4.49
Ni_{Oh}	2	-2	-0.428	0.012	0.747		5	-2	0.964	-0.559	1.988	
Ni_{Td}	5	-2	0.998	-0.069	1.735	4.48	2	-2	-0.465	-0.586	1.422	4.48
Ni_{Oh}	2	2	-0.462	0.586	1.420		5	2	0.996	0.070	1.731	
Ni_{Td}	5	2	0.963	0.559	2.008	4.49	2	2	0.470	0.588	1.431	4.48
Ni_{Oh}	-2	-2	-0.508	-0.021	0.881		-5	-2	-0.994	-0.069	1.727	
Ni_{Td}	5	2	0.960	0.559	2.003	4.49	2	2	0.500	-0.020	0.882	4.48
Ni_{Oh}	-2	2	-0.508	-0.019	0.881		-5	2	-0.956	0.559	1.998	
Ni_{Td}	5	2	0.964	0.559	2.009	4.49	2	2	0.500	0.021	0.867	4.49
Ni_{Oh}	2	-2	-0.500	0.559	0.867		5	-2	0.964	-0.559	2.009	
Ni_{Td}	5	2	0.964	0.559	2.009	4.49	2	2	-0.430	-0.011	0.746	4.60
Ni_{Oh}	2	2	-0.500	-0.019	0.867		5	2	1.000	0.488	1.988	

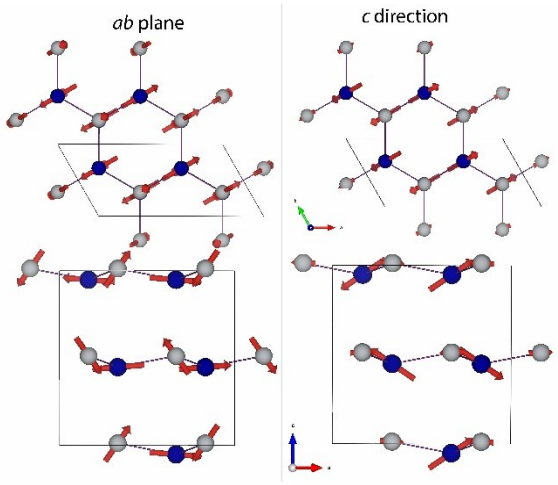

Figure 2.14 Visualization of magnetic structures shown in Figure 2.15. Left: tetrahedral magnetic moment is in the ab plane, right: tetrahedral magnetic moment in the c direction.

The ratio of the tetrahedral to octahedral g factors (which are proportional to the magnetic moment) is 1.21 for structure where the tetrahedral moment is primarily in the *ab* plane and 2.24 for the moment in the *c* direction. These numbers bracket the ratio of 1.8 observed in the ESR measurements at $T = 10$ K, Table 2.9. The refinement to the structure where the tetrahedral spins lie mainly in the *ab* plane better describes the data, based on visual inspection (Figure 2.15). This solution is more intuitive, too, as one would expect the magnetic moment to be roughly the same for the two sites, as nickel is 2+ on both.

Table 2.9. Values and ratios of tetrahedral to octahedral magnetic moments from ESR measured at T = 10 K and refinements in Γ_2 to the magnetic Bragg peaks from NPD with the tetrahedral spins primarily in the *ab* plane or the *c* direction.

	$\mu_{B,Tet.}$	$\mu_{B,Oct.}$	$\frac{\mu_{B,Tet.}}{\mu_{B,Oct.}}$
ESR T = 10 K	4.32	2.43	1.78
ab plane	1.727	1.431	1.21
c direction	1.997	0.891	2.24

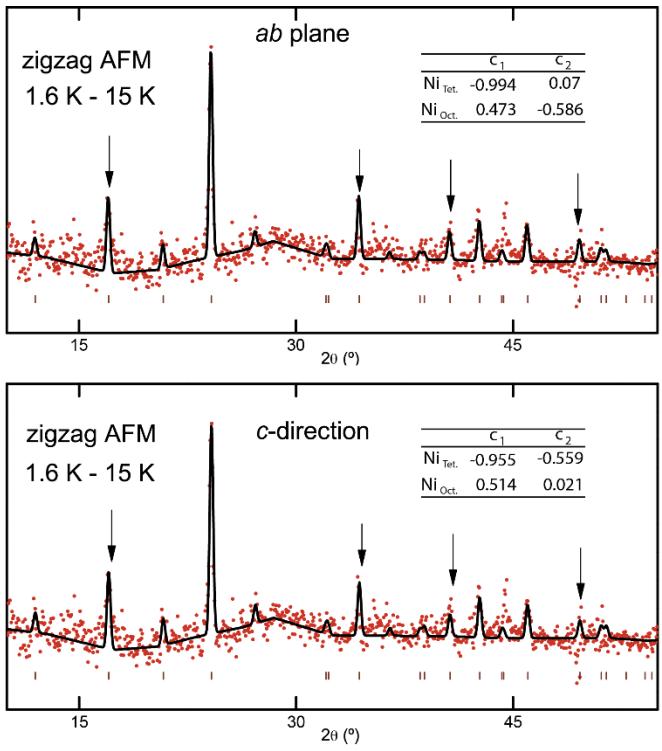

Figure 2.15 Refinements to the magnetic contribution to NPD patterns. Top: tetrahedral magnetic moments in the *ab* plane. Bottom: tetrahedral magnetic moment in the *c* direction. Inset tables show the refined coefficients for the basis vectors for each refinement. Arrows identify peaks with significant differences between the two refinements. Visualizations of these structures can be seen in Figure 2.14. The coefficient c_1 operates on a basis vector in the *ab* plane, c_2 on a basis vector in the *c* direction.

Section 2.4 Discussion

The ratio of the tetrahedral site g-factor to the octahedral site g-factor determined by ESR at T = 290 K is 1.46, which is very close to 1.52, the ratio of the effective magnetic moments per Ni of $Ni_2Mo_3O_8$ to $MgNiMo_3O_8$ found by Curie-Weiss analysis of temperature-dependent magnetization. This further validates the agreement of the magnetic measurements and the conclusion that $MgNiMo_3O_8$ is an analog for the magnetic behavior for isolated nickels interacting on the octahedrally coordinated sublattice of the honeycomb. This ratio is also close to the ratio of the ordered magnetic moments on the tetrahedral and octahedral sites determined by NPD.

The data supports the interpretation that there is anisotropy to the magnetism on the tetrahedral site in $Ni_2Mo_3O_8$. (1) The zig-zag ordered structure shows a strong directional dependence of the magnetic moment on the two sites where the tetrahedral site has a strong *ab* plane component, (2) the observed metamagnetism in the field-dependent magnetization (inset, Figure 2.7 (a)) is a signature of anisotropy in powder samples, and has been observed in other honeycombs such as α-$RuCl_3$ [8], and (3) the entropy recovered in heat capacity measurements is consistent with Ni on the tetrahedral site recovering Rln(2) in $Ni_2Mo_3O_8$.

The expected recovered entropy for a triangular lattice of $S = 1$ ions with three spin degrees of freedom is Rln(3) and for a honeycomb lattice (comprised of two triangular sublattices) is 2Rln(3). As summarized in Table Table 2.2, $Ni_2Mo_3O_8$ recovers ~Rln(2) + Rln(3) and $MgNiMo_3O_8$ recovers 6.9(3) J mol^{-1} K^{-1} = 0.764Rln(3) of entropy. The site disorder determined by NPD places 86% of Ni on the octahedral site in $MgNiMo_3O_8$. The theoretical change in entropy if the octahedral site were to recover Rln(2) and the tetrahedral site were to recover Rln(3) is 6.1 J mol^{-1} K^{-1}. As this is smaller than the recovered value, it is clear that the octahedral site must be recovering Rln(3). The value of 0.76Rln(3) suggests, but does not conclusively prove, that the tetrahedral site does not recover significant entropy in $MgNiMo_3O_8$. That the entropy in $Ni_2Mo_3O_8$ recovers Rln(3)+Rln(2) strongly suggests that the tetrahedral site recovers Rln(2) of entropy, and thus has one fewer degree of freedom than the octahedral site. This implies spin anisotropy, perhaps easy-plane, which is consistent with the magnetic structure.

There are three known possible magnetic Hamiltonians which could stabilize zig-zag AFM order in $Ni_2Mo_3O_8$: (1) bond-dependent Heisenberg-Kitaev interactions [48, 49], (2) isotropic interactions where nearest neighbor (2N), next-nearest neighbor (3N), and next-next-nearest neighbor (4N) in-plane interactions

are all of similar strength [12, 13], and (3) bond-dependent anisotropic interactions through ligand distortion [35].

(1) The Kitaev model requires that exchange anisotropy must be orthogonal to the Ni-Ni bond and that there are 90° interfering ligand superexchange pathways for Ising-like terms to emerge [50]. In $Ni_2Mo_3O_8$, the Ni-O-Ni bond lies along a mirror plane which precludes the necessary orthogonality. In addition, the alternating octahedral and tetrahedral coordination environments geometrically obstruct the ligand superexchange pathway.

(2) Isotropic interactions can stabilize zig-zag order when the 2N, 3N, and 4N in-plane interactions are all of similar strength. In $Ni_2Mo_3O_8$, 2N interactions are Oct.-Tet. (3.39 Å; oxygen mediated), 3N interactions are self-sublattice Oct.-Oct. and Tet.-Tet. (5.96 Å; oxygen and molybdenum mediated), and 4N are Oct. - Tet. (6.680(5) Å). $MgNiMo_3O_8$ can be viewed as a magnetically dilute analog of $Ni_2Mo_3O_8$ where the interacting magnetic atoms are predominantly structurally equivalent to the 3N interaction sublattice in $Ni_2Mo_3O_8$. While not a perfect analog, the type and relative scale of the magnetic interactions in $MgNiMo_3O_8$ is suggestive of the characteristics of the $Ni_2Mo_3O_8$ 3N interactions in the absence of the 2N interactions. The result of this magnetic dilution is a dramatic loss of

interaction strength: the Weiss temperature of $MgNiMo_3O_8$ is small and positive, 6 K, indicating that the interactions are small and ferromagnetic. For comparison, the Weiss temperature of $Ni_2Mo_3O_8$ is -55 K. Thus it is likely that nearest neighbor interactions are making up the bulk of the antiferromagnetic interactions in $Ni_2Mo_3O_8$ and isotropic interactions are likely not stabilizing the zig-zag order.

(3) There are slight distortions of the octahedral and tetrahedral coordination environments from the ideal single-ion crystal field to the symmetry-adapted, spin-orbit-coupled regime. Both Ni^{2+} ions are on sites with $3m$ (C_{3v}) symmetry, which is significantly lower point symmetry than either the O_h or T_d point groups in the single ion regime. As described in Figure 2.12, the lowest energy state in an undistorted octahedral complex is ^3A, which decomposes into a singlet Γ_1 and doublet Γ_3 under small trigonal distortions and application of spin orbit coupling in $3m$ symmetry. The next lowest energy state is 490 meV higher. In the tetrahedral coordination, the ground state is a spin and orbital triplet, ^3T, which decomposes into a singlet Γ_1 and doublet Γ_3 under small trigonal distortions and application of spin orbit coupling in $3m$ symmetry. It is possible that the bond-dependent interactions that occur as a result of Γ_1-Γ_1 and Γ_3-Γ_3 mixing in adjacent octahedral and tetrahedral coordination environments stabilize zig-zag order in $Ni_2Mo_3O_8$.

Bond-dependent interactions are consistent with the data collected. In particular, the rich temperature-dependent behavior in the ESR data suggest the presence of single ion anisotropy that changes with temperature: the g factor increases between T = 130 K and T = 10 K, and below T ~ 150 K the amplitude of the signal decreases. This is attributable to a change in the timescale of paramagnetic fluctuations to frequencies below those that ESR samples as the magnetic state heads toward long range order. Additionally, the ratio of the a and c lattice parameters shows anisotropic changes concomitant with the temperature dependence of the ESR data.

Section 2.6 Conclusions

$Ni_2Mo_3O_8$ is the first realized example of an integer spin zig-zag AFM ordered honeycomb in a non-centrosymmetric space group ($P6_3mc$). Theoretical studies have predicted the existence of topological magnons in honeycomb compounds with zig-zag AFM order, and $Ni_2Mo_3O_8$ may provide an opportunity to investigate this and other topological phenomena experimentally. The zig-zag AFM order on $Ni_2Mo_3O_8$ may be stabilized by bond-dependent anisotropic exchange due to ligand distortion; the unique structure of alternating octahedral and tetrahedral Ni^{2+} on the honeycomb offers fundamentally different chemistry from other nickel honeycomb compounds in existence. We have also shown that

the magnetic exchanges in this material are tuneable by selective chemical substitution on the honeycomb, from weakly ferromagnetic ($MgNiMo_3O_8$) to strongly antiferromagnetic ($FeNiMo_3O_8$). Further studies on these materials will advance the search for realized non-trivial quantum states of matter.

References

[1] M. Z. Hasan and C. L. Kane, Rev. Mod. Phys. 82, 3045 (2010).

[2] Y. Ando and L. Fu, Annu. Rev. Condens. Matter Phys. 6, 1 (2015).

[3] Y. Zhou, K. Kanoda, and T-K. Ng, Rev. Mod. Phys. 89, 025003 (2017).

[4] L. Savary and L. Balents, Rep. Prog. Phys. 80, 016502 (2016).

[5] B. K. Clark, D. A. Abanin, and S. L. Sondhi, Phys. Rev. Lett. 107, 087204 (2011).

[6] A. Kitaev, Ann. Phys. 321, 2 (2006).

[7] K. W. Plumb, J. P. Clancy, L. J. Sandilands, V. Vijay Shankar, Y. F. Hu, K. S. Burch, Hae-Young Kee, and Young-June Kim Phys. Rev. B 90, 041112(R) (2014).

[8] J. A. Sears, M. Songvilay, K. W. Plumb, J. P. Clancy, Y. Qiu, Y. Zhao, D. Parshall, and Young-June Kim Phys. Rev. B 91, 144420 (2015).

[9] H.-S. Kim, Vijay Shankar V., A. Catuneanu, and H.-Y. Kee Phys. Rev. B 91, 241110(R) (2015).

[10] C. A. Bridges, J.-Q. Yan, A. A. Aczel, L. Li, M. B. Stone, G. E. Granroth, M. D. Lumsden, Y. Yiu, J. Knolle, S. Bhattacharjee, D. L. Kovrizhin, R. Moessner, D. A. Tennant, D. G. Mandrus and S. E. Nagler, Nat. Mater. 15 (2016).

[11] A. Banerjee, C. A. Bridges, J.-Q. Yan, A. A. Aczel, L. Li, M. B. Stone, G. E. Granroth, M. D. Lumsden, Y. Yiu, J. Knolle, S. Bhattacharjee, D. L. Kovrizhin, R. Moessner, D. A. Tennant, D. G. Mandrus and S. E. Nagler, Nat. Mater. 15 (2016).

[12] P. H. Y. Li, R. F. Bishop, D. J. J. Farnell, and C. E. Campbell, Phys. Rev. B 86, 144404 (2012).

[13] A. F. Albuquerque, D. Schwandt, B. Hetényi, S. Capponi, M. Mambrini, and A. M. Läuchli, Phys. Rev. B 84, 024406 (2011).

[14] Y-Z You, I. Kimchi, and A. Vishwanath, Phys. Rev. B 86, 085145 (2012).

[15] J. Reuther, R. Thomale, and S. Rachel, Phys. Rev. B 90, 100405(R) (2014).

[16] A. Biffin, R. D. Johnson, I. Kimchi, R. Morris, A. Bombardi, J. G. Analytis, A. Vishwanath, and R. Coldea, Phys. Rev. Lett. 113, 197201 (2014).

[17] T. Takayama, A. Kato, R. Dinnebier, J. Nuss, H. Kono, L. S. I. Veiga, G. Fabbris, D. Haskel, and H. Takagi, Phys. Rev. Lett. 114, 077202 (2015).

[18] S. C. Williams, R. D. Johnson, F. Freund, S. Choi, A. Jesche, I. Kimchi, S. Manni, A. Bombardi, P. Manuel, P. Gegenwart, and R. Coldea. Phys. Rev. B 93, 195158 (2016).

[19] H-C. Jiang, Z-C. Gu, X-L. Qi, and S. Trebst, Phys. Rev. B 83, 245104 (2011).

[20] Y. Singh, S. Manni, J. Reuther, T. Berlijn, R. Thomale, W. Ku, S. Trebst, and P. Gegenwart, Phys. Rev. Lett. 108, 127203 (2012).

[21] F. Ye, S. Chi, H. Cao, B. C. Chakoumakos, J. A. Fernandez-Baca, R. Custelcean, T. F. Qi, O. B. Korneta, and G. Cao, Phys. Rev. B 85, 180403(R) (2012).

[22] J. Chaloupka, G. Jackeli, and G. Khaliullin, Phys. Rev. Lett. 110, 097204 (2013).

[23] V. M Katukuri, S. Nishimoto, V. Yushankhai, A. Stoyanova, H. Kandpal, S. Choi, R. Coldea, I. Rousochatzakis, L. Hozoi and J. van den Brink, New J. Phys. 16 (2014).

[24] K. A. Modic, T. E. Smidt, I. Kimchi, N. P. Breznay, A. Biffin, S. Choi, R. D. Johnson, R. Coldea, P. Watkins-Curry, G. T. McCandless, J. Y. Chan, F. Gandara, Z. Islam, A. Vishwanath, A. Shekhter, R. D. McDonald and J. G. Analytis, Nat. Comm. 5 (2014).

[25] J. Chaloupka and G. Khaliullin, Phys. Rev. B 94, 064435 (2016).

[26] A. F. Albuquerque, D. Schwandt, B. Hetényi, S. Capponi, M. Mambrini, and A. M. Läuchli, Phys. Rev. B 84, 024406 (2011).

[27] F. Mezzacapo and M. Boninsegni, Phys. Rev. B 85, 060402(R) (2012).

[28] J. G. Rau, E. K.-H. Lee, and H.-Y. Kee, Phys. Rev. Lett. 112, 077204 (2014).

[29] Z. Nussinov and J. van den Brink Rev. Mod. Phys. 87, 1 (2015).

[30] E. A. Zvereva, M. I. Stratan, A. V. Ushakov, V. B. Nalbandyan, I. L. Shukaev, A. V. Silhanek, M. Abdel-Hafiez, S. V. Streltsovbh and A. N. Vasilievahi, Dalton Trans. 45, 17 (2016).

[31] H. Liu and G. Khaliullin, Phys. Rev. B 97, 014407 (2018).

[32] S. A. Owerre, J. Phys. Condens. Matter. 28, 38 (2016).

[33] H. Lee, S. B. Chung, K. Park, J.-G. Park , arXiv:1712.09801 (2017).

[34] S.P. McAlister and P. Strobel, J. Magn. Magn. Mater. 20, 3 (1983).

[35] E. A. Zvereva, M. I. Stratan, Y. A. Ovchenkov, V. B. Nalbandyan, J.-Y. Lin, E. L. Vavilova, M. F. Iakovleva, M. Abdel-Hafiez, A. V. Silhanek, X.-J. Chen, A. Stroppa, S. Picozzi, H. O. Jeschke, R. Valenti, and A. N. Vasiliev, Phs. Rev. B 92, 144401 (2015).

[36] E. M. Seibel, J. H. Roudebush, H. Wu, Q. Huang, M. N. Ali, H. Ji and R. J. Cava, Inorg. Chem. 52, 23 (2013).

[37] R. Berthelot, W. Schmidt, S. Muir, J. Eilertsen, L. Etienne, A. W. Sleight and M. A. Subramanian, Inorg. Chem. 51, 9 (2012).

[38] A.C. Larson and R.B. Von Dreele, Los Alamos National Laboratory Report LAUR 86-748 (2000).

[39] B.H. Toby, J. Appl. Cryst. 34, 210 (2001).

[40] Rodrigues-Carvajal, Phys. B 192, 55 (1993).

[41] Wills, A. S. Physica B, 276 (2000).

[42] K. Momma and F. Izumi, J. Appl. Crystallogr. 44 (2011).

[43] A. Tari, *The Specific Heat of Matter at Low Temperatures* (Imperial College Press, London, 2003).

[44] T. Kurumaji, Y. Takahashi, J. Fujioka, R. Masuda, H. Shishikura, S. Ishiwata, and Y. Tokura, Phys. Rev. B 95, 020405(R) (2017).

[45]M. Hutchings, Solid State Physics, 16 , 227 (1964).

[46] A. Scheie, PyCrystalField, (2018), GitHub repository, https://github.com/asche1/PyCrystalField

[47] A. Abragam and B. Bleaney, Electron Paramagnetic Resonance of Transition Ions, 1st ed. (Clarendon Press, Oxford, 1970).

[48] J. G. Rau, E. K.-H. Lee, and H.-Y. Kee, Phys. Rev. Lett. 112, 077204 (2014).

[49] H. B. Cao, A. Banerjee, J.-Q. Yan, C. A. Bridges, M. D. Lumsden, D. G. Mandrus, D. A. Tennant, B. C. Chakoumakos, and S. E. Nagler, Phys. Rev. B 93, 134423 (2016).

[50] G. Jackeli and G. Khaliullin, Phys. Rev. Lett. 102, 017205 (2009).

Chapter 3 Growth and Characterization of Iron Scandium Sulfide ($FeSc_2S_4$)

Large portions of this work were co-written with the following authors, published under the following citation:

J. Cryst. Growth **454**, 128-33 (2016).

Jennifer R. Morey*[,a,b], K.W. Plumb[b,c], C.M. Pasco[a,b], B. A. Trump[a,b], Tyrel M. McQueen[a,b,c,d], S. M. Koohpayeh [b,c]

[a]Department of Chemistry, Johns Hopkins University, Baltimore, Maryland 21218, USA

[b]Institute for Quantum Matter, Johns Hopkins University, Baltimore, Maryland 21218, USA

[c]Department of Physics and Astronomy, Johns Hopkins University, Baltimore, Maryland 21218, USA

[d]Department of Material Science, Johns Hopkins University, Baltimore, Maryland 21218, USA

Section 3.1 Introduction

Iron scandium sulfide, a cubic spinel of the form AB_2X_4, Figure 3.1(a), is a material of great interest as a candidate spin-orbital liquid (SOL), and has been the subject of many experimental [3-8] and theoretical studies [9-11]. The nature of SOL's remains an elusive subject for experimental observation, and the synthesis of more candidate SOL's enables further study in this area. Unfortunately, progress in understanding and utilizing $FeSc_2S_4$ has been hampered by the lack of stoichiometric powders and single crystals.

Previously reported growths of single crystal $FeSc_2S_4$ are via the iodine chemical vapor transport method [12]. Unfortunately, crystals produced in this fashion are quite small, yielding typical crystals of volume ~6 μm^3 after 30 days of reaction, and are often not quite stoichiometric due to changes in Fe/Sc ratio and substitution of I for S [12]. Here we report the first growths of stoichiometric single crystals of $FeSc_2S_4$ by the travelling solvent technique [13, 14], with FeS as a solvent, in an optical heating furnace. Further, we present a synthetic route to stoichiometric, polycrystalline $FeSc_2S_4$ that does not involve the use of toxic and explosive H_2S gas.

Section 3.2 Experimental Methods

3.2.1 Preparation of Polycrystalline $FeSc_2S_4$

Some of the main difficulties associated with the growth of this material are (1) the volatilization of sulfur during each stage of the precursor synthesis and growth process, and (2) the reactivity of precursor materials with quartz and alumina crucibles. Additionally, Fe, FeS, Sc_2S_3, and $FeSc_2S_4$ are all moisture sensitive, and thus were handled in an argon glovebox with $pO_2 < 2$ ppm and $pH_2O < 1$ ppm.

FeS powder was synthesized by heating stoichiometric amounts of sulfur pieces (99.999%, metals basis, Alfa Aesar) and vacuum remelted iron (99.99%, low oxygen, Alfa Aesar) in an evacuated quartz ampoule. Sc_2S_3 powder was synthesized by heating scandium metal pieces (99.9%, distilled dendritic (REO), Alfa Aesar) and sulfur pieces (99.999%, metals basis, Alfa Aesar) in a boron nitride (BN) crucible in an evacuated quartz ampoule. BN was used to prevent the reaction of scandium with quartz.

Sulfur volatilization limits the size of the quartz ampoules used by this method, as gaseous sulfur exerts an enormous amount of pressure in the tube. Ultimately, tubes of size 12x16 mm (IDxOD) were found to work best for larger scale (1 g) syntheses, and 4x6 mm tubes for smaller batches. Sc_2S_3 is the most sulfur rich phase in this system, so excess sulfur may be added to account for

volatilization during sealing of the ampoule.

To prepare $FeSc_2S_4$ powder, FeS and Sc_2S_3 in a 1:1 molar ratio were ground together, pressed into a pellet, sealed in an evacuated quartz ampoule, and double sealed into a larger evacuated quartz ampoule. This was quickly heated to 500 °C, held for 2h, then heated at a rate of 50 °C/hr to 1000 °C. The furnace was allowed to cool to room temperature after 30 hours of reaction at 1000 °C.

Powder X-ray diffraction patterns were collected on a Bruker D8 Focus diffractometer with a LynxEye detector using Cu Kα radiation. Lattice parameters and Rietveld refinements were performed using Topas 4.2 (Bruker).

3.2.2 Single crystal growth of $FeSc_2S_4$

The pure polycrystalline $FeSc_2S_4$ powder and solvent (FeS) in a 2-3:1 mass ratio were placed in a pyrolytic boron nitride crucible with the solvent at the bottom of the container. The crucible was sealed in a quartz tube under 0.3 bar argon and placed vertically in an optical heating furnace (Crystal Systems Inc. FZ-T-4000-H-VII-VPO-PC). The focused radiation at 80-85% lamp power melted the solvent which was then moved along the polycrystalline $FeSc_2S_4$ powder at a traveling rate of 0.3 mm/h. Single crystals of mm size were grown by this technique.

3.2.3 $FeSc_2S_4$ crystal characterization

Single crystal X-ray diffraction data were collected using a SuperNova diffractometer equipped with an Atlas detector, irradiated with Mo Kα. The cuboid crystal, cut from a larger crystal piece, was mounted with Paratone-N oil. Diffraction patterns were analyzed using the CrysAlisPro software suite, version 1.171.36.32 (2013), Agilent Technologies. This software was also used to perform data reduction. Initial structural models were developed using SIR92 [15] and refinements of this model were done using SHELXL-97 (WinGX version, release 97-2) [16].

Crystal alignments were done using back-reflection Laue diffraction. Selected area electron diffraction was done using a Phillips CM300 atomic resolution transmission electron microscope with a field emission gun and a bottom mounted Orius CCD camera. The accelerating voltage was 300 kV.

3.2.4 Magnetization and Specific Heat Measurements

Magnetization and heat capacity measurements were made on both $FeSc_2S_4$ powder and single crystals using a Quantum Design Physical Properties Measurement System. Magnetization data was collected from T = 1.9 -300 K under applied fields of $\mu_0 H$ = 0.1-0.5 T. For single crystals, the field was applied along the [100] direction. Zero field heat capacity was collected from T = 1.9 to T = 70 K.

Field-dependent specific heat was collected up to $\mu_0 H = 14$ T from $T = 1.9$ K to T = 20 *K*. Curie-Weiss analysis was performed over the temperature range 50 K < T < 200 K, where previous reports indicate a region of linearity in the inverse susceptibility [3].

Section 3.3 Results and Discussion

Rietveld refinements to a typical powder X-ray diffraction pattern from the as-prepared polycrystalline material, Figure 3.1(b), show a structure consistent with previous reports: cubic, spacegroup $Fd\bar{3}m$, with lattice parameter *a* =10.5184(1) Å at room temperature. Previously reported values of *a* at room temperature are 10.606 Å[6] and 10.52 Å[7]. Further, no structural distortions other than minor lattice contraction were observed by laboratory powder X-ray diffraction down to 12 K (data not shown).

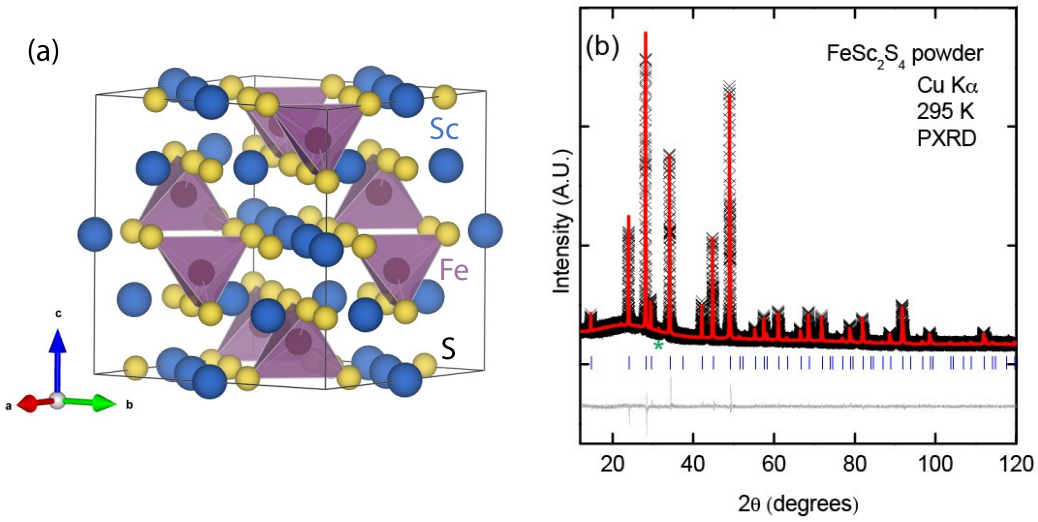

Figure 3.1 Structure and refinement of FeSc2S4 in spacegroup $Fd\bar{3}m$. **(a)** The spinel (AB_2X_4) unit cell of $FeSc_2S_4$. Fe (purple) is tetrahedrally coordinated by S (yellow) and sits on the A-site diamond sublattice. Sc (blue) is octahedrally coordinated and occupies the B-site. **(b)** Powder X-ray diffraction pattern of polycrystalline $FeSc_2S_4$. The experimental data is plotted as black symbols. A refinement of the model to the $Fd\bar{3}m$ space group is plotted as a red curve, and the difference between the data and the fit is plotted below in gray (R_{wp} = 3.344). The *hkl* indices are represented by vertical ticks. The peak corresponding to an added internal Si standard is marked with a green asterisk.

As reported in the Sc_2S_3-FeS phase diagram [17], $FeSc_2S_4$ cannot be synthesized by simply melting and cooling of the stoichiometric composition since it does not melt congruently. However, this compound can be grown with excess FeS by the traveling solvent technique using a high temperature optical furnace. Figure 3.2(a) shows a schematic of the mounting used to achieve this goal; given the high temperature (above 1517 °C) required, it was necessary to use a pyrolytic boron nitride crucible to avoid reaction with quartz; the boron nitride also acts as a thermal standoff to avoid melting the quartz.

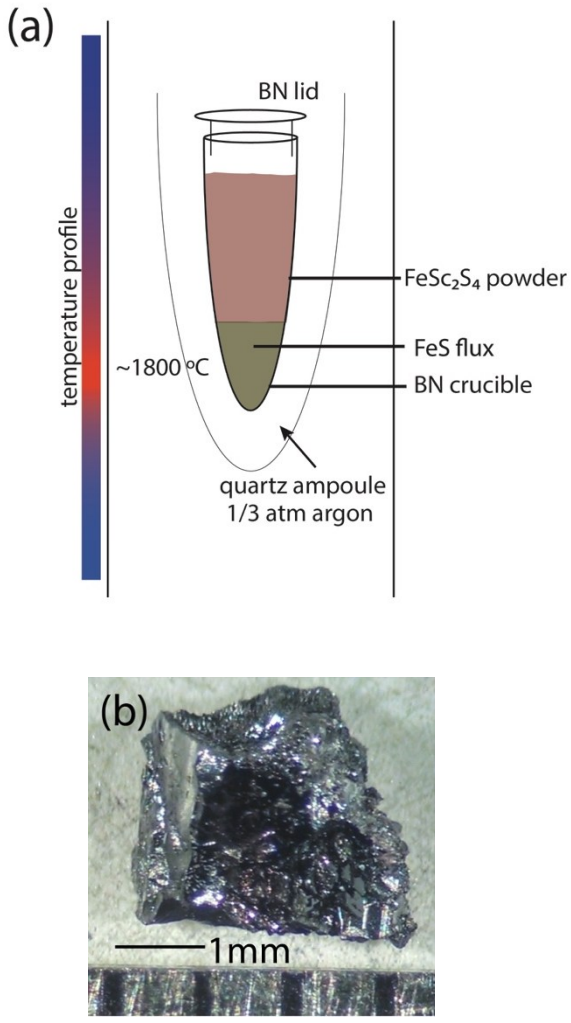

Figure 3.2 Schematic and example $FeSc_2S_4$ crystal. (a) Diagram of traveling solvent in a container using optical heating. The temperature profile used during the growth is indicated by a bar on the side, where the temperature of the hot zone (red) is above 1517 ºC, based on the lamp power used and the phase diagram of this system [16]. (b) One crystal grown by this method, with dimensions approximately 4x4x2 mm. Facets are observable in this crystal.

A representative crystal grown by this technique is shown in Figure 3.2(b), oriented with the (100) plane facing the camera, confirmed by back-reflection Laue diffraction, Figure 3.3(a). Consecutive Laue patterns collected across the length of this crystal show a uniform orientation. A Laue pattern from a second crystal

growth, also along the (100) plane, is shown in Figure 3.3(b).

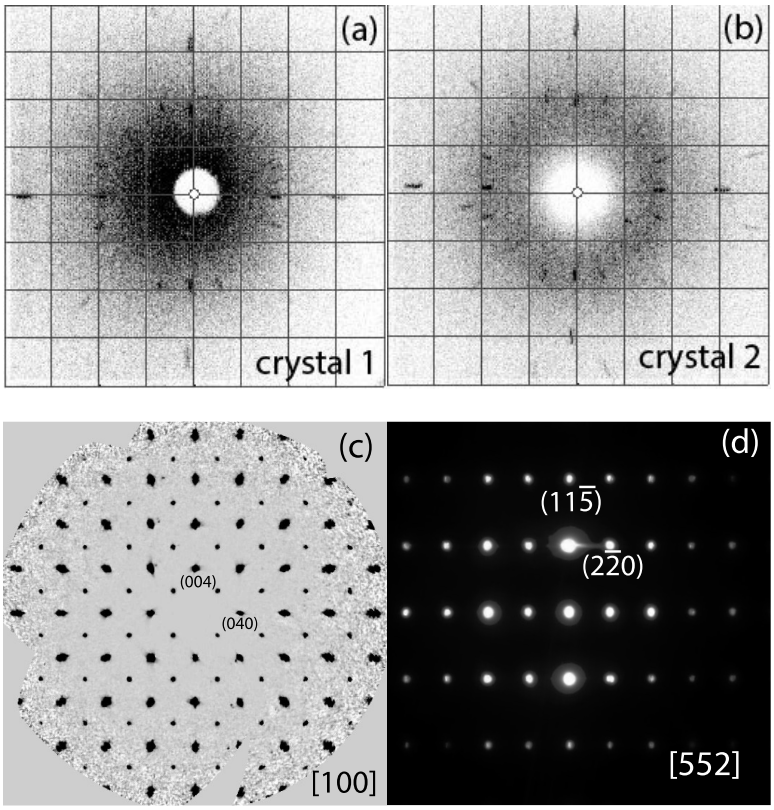

Figure 3.3 Diffraction patterns of single crystals and crystallites. (a-b) Representative back-reflection Laue diffraction patterns of the (100) face from $FeSc_2S_4$ crystals from two different growth runs. (c) Precession image from single crystal diffraction of $FeSc_2S_4$ crystal cut from a larger crystal piece. This image corresponds to the single crystal refinement results shown in Table 3.1 and Table 3.2. (d) Selected area electron diffraction in the [552] direction from a crystallite in the polycrystalline sample. No diffuse scattering was observed.

To determine whether samples produced in this fashion have appropriate stoichiometry, we carried out an extensive series of structural and physical property measurements. First, as expected from the precession images, shown in

Figure 3.3(c), modeling of single crystal X-ray diffraction data yielded a fit consistent with the $Fd\bar{3}m$ spacegroup, with a cubic lattice parameter a = 10.5097(2) Å at T = 110(2) K. This is also in agreement with selected area electron diffraction (SAED) images (Figure 3.3(d)) of $FeSc_2S_4$, which show no diffuse scattering and indicate that at room temperature, $Fd\bar{3}m$ symmetry is maintained even on the local scale. Sulfur deficiency and partial occupancy of Fe or Sc sites, equivalent to a change in Fe:Sc ratio, were not observed in any tested models. Antisite mixing of the form $Fe_{1\pm x}Sc_{2\pm x}S_4$ did not improve the quality of the refinement, and were held fixed at their ideal values. Explicitly, 3.5% site mixing had the effect of increasing R_1 by 7% and *GooF* by 10%. Thus, within the limits of detection of single crystal diffraction, the pieces produced here have appropriate stoichiometry.

Table 3.1 Crystallographic parameters for the first $FeSc_2S_4$ crystal obtained from model fits to the X-ray diffraction data. Absorption correction was analytical using a multifaceted crystal model.

Temperature (K)	110(2)
Space Group	$Fd\bar{3}m$
a (Å)	10.5097(2)
V(Å^3)	1161
Crystal Size (mm)	0.155 x 0.146 x 0.127
Collected Reflections	7932/165 unique
θ_{max} / Completeness	36.13 / 1.000
μ/mm	6.022
Transmission min/max	0.503/0.576
R_{eq}	0.0245
GooF	1.417
R_1 [$F^2>2\sigma(F^2)$]	0.0261
wR_2 (F^2)	0.0686
$\Delta\rho_{max}$ (Å^{-3})	2.59
$\Delta\rho_{min}$ (Å^{-3})	-1.42

Table 3.2 Atomic coordinates and atomic displacement parameters for $FeSc_2S_4$ in the $Fd\bar{3}m$ spacegroup. All occupancies refined to unity within error and thus were fixed at full occupancy in the final refinement.

Atom	Wyckoff site	x	y	z	$U_{11}=U_{22}=U_{33}$ (Å^2)
Fe1	8*a*	1/8	1/8	1/8	0.0054(2)
Sc1	16*d*	1/2	1/2	1/2	0.0048(2)
S1	32*e*	0.25553(3)	0.25553(3)	0.25553(3)	0.0049(2)

A comparison between the physical properties of polycrystalline and single crystal samples was done to confirm the quality of the grown crystals of $FeSc_2S_4$. Figure 3.4 shows a comparison of dc magnetic susceptibilities ($\chi \sim M/H$) at $T < 50$ K between previous literature powder data, data from the polycrystalline material

prepared in this work, and data from two of our single crystals. Our powder and single crystals have similar behavior to the literature specimens, except in the low temperature regime where there is a pronounced roll-over in our measurements. The difference likely arises due to a greater density of defects in the literature samples: it is commonly observed in quantum magnetic materials that the presence of small non-stoichiometries or other defects results in the appearance of a Curie-tail, i.e. rising magnetic susceptibility, at low temperatures. This hypothesis is further supported by comparison of our data to literature ^{45}Sc NMR data [5], which also shows a roll-over; NMR, unlike bulk magnetization measurements, directly probes the intrinsic local susceptibility and is much less sensitive to the defects that give rise to the Curie-tail effect. Based on these magnetization measurements, it appears that the polycrystalline samples here have a lower defect density than previously reported, and that the single crystals behave similarly.

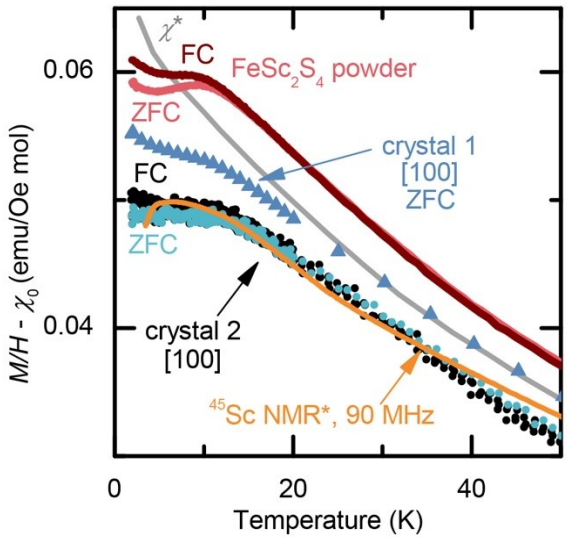

Figure 3.4 Magnetic susceptibility of polycrystalline and single crystal $FeSc_2S_4$. Comparison of magnetic susceptibilities of polycrystalline $FeSc_2S_4$ measured at $\mu_0 H = 1$T (solid gray)[3], the polycrystalline material in this work, measured at $\mu_0 H = 0.5$T (red points), two $FeSc_2S_4$ crystals oriented to [100] at $\mu_0 H = 0.1$T (light blue/black circles) and $\mu_0 H = 0.5$T (dark blue triangles) and the susceptibility measured via ^{45}Sc NMR Knight Shift at 90 MHz (solid orange line) [5]. Powder and crystal measurements from this work exhibit a peak at $T = 11$K, in agreement with the NMR Knight shift data. Asterisks denote data taken from literature.

A Curie-Weiss analysis of the magnetic data in the paramagnetic regime gives parameters in agreement with previous reports, Table 3.3. The Weiss temperatures, θ_w, are negative, indicating net mean field antiferromagnetic interactions. The Curie constants, C, correspond to effective magnetic moments, p_{eff}, that are in good agreement with the spin-orbital model for Fe^{2+} on a tetrahedron that predicts $p_{eff} = 5.32$. One significant difference between our results and prior literature is the presence of a non-negligible temperature-independent

contribution, χ_0, in the present samples. This is most likely due to the presence of residual contributions from residual travelling solvent, FeS, which is a ferromagnetic metal at all temperatures measured here. Residual FeS is likely contributing to the unreliably large θ_w in Crystal 2 (Table 3.3), which is significantly more negative than is seen in the other samples. The error on this calculated value is particularly large (20%), but the calculated χ_0-subtracted susceptibility is well in line with other samples in this and other work (Figure 3.4). Based on the reported saturation magnetization for FeS, we can estimate between 0.05% and 0.2% FeS in samples reported here[18]. The presence of these inclusions precludes more precise comparisons. Future optimization of the traveling solvent technique as applied here is expected to be able to eliminate these inclusions.

Table 3.3 Curie-Weiss analysis of $FeSc_2S_4$: polycrystalline material in this work and reported in literature [1], and two grown crystals. *C* is the Curie constant (emu K Oe^{-1} mol f.u.$^{-1}$), θ_w (K) the Weiss Temperature, p_{eff} the effective magnetic moment per ion, and χ_0 the temperature independent contribution to the magnetic susceptibility (emu Oe^{-1}).

	Powder	Lit. Powder	Crystal 1	Crystal 2
C	3.45(5)	3.28	3.60(5)	3.5(2)
θ_w	-42(2)	-45.1	-54(5)	-100(20)
p_{eff}	5.3(1)	5.12	5.4(3)	5.3(3)
χ_0	0.0311		0.07274	0.17748

Figure 3.5 shows a comparison of heat capacity measurements on published powder data [3] versus the polycrystalline and single crystal samples prepared in

this work. In all cases, there is a broad maximum in C/T at T ~ 10 K. The maximum is at a slightly higher temperature and sharper in the specimens of this work, consistent with the presence of fewer defects (which tend to broaden transitions). These differences are not attributable to the presence of FeS inclusions, since there is only a weak field dependence to the specific heat (inset). The magnetic contribution to specific heat ($C_{magnetic}$) was estimated by subtracting the phononic contribution (C_{phonon}) from the total specific heat in each case. We used existing literature data on $CdIn_2S_4$, which has no magnetic degrees of freedom, and scaled it based on the change in atomic masses per known methods[19]. The results are shown in Figure 3.5 and are similar amongst all four datasets. Note that our integrated entropies differ from that of Fritsch et al.[3] due to a difference in how the non-magnetic heat capacity was scaled (future work with a more closely atomic weight matched analog is necessary to unambiguously resolve which is more accurate). Both the powder and the single crystals recover entropy to approximately 70% of Rln(5). The value Rln(5) corresponds to the spin and orbital degrees of freedom for Fe^{2+} in a tetrahedral coordination. The presence of a transition at low temperatures was explored by Plumb et al. [8] who observed evidence for a tetragonal distortion in this material at T ~ 11K. The physical basis of this peak at low temperatures is still under investigation. Synthesis of large single crystals will further enable this exploration.

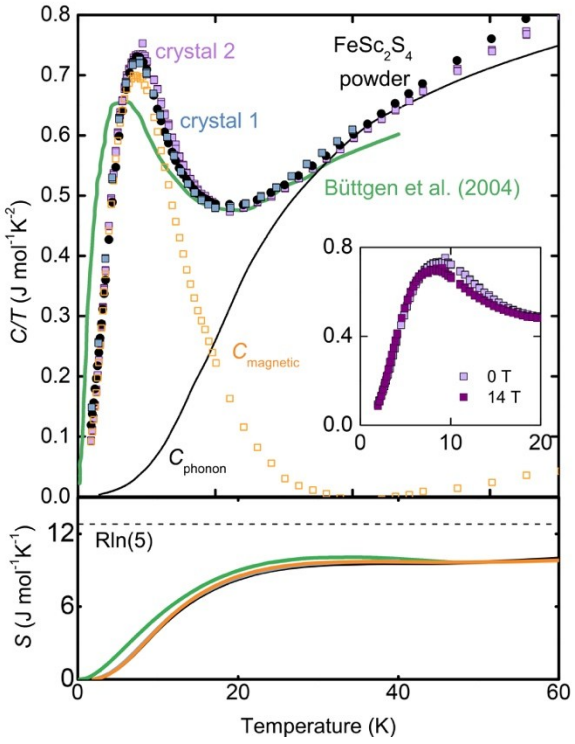

Figure 3.5 Heat capacity of polycrystalline and single crystal $FeSc_2S_4$. (a) Heat capacity measurements on crystal 1 (blue squares) and crystal 2 (purple squares) are consistent with measurements on the powder (black circles). Both show a broad peak between T = 2 K and T = 15 K that responds minimally to fields up to $\mu_0 H$ = 14 T. The peak is slightly higher in temperature and sharper than reported heat capacity data for polycrystalline samples [3]. (b) Integrated entropy, and thus number of spin and orbital degrees of freedom involved, are similar between all four samples.

Section 3.4 Continued Work

In short, we report the successful preparation of polycrystalline powder and mm-scale single crystals of stoichiometric iron scandium sulfide by the travelling solvent technique. This paves the way to finally understanding this fascinating material, with future optimizations to improve the purity and size of single

crystals. The use of an optical furnace to perform a traveling solvent crystal growth in a container is also adaptable to a wide range of other complex quantum materials [13].

3.4.1 Neutron Scattering

The samples from this work were used in subsequent neutron scattering experiments to investigate spin wave excitations and possible orbital ordering in this material. One of the significant differences between the measurements made on these samples and those on the others reported in the literature is the broad antiferromagnetic feature at T = 10 K in magnetization measurements. Temperature dependent neutron scattering measurements revealed magnetic Bragg peaks arising from long range magnetic order, **Figure 3.6**. The peaks begin to appear around T = 10 K, and increase in intensity as temperature decreases.

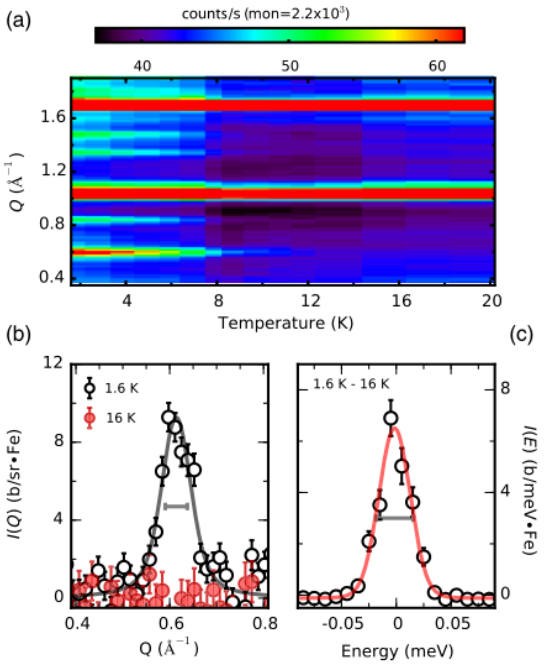

Figure 3.6 (a) Temperature dependent neutron scattering of $FeSc_2S_4$. (b) A magnetic Bragg peak is apparent at $T = 1.6$ K that was not present at $T = 16$ K. (c) Energy dependence of the Bragg peak. Reproduced from Plumb, Morey et al., 2016.

Magnetization measurements suggested antiferromagnetic interactions, and solved magnetic structures agree with this. As mentioned Chapter 2, according to Landau Theory, one irreducible representation should be sufficient to describe the order resulting from a second order phase transition. There was no single IR capable of describing the data in the presumed structural space group, Fd-3m. However, lowering the symmetry to a tetragonal subgroup, I-4m2, then made it possible to use one IR. The result of this symmetry lowering is a metrically cubic unit cell that hosts tetragonal distortions of the Fe^{2+} tetrahedra,

resulting in two symmetrically non-equivalent iron sites, shown in Figure 3.7. This is consistent with earlier Moessbauer Spectroscopy data on $FeSc_2S_4$, which ascribed the two-site signal to Fe-Sc site mixing; no evidence for site mixing was found in the crystalline or polycrystalline scattering experiments done in the present studies.

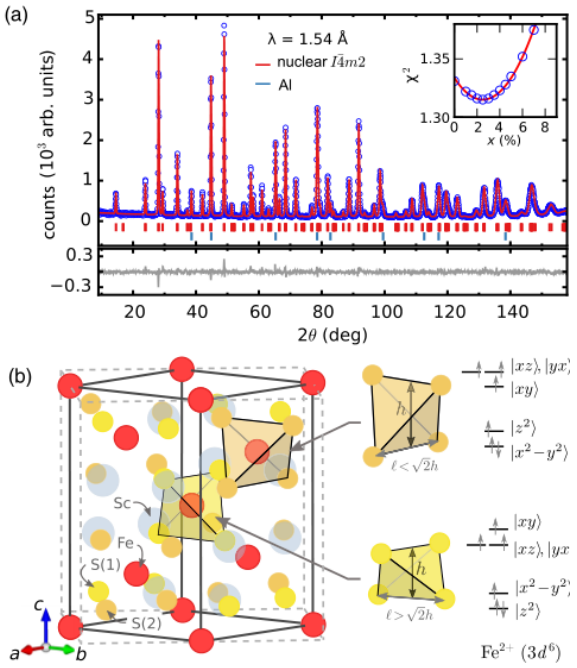

Figure 3.7 (a) Neutron scattering of $FeSc_2S_4$ and Rietveld refinement in I-4m2. (b) Tetragonal unit cell. Distortions of the tetrahedra lead to a breaking of magnetic degeneracy. Reproduced from Plumb, Morey et al., 2016.

There were multiple candidate magnetic structures, resulting in the inability to distinguish between the k vectors $\vec{k} = (\frac{1}{2}, \frac{1}{2}, 0)$. and (0 0 1) in the above scatting data, but, notably, the two solutions resulted in the same moment; the

direction is not uniquely resolvable. However, inelastic magnetic neutron scattering was used to determine that the correct propagation vector in this case is $\vec{k} = (\frac{1}{2}, \frac{1}{2}, 0)$. The fit to the data with this model is shown in Figure 3.8(a) and the model is visualized in Figure 3.8(b).

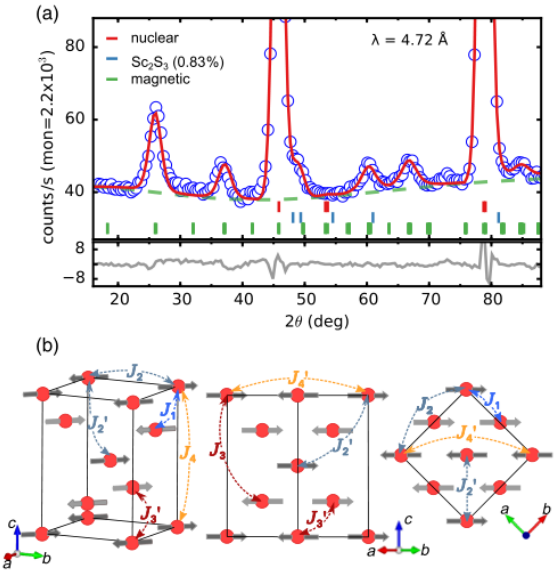

Figure 3.8 (a) Neutron powder diffraction showing the nuclear peaks (red tick marks) and the magnetic peaks (green tick marks) for a propagation vector $\vec{k} = (\frac{1}{2}, \frac{1}{2}, 0)$, and (b) visualization of this structure, with moments in light and dark gray showing the symmetrically distinct Fe sites. Magnetic exchanges, J_i, are also shown. Reproduced from Plumb, Morey et al., 2016.

3.4.2 Short range nuclear structure

The synthesis of high quality polycrystalline and single crystal $FeSc_2S_4$ enabled additional experiments on this system, including local structure analysis and single crystal resistivity. Pair Distribution Function (PDF) analysis is a technique

used to determine local structure in a material, and plots *G(r)*, which is related to a Fourier function in Q-space *S(Q)* as described in the Introduction, against *r* in real-space units. Prior to the above neutron scattering work, $FeSc_2S_4$ was reported as being in the space group Fd-3m.

PDF measurements collected on two samples of $FeSc_2S_4$: one considered 'pristine' which was stored in the glovebox once it was made and was dark gray/black in color, and the other which is considered 'air-exposed' which was taken from the same batch that was used for muon spin resonance experiments. This sample was a medium brown color after having been stored in air for months. The data were collected at the 11-ID-B beamline at the Advanced Photon Source at Argonne National Lab by Kathryn Arpino at index 311 with an energy of 58.66 keV and a wavelength of 0.2112 Å. CeO_2 was used as a calibration standard. Karena Chapman assisted with data work-up during the Modern Methods in Rietveld Refinement for Structural Analysis workshop hosted at Oak Ridge National Laboratory in June 2017.

The space group Fd-3m does fit well to the extended structure of an air-exposed sample of $FeSc_2S_4$ at room temperature, shown in Figure 3.10 X-ray PDF of pristine (black) and air-exposed (green) samples of FeSc2S4. Peak locations where the

two samples differ substantially have been marked with a pink asterisk.. Fit deviations at low *r* are likely due to instrumental broadening parameters.

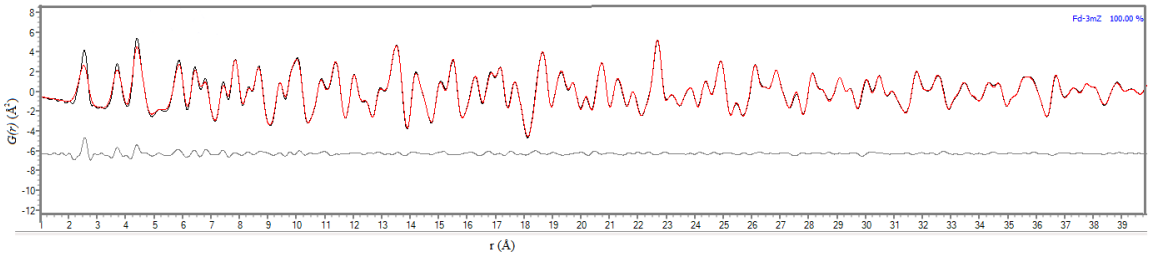

Figure 3.9 Refinement of the space group Fd-3m to an air-exposed sample of $FeSc_2S_4$ at room temperature.

The same data in Figure 3.9 is plotted in Figure 3.10 as the green curve. The pristine sample is plotted as the black curve. The top panel shows the full measured 40 Å range and the lower panel shows the same data in the $0.5 < r < 15$ Å range.

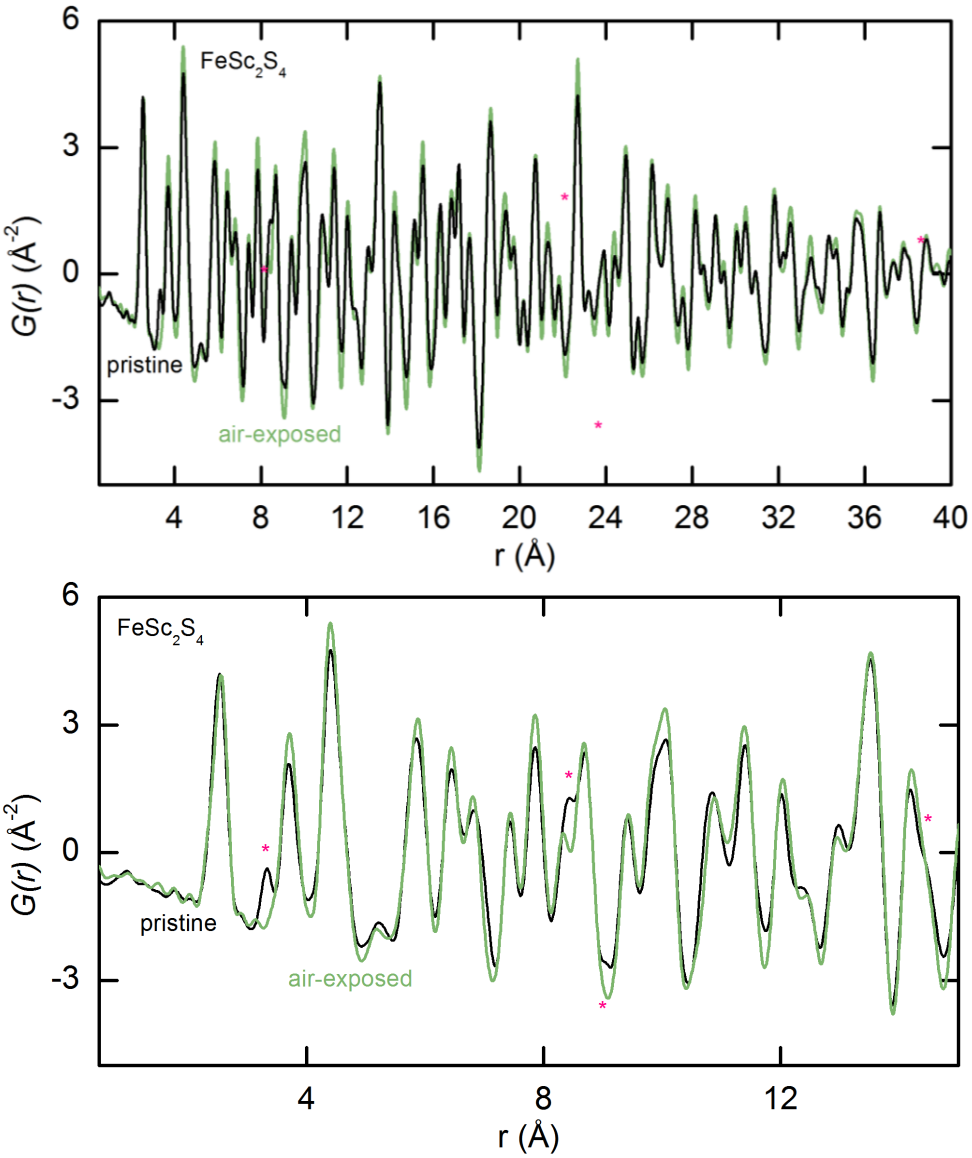

Figure 3.10 X-ray PDF of pristine (black) and air-exposed (green) samples of $FeSc_2S_4$. Peak locations where the two samples differ substantially have been marked with a pink asterisk.

There are notable qualitative differences between the two $FeSc_2S_4$ samples. First, the intensity of the pristine sample is smaller than the air-exposed sample, and decreases more rapidly over the *r* range. This can be an indication that this

material is more disordered than the air-exposed one. There are peaks present in the pristine sample that are not present in the air-exposed sample. These have been marked with pink asterisks in the lower panel of Figure 3.10. The peak at r = Å looks to be a two-contribution peak in the air-exposed (green) data, but that the lower *r* peak has a low intensity. It seems that the higher *r* higher-intensity peak in the pristine sample is one contribution, and that the lower intensity contribution has increased in magnitude and decreased slightly in *r*. In contrast, the lower-intensity lower-*r* peak at *r* = 8.2 Å is at a higher r in the pristine sample. Another peak at r ~ 13.5 Å splits similarly.

There are a few interpretations that can be made of the data, though the quantitative analysis remains to be done. One possibility is that the samples were mixed up, and the one referred to as 'pristine' is actually 'air-exposed', and the extra/shifted peaks come from oxygen-iron and oxygen-scandium bonds and resultant distortions of the lattice. However, it is also possible that these curves are representative of pristine and air-exposed samples as labeled. In this case, it is possible that the extra peaks in the pristine sample are real signatures of the slight distortions of the lattice that can occur in I-4m2 symmetry, which was identified by Plumb, Morey, et al. (2016).

Resistivity measurements on a single crystal of FeSc2S4 oriented along [100], measured from T = 30 K to T = 145 K with an excitation of 1000 μA on a Quantum Design Physical Properties Measurement System show an upward curvature with decreasing temperature, with a relatively small absolutely resistivity of ~ 0.01 Ohm-m, Figure 3.11. This suggest that $FeSc_2S_4$ is a small band gap semiconductor. Linear behavior in $\ln\left(\frac{\rho}{\rho_0}\right) vs. T^{-1/4}$ suggests that the mechanism of conduction in the 2 < T < 150 K temperature range is variable range hopping.

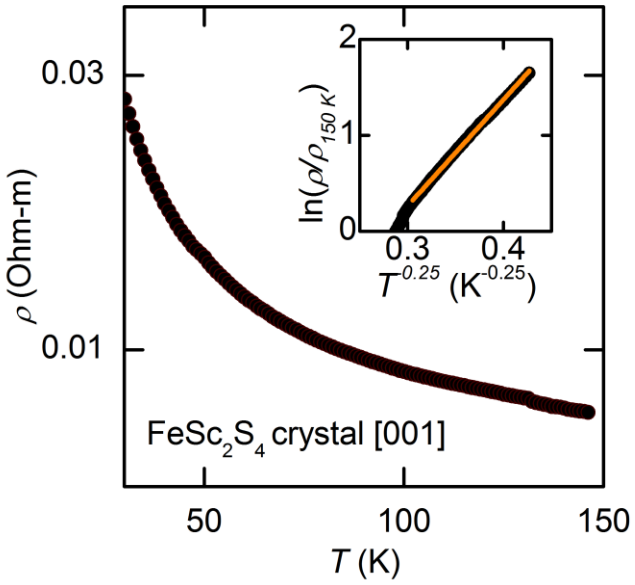

Figure 3.11 Resistivity of a single crystal of $FeSc_2S_4$, measured on the [100] face. Inset: diagram of four-probe measurement configuration, to approximate scale.

References

[1] V. Fritsch, J. Hemberger, N. Büttgen, E.-W. Scheidt, H.-A. Krug von Nidda, A. Loidl, and V. Tsurkan*Phys. Rev. Lett.* **92**, 116401 (2004).

[2] N. J. Laurita, J. Deisenhofer, LiDong Pan, C. M. Morris, M. Schmidt, M. Johnsson, V. Tsurak, A. Loidl, N. P. Armitage, *Phys. Rev. Lett.* **114** 207201 (2015).

[3] N. Büttgen, J. Hemberger, V. Fristch, A. Krimmel, M. Mücksch, H.-A. Krug von Nidda, P. Lunkenheim, R. Fichtl, V. Tsurkan, A. Loidl, *New J. Phys.* **6**, 191 (2004).

[4] S. Reil, S.-J. Stork, H. Haeuseler, *J. Alloys Compd.* 334, 92 (2002).

[5] A. Krimmel, M. Mücksch, V. Tsurkan, M. M. Koza, H. Mutka, A. Loidl, *Phys. Rev. Lett.* **94**, 237402 (2005).

[6] L. Mittelstädt, M. Schmidt, Zhe Wang, F. Mayr, V. Tsurkan, P. Lunkenheimer, D. Ish, L. Balents, J. Deisenhofer, A. Loidl, *Phys. Rev. B: Condens. Matter* **91**, 125112 (2015).

[7] K.W. Plumb, J. R. Morey, J. A. Rodriguez-Rivera, Hui-Wu, A. A. Podlesnyak, T. M. McQueen, C. L. Broholm, Phys. Rev. X 6, 041055 (2016), arXiv:1603:08033

[8] G. Chen, A. P. Schnyder, L. Balents, *Phys. Rev. B: Condens. Matter* **80**, 224409

(2009).

[9] G. Chen, L. Balents, A. P. Schnyder, *Phys. Rev. Lett.* **102**, 096406 (2009).

[10] S. Sarkar, T. Maitra, R. Valenti, T. Saha-Dasgupta, *Phys. Rev. B: Condens. Matter* **82**, 041105 (2010).

[11] A. Tomas, M. Guittard, J. Rigoult, B. Bachet, *Mat. Res. Bull.* **14**, 249 (1979).

[12] R. Triboulet, *Handbook of Crystal Growth*, 2nd Ed., Part A, Ch. 12 (2015) 459.

[13] S. M. Koohpayeh, *Prog. Cryst. Growth Charact. Mater* (2016) doi:10.1016/j.pcrysgrow.2016.03.001 (In Press).

[14] A. Altomare, G. Cascarano, C. Giacovazzo, A. Gualardi, *J. Appl. Cryst.* **26,** 343 (1993).

[15] G.M. Sheldrick, *Acta Cryst,* **A64**, 112 (2008).

[16] O. V. Andreev, N. N. Parshukov, *Russ. J. Inorg. Chem.* **37**, 968 (1992).

[17] F. Grønvold, S. Stølen, A. K. Labban, E. F. Westrum, Jr, *J. Chem. Thermodynamics*, **23**, 261 (1991).

[18] A. Tari, *The Specific Heat of Matter at Low Temperatures* 1st edition, Imperial College Press. (2003).

Chapter 4 Layered Materials

Section 4.2 A Metallic Kagomé Antiferromagnet: KV_3Sb_5

Portions of this work were done in collaboration with Brenden R. Ortiz, who discovered the material, provided samples, solved the structure, and attempted many crystal growths, his advisor Eric S. Toberer at the Colorado School of Mines, and Tyrel M. McQueen at Johns Hopkins University.

4.2.1 Introduction

Like the honeycombs discussed in Chapter 2, the kagomé lattice is another frustrated lattice that is theoretically capable of hosting interesting quantum behavior [1]. One of the strongest candidate materials for hosting a QSL state is the copper kagomé material Herbertsmithite [2, 3]. The search for QSL's has led to the discovery that interesting quantum states, including superconductivity, can arise when metallicity and magnetism coexist. There are theoretical predictions for QSL [4] and antiferromagnetic [5] states on the kagomé lattice, but very few structurally perfect kagomé compounds have been found.

Metallic antiferromagnets are relatively rare, and are much rarer than metallic ferromagnets. And, while metallic kagomé materials [6], and ferromagnetic [7] and antiferromagnetic [2, 4] kagomé materials have been reported, there has never been a report of a metallic antiferromagnetic kagomé.

The discovery of such a material would be a great boon to the community. The zintl-type compound KV_3Sb_5 appears to be a metallic kagomé antiferromagnet.

4.2.2 Experimental Methods

KV_3Sb_5 was made by solid state reaction of elemental constituents, which were reacted in a ball mill for 2 hours, then sieved and sintered in an evacuated quartz ampoule at 600 °C for 48 h. Samples were doped with barium and tin as well. The elemental composition of the barium and tin doped compounds has not been determined. Powder X-ray diffraction patterns were collected at 273 K on the 11-BM beamline at the Advanced Photon Source with a wavelength of 0.412619 Å. Rietveld refinement with the charge flipping method was used to solve the structure.

The magnetization of KV_3Sb_5, barium doped KV_3Sb_5:Ba, and tin doped KV_3Sb_5:Sn powders were measured using a Quantum Design Physical Properties Measurement System (PPMS) from T = 300 K to T = 2 K under an applied field of $\mu_0 H$ = 1 T.

Condensed pellets for heat capacity and resistivity measurements were made via uniaxial hot pressing at 500 °C under 40 MPa of pressure. Heat capacity measurements from T = 11 K to T = 300 K were performed on the PPMS and measurement from T = 0.055 K to T = 3.5 K were measured using a Quantum

Design Dilution Refrigerator. All heat capacity measurements were performed using the semi-adiabatic technique with 3 time constants, each temperature was measured in triplicate. Resistivity measurements were made using the 4-probe technique on bars cut from densified pellets of material.

4.2.3 Results and Discussion

The material was found to crystallize in the centrosymmetric space group P6/mmm, Figure 4.1, determined via Rietveld refinement. Minor impurities of VSb_2 and Sb were detected. This material contains a structurally perfect kagomé network of vanadium ions, separated by layers of antimony and potassium.

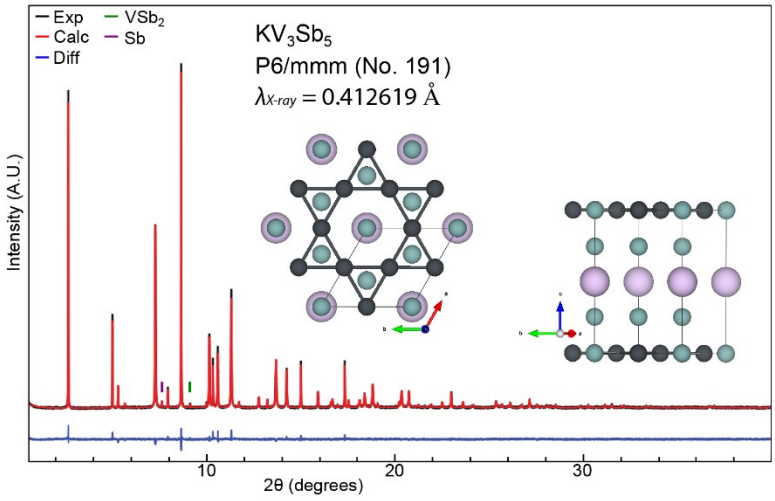

Figure 4.1 Rietveld refinement of KV_3Sb_5 in space group P6/mmm to data from the 11-BM beamline at the Advanced Photon Source, with an X-ray wavelength of 0.412619 Å. Small impurities of VSb_2 and Sb are accounted for. Inset: visualization of the kagomé network and layers.

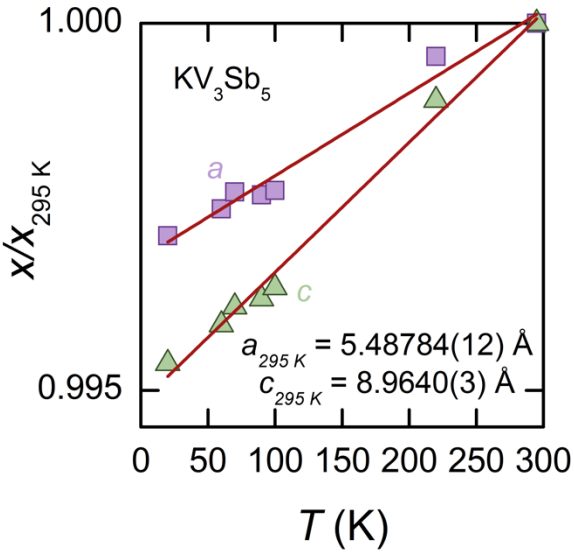

Figure 4.2 Temperature dependence of lattice parameters *a* (purple squares) and *c* (green triangles) of KV_3Sb_5 relative to values at $T = 295$ K.

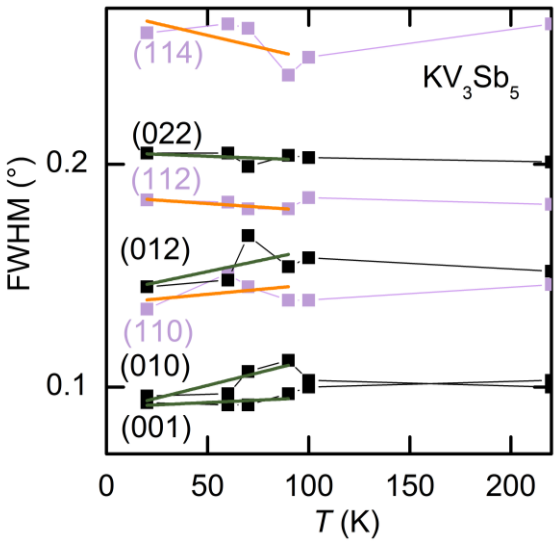

Figure 4.3 Temperature dependence of the full width at half max (FWHM) of seven peaks in PXRD patterns of KV_3Sb_5. Peaks in the (11l) family are purple squares, others are black squares.

Table 4.1 Lattice parameters refined from in-house PXRD patterns at room temperatures.

	a (Å)	*c* (Å)
KV_3Sb_5	5.48169(4)	8.95478(9)
Ba-doped	5.4836(19)	8.9297(4)
Sn-doped	5.48481(4)	8.94018(8)

The *a* and *c* lattice parameters show nearly linear decrease with decreasing temperature, Figure 4.2. The *c* parameter changes more than a across the temperature range. It is unclear from plots of the temperature dependence of the full width at half max (FWHM) of a variety of peaks in PXRD patterns whether there is a structural transition in this material. Peaks with indices (11l) may increase in FWHM at temperatures below $T = 90$ K.

Refinements of the parent, Ba-doped, and Sn-doped samples do have different lattice parameters. Ba and Sn doping both increase the *a* lattice parameter (Sn more than Ba) and decrease the *c* lattice parameter (Ba more than Sn). This suggests that Sn and Ba do truly dope into the bulk material; further work needs to be done to quantify the amount. Nominal values were 10% substitution of K and Sb, for Ba and Sn respectively. It is intuitively believable that Ba doping would decrease the c lattice parameter: K and Ba are interlayer ions and are likely interacting coulombically with the layers. Ba is a 2+ ion, and

so has a stronger coulombic attraction to the kagomé layers. Sn has a larger ionic radius than Sb, and so is possibly straining the kagomé lattice.

The parent compound KV_3Sb_5, as well as the barium and tin toped variants all show weak paramagnetic response and a large Curie tail, seen in the main panel of Figure 4.4. Molar quantities are approximate: the amount of doping of barium and tin is unclear, so all compounds are displayed as per mol of KV_3Sb_5.The kink in the magnetization data is much more obvious when plotted as 1/(M/H - χ_0). Only KV_3Sb_5 displayed Curie-Weiss behavior with the application of a temperature-independent χ_0, of 0.00005. No χ_0 was found to improve the high temperature linearity of the barium and tin doped samples. The Weiss temperature of KV_3Sb_5 was found to be -157 K, and the effective magnetic moment p_{eff}= 0.66 μ_B (C = 0.05445). The Néel temperature of KV_3Sb_5 seems to be 80 K (Figure 4.4, inset). The barium doped material, measured on samples with two different sample amounts, shows a Néel temperature of 100 K, which is 20 K higher than the parent. Tin doping seems to mostly suppress the magnetism and/or possibly move the transition a little lower in temperature.

Though identification of oxidation states in metallic compounds is not necessarily representative of the actual bonding in the material, some insight can be gained into the magnetic behavior by doing so for KV_3Sb_5. Potassium is

generally found as +1, and antimony often as -5, leaving +14 to distribute between the three V ions. V^0 has a valence electron configuration of $4s^2 3d^3$. Two V^{5+} and one V^{4+} would keep the material charge balanced. V^{5+} has a full valence and is therefore likely diamagnetic. V^{4+}, however, should have one unpaired electron and could thus be magnetically active.

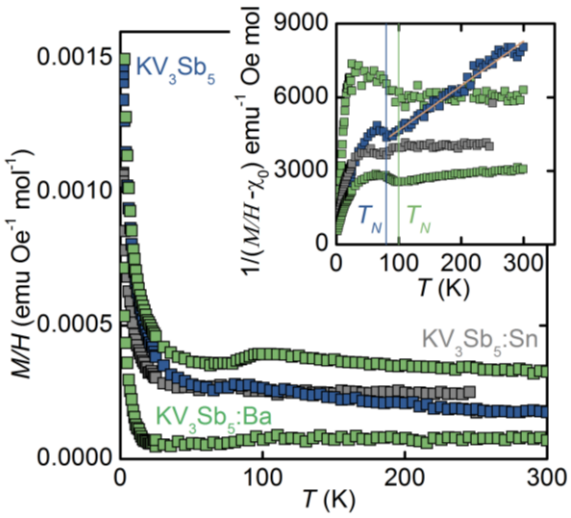

Figure 4.4 Magnetization of KV_3Sb_5, the barium doped KV_3Sb_5:Ba, and the tin doped KV_3Sb_5:Sn showing paramagnetic response down to $T = 2$ K. Inset: KV_3Sb_5 is the only material to show linear Curie-Weiss behavior from $T = 100$ K to $T = 300$ K.

The specific heat of KV_3Sb_5 from $T = 11$ K to $T = 300$ K shows no sharp features, Figure 4.5. However, there is a bump at $T = 80$ K that is reproducible on warming and cooling, and at $H = 2$ T and $H = 5$ T. This is the same temperature as the antiferromagnetic feature in the magnetization data, possibly a Néel AFM ordering temperature. Heat capacity is a bulk measurement, and therefore it is

likely that the antiferromagnetic feature in the magnetization is a signature of bulk antiferromagnetism in the material. Similarly, there is a subtle bump in the heat capacity of the barium doped KV_3Sb_5 at T = 100 K. This is the temperature that the antiferromagnetic feature in the barium doped material appears in magnetization; again, this implies that the antiferromagnetism is a bulk property, and that doping with barium increased the strength of the interactions.

Barium likely substitutes in for potassium in the structure, as these elements are chemically similar. Barium is almost always found as a 2+ ion, whereas K is 1+. So, returning to the discussion of oxidation state in the material above, the substitution of barium could add another magnetic spin ½ to the unit cell as it induces V^{4+} to become V^{3+}. While this could cause the transition temperature to increase (as the strength of the magnetic exchanges increases), it does not explain the lack of observable Curie-Weiss behavior in barium-doped KV_3Sb_5. Though this could be due to the small absolute magnitude of the measured signal.

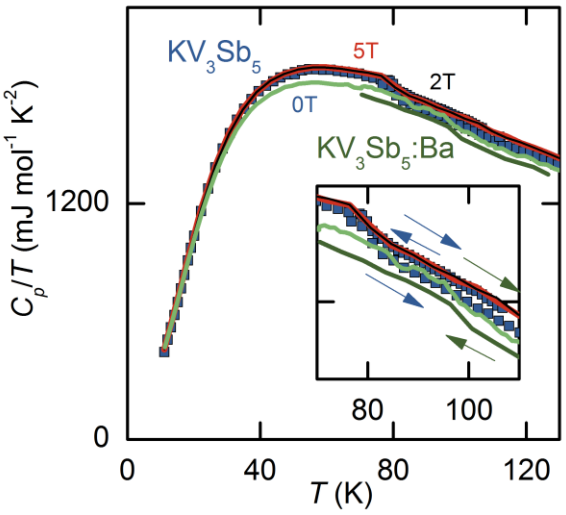

Figure 4.5 Heat capacity of KV_3Sb_5 at $\mu_0 H = 0$ T (blue squares), 2 T (thin black line), and 5 T (thick red line). Inset: There is a feature at $T = 80$ K that is reproducible on heating and cooling (indicated by arrows) and is present all measured fields.

A linear fit to the DR HC data shows a fairly large gamma contribution, which is characteristic of a metal. The lowest temperature measurements, between 250 mK and 500 mK show hysteresis on cooling and warming. The origin of the heat capacity peak at the lowest temperatures is unclear – perhaps magnetism, perhaps a nuclear contribution.

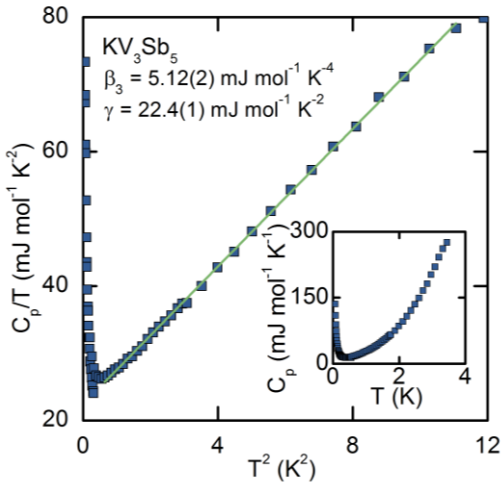

Figure 4.6 Low temperature heat capacity plotted as C_p/T versus T^2 of KV_3Sb_5. A linear fit to the 1 K < T < 3.2 K region (green line) fit to the equation $C_p/T = \gamma T^2 + \beta_3$ gives β_3 = 5.12(2) mJ mol^{-1} K^{-4} and γ = 22.4(1) mJ mol^{-1} K^{-2}. Inset: C_p versus T has no sharp features above T = 0.25 K.

The resistivity of all three materials measured is characteristic of a metal: it decreases with decreasing temperature (Figure 4.7) .The resistivity of the barium doped sample and the parent compound almost exactly overlay. The tin-doped compound shows slightly higher resistivity throughout the temperature range, dropping to a vanishingly small resistivity at T = 4 K. This is ascribed to a possible tin impurity; elemental tin is known to superconduct at T = 4 K. Elemental analysis will enable further understanding of this behavior.

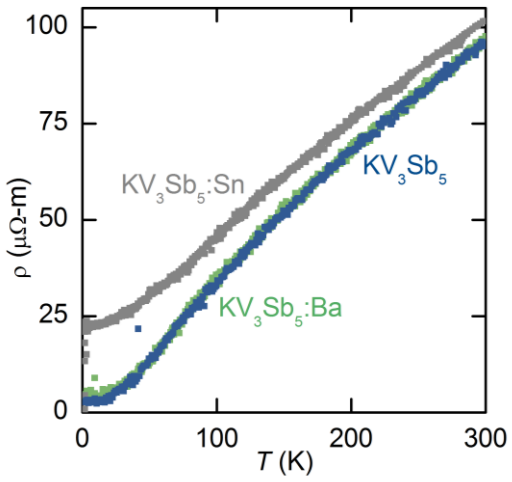

Figure 4.7 Resistivity of KV_3Sb_5 (dark blue) and its barium-doped (green) and tin-doped (grey) derivatives.

4.2.4 Conclusions and Future Work

KV_3Sb_5 is the first realization of a metallic antiferromagnet kagomé lattice. The metallicity, measured by resistivity and confirmed by linear fits to low temperature heat capacity measurements, is robust under doping with tin and barium. KV_3Sb_5 appears to have a weak AFM transition. Further work will be done to characterize the structure. Neutron scattering experiments could be done to solve the ordered magnetic state. While natural vanadium has mostly large incoherent scattering cross section (5.08 barns) and small coherent cross section (0.0184 barns), making it excellent as a material for sample canisters, the isotope ^{50}V has a large bound coherent scattering cross section (7.3(1.1) barns).and a much smaller bound incoherent scattering cross sections (0.5 barns). So, samples prepared with isotopically pure ^{50}V. All isotopes of potassium have relatively

small and similar coherent scattering cross sections, no greater than 1.76 barns with 0.27 barns of incoherent cross section, so isotopic substitution of K will likely not improve the measurement.

4.2 Small band gap metal organic frameworks

Portions of this work were done in collaboration with Mircea Dinca at the Massachusetts Institute of Technology and his students, who discovered the materials, provided samples, and solved the structures, and Tyrel M. McQueen at Johns Hopkins University.

4.2.1 Introduction

Metal organic frameworks (MOF's) are a class of materials defined by metal centers connected by organic linkers. The nature of the metal and the organic linker, as well as the structure, are what dictate the properties of the material. MOF's are employed for many applications in a wide variety of fields, from electrocatalysis {8- 10] to applications as field effect transitors [11]. Many MOF's are insulating or somewhat conductive, but there are few reports of metallicity in MOF's, and no reports of superconductivity in MOF's [12]. Nickel hexaiminobenzene ($Ni_3(HIB)_2$; $Ni_3(C_6N_6H_6)_2$) and copper hexaiminobenzene ($Cu_3(HIB)_2$; $Ni_2(C_6N_6H_6)_3$) have been reported to show metallic character above T = 300 K [13]. They crystallize in a layered structure, visualized in Figure 4.8.

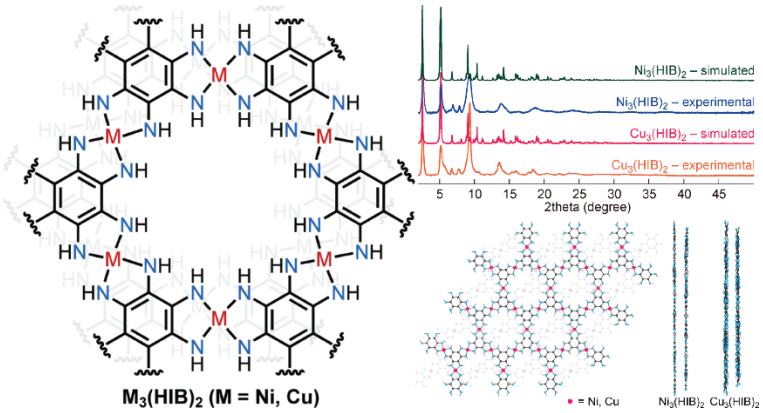

Figure 4.8 Visualization of the structure of $M_2(HIB)_2$, M= (Cu, Ni) and comparison of experimental and calculated powder x-ray diffraction patterns. Adapted from Dou et al. (2017) [13].

4.2.2 Results and Discussion

Despite reports of metallicity, temperature dependent resistivity measurements done at $\mu_0 H = 0$ T and $\mu_0 H = 3$ T, Figure 4.9, show that resistivity on the order of 30 Ohm-m in $Ni_3(HIB)_2$ and 5.00×10^5 Ohm-cm in $Cu_3(HIB)_2$ increases with deceasing temperature. This behavior and these resistivity values are consistent with two relatively small band gap semiconductors. A fit of a linear region in a plot of the natural log of the resistivity normalized to the resistivity at $T = 300$ K versus inverse temperature gives band gaps of $E_g = 23.4$ meV for $Ni_3(HIB)_2$ and $E_g = 103.2$ meV for $Cu_3(HIB)_2$, which are calculated based on the relationship $\ln(\rho_T/\rho_{300\,K}) = 2k_B E_g T^{-1} + b$ where k_B is the Boltzmann constant, E_g is the band gap, and b is the intercept of the line.

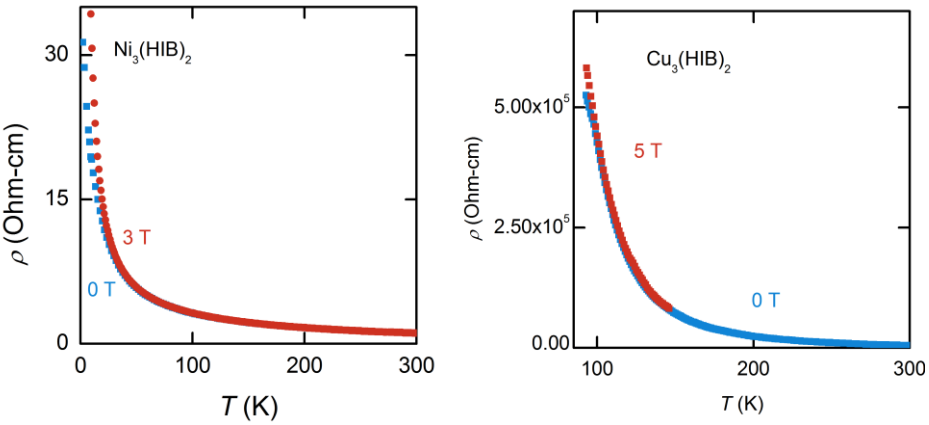

Figure 4.9 Resistivity measurements of (left) $Ni_3(HIB)_2$ and (right) $Cu_3(HIB)_2$, measured at fields of $\mu_0 H = 0$ T (blue) and $\mu_0 H = 3$ T (red).

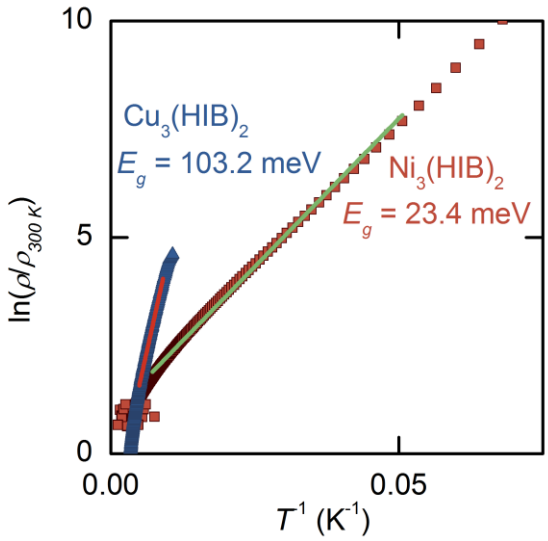

Figure 4.10 The natural log of the temperature-dependent resistivity normalized to the resistivity at $T = 300$ K plotted against inverse temperature for $Ni_3(HIB)_2$ (brown) and $Cu_3(HIB)_2$ (blue).

One of the hallmarks of metallic behavior is a linear heat capacity at low temperatures when plotted as C_p/T versus T^2 with a large γ when fit to the equation $C_p/T = \gamma T^2 + \beta_3$. For $Ni_3(HIB)_2$, this fit gives $\beta_3 = 0.0043(8)$ mJ mol^{-1} K^{-4}

and γ = 0.148(4) mJ mol^{-1}K^{-2}. The R^2 metric of the quality of the fit is 0.9921, which indicates that this fit is not excellent. Indeed, visually, this region is not quite linear. Further, the γ obtained is much smaller than one would expect for a metal, further supporting the identification of these materials as small band gap semiconductors.

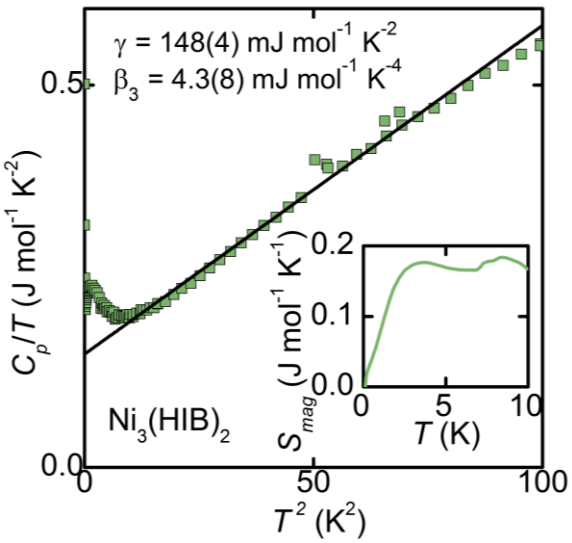

Figure 4.11. Heat capacity measurement of $Ni_3(HIB)_2$ plotted as C_p/T versus T^2 to highlight possible linearity indicating metallic behavior. A linear fit of the data fit to the equation $C_p/T = \gamma T^2 + \beta_3$ gives β_3 = 0.0043(8) mJ mol^{-1} K^{-4} and γ = 0.148(4) mJ mol^{-1}K^{-2}. from T = 4 K to T = 10 K is plotted (purple line). Inset: Heat capacity from T = 0.05 K to T = 225 K is plotted on a linear temperature scale. There are no sharp features indicative of a superconducting phase transition.

The low temperature heat capacity of $Cu_3(HIB)_2$ shows a divergence, or the onset of a peak, at the lowest temperatures. This peak seems to move to higher

temperatures under the application of a $\mu_0 H = 1$ T field, suggesting ferromagnetic behavior. The heat capacity of $Ni_3(HIB)_2$ shows a hump between $T = 0.02$ K and $T = 2.5$ K. There is a large divergence at the lowest temperatures in this material as well. It is possible that both features could be attributed to either magnetic or nuclear contributions to the heat capacity.

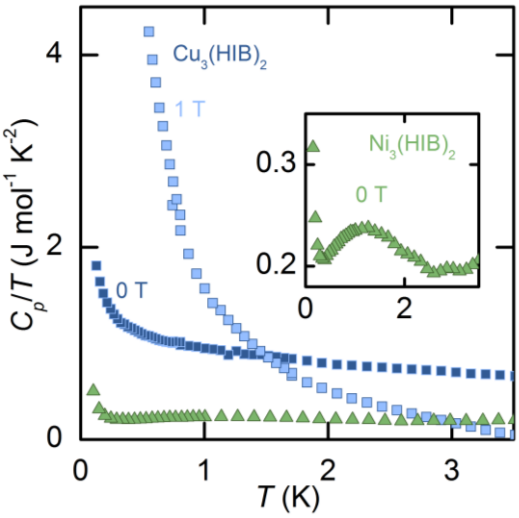

Figure 4.12 Low temperature heat capacity of $Cu_3(HIB)_2$ under fields of $\mu_0 H = 0$ T (dark blue squares) and $\mu_0 H = 1$ T (light blue squares) and $Ni_3(HIB)_2$ under $\mu_0 H = 0$ T. Inset: a zoomed in region in $Ni_3(HIB)_2$.

Despite the reported metallicity in the MOF's $Ni_3(HIB)_2$ and $Cu_3(HIB)_2$, our heat capacity and resistivity data suggest that these materials are actually small band gap semiconductors with some possible magnetic properties at very low temperatures. We do not observe evidence for superconducting transitions down to $T = 0.05$ K.

References

[1] J. S. Helton, K. Matan, M. P. Shores, E. A. Nytko, B. M. Bartlett, Y. Yoshida, Y. Takano, A. Suslov, Y. Qiu, J.-H. Chung, D. G. Nocera, and Y. S. Lee, *Phys. Rev. Lett*. 98, 107204 (2007).

[2] M. P. Shores, E. A. Nytko, B. M. Bartlett, and D. G. Nocera *J. Am. Chem. Soc.*, *127*, 39 (2005).

[3] T-H. Han, J. S. Helton, S. Chu, D. G. Nocera, J. A. Rodriguez-Rivera, C. Broholm and Y. S. Lee *Nature*, 492 (2012).

[4] S. Yan, D. A. Huse, S. R. White, Science, 332, 6034 (2011).

[5] R R. P. Singh and D. A. Huse, Phys. Rev. B 76, 180407(R) (2007).

[6] S. A. Baudron, P. Batail, C. Coulon, R. Clérac, E. Canadell, V. Laukhin, R. Melzi, P. Wzietek, D. Jérome, P. Auban-Senzier, and S. Ravy. *J. Am. Chem. Soc.*, 127, 33 (2005).

[7] J. N. Behera and C. N. R. Rao, *J. Am. Chem. Soc.*, *128*,29 (2006).

[8] E.Miner, T. Fukushima, D. Sheberla, L. Sun, Y. Surendranath, M. Dincă, *Nat. Commun.* 7 (2016).

[9] A. J. Clough, J. W. Yoo, M. H. Mecklenburg; S. C. Marinescu, *J. Am. Chem. Soc.*, 137 (2015)

[10] S. Zhao, Y. Wang, J. Dong, C.-T. He, H. Yin, P. An, K. Zhao, X. Zhang, C. Gao, L. Zhang, J. Lv, J. Wang, J. Zhang, A. M. Khattak, N. A. Khan, Z. Wei, J. Zhang, S. Liu, H. Zhao, Z. Tang, *Nat. Energy*, 1 (2016).

[11] G. Wu, J. Huang, Y. Zang, H. He, G. Xu, *J. Am. Chem. Soc.*, 139 (2017).

[12] L. Sun, M.G. Campbell, M. Dincă, *Angew. Chem., Int. Ed.*, 55 (2016).

[13] J-H. Dou, L. Sun, Y. Ge, W. Li, C. H. Hendon, J. Li, S. Gul, J. Yano, E. A. Stach, and M. Dincă. *J. Am. Chem. Soc.*, *139*, 39 (2017).

Biography

Jennifer Rose Morey was born on October 12, 1990 to Charles Calvin Morey and Betty Lou (Bernhardt) Morey. She was raised in Ashby, MA, where most of her immediate family still lives. She graduated from North Middlesex Regional High School in 2008 where she was actively involved in concert band and theater. She received the International Library of Poetry: Editor's Choice Award in April of 2006 and again in October of 2006. She received the Band Director's Award, the NMRHS Certificate of Academic Excellence in Brass Performance, and the Local Musician's Association Award for outstanding musicianship and accomplishment on the French horn. She received a number of scholarships, including the John and Abigail Adams Scholarship, the NM Band Parent Booster Association Scholarship, and the Sterilite Scholarship.

She attended the University of Rochester from 2008 to 2012, graduating with a B.S. in Chemistry and a minor in Environmental Geology. While there, she was an active member of the Music Interest Floor and many campus ensembles, including the Wind Symphony and the Symphony Orchestra, and took lessons at the Eastman School of Music with Erin Futterer. Her independent research in her junior and senior years was titled "Paleoclimate Reconstruction at the Paleocene-Eocene Thermal Maximum (~55 Ma) using Light Stable Isotopes found in Mollusk Shells" which were collected in the Hanna Basin, WY, under the supervision of her research advisor Dr. Pennilyn Higgins. Her academic advisor was Dr. James Farrar.

Jen attended the University of Wyoming in Laramie, WY from 2012 to 2014, earning a M.S. in Geology with a focus on low-temperature aqueous geochemistry. Her thesis,

supervised by Dr. Carrick. M. Eggleston, was entitled “Photoelectrochemistry at the mineral/water interface and naturally occurring two-layer solar cells”. While at UW, she received the University of Wyoming Brass Scholarship to study horn with Jason Johnston.

She began research with Dr. Tyrel McQueen in Fall of 2014. Her research has been highly collaborative in nature, and she has been able to work with many talented physicists in the Institute for Quantum Matter, including Dr. Collin Broholm and Dr. Kemp Plumb. She attended the National School for X-Ray and Neutron Scattering at Oak Ridge National Laboratory and Argonne National Laboratory and Modern Methods in Rietveld Refinement for Structural Analysis at Oak Ridge National Laboratory in summer 2017.

Jen took every opportunity she had to teach at JHU. She was a teaching assistant for introductory chemistry lecture and laboratory in the 2014-2015 year, the head teaching assistant for introductory chemistry lecture in fall 2015, and a teaching assistant for Dr. McQueen’s class, Chemical Structure and Bonding in spring 2015. In 2016 she completed the Preparing Future Faculty Teaching Academy and attended the Teaching Academy Summer Teaching Institute run by the Center for the Integration of Research, Teaching, and Learning. In fall 2017 she was the instructor for a class she designed called “Surfaces and Interfaces in Engineering”, which was targeting to first-semester freshman in the Whiting School of Engineering. She is currently a Teaching as Research Fellow, and was the recipient of the Dean’s Teaching Fellowship, which she had to decline due to graduation.

Jen, along with another student, Avery Baumann, founded ChemDNA: Diversity Networking and Advancement: a group in the Department of Chemistry to promote

inclusivity and diversity in the department and discipline. She served as a graduate student representative on the Homewood Council on Inclusive Excellence in the 2017-2018 school year, an advisory council to the Deans of the Krieger School of Arts and Sciences, Whiting School of Engineering, and the Sheridan Libraries. While at JHU she received the Owen Fellowship for an Advanced Graduate Student in summer 2017.

Jen studied horn under Denise Tryon at the Peabody Conservatory for her last two years at JHU. She earned her M.A. in Chemistry in 2016 and her Ph.D. in 2018.